ONLINE INERTIAL MEASUREMENT UNIT SENSOR BIAS AND ATTITUDE ESTIMATION FOR THE CALIBRATION AND IMPROVED PERFORMANCE OF ATTITUDE AND HEADING REFERENCE SYSTEMS

by

Andrew R. Spielvogel

A dissertation submitted to Johns Hopkins University
in conformity with the requirements for the degree of
Doctor of Philosophy

Baltimore, Maryland
March, 2020

Abstract

Dynamic instrumentation and estimation of vehicle attitude is critical to the accurate navigation of land, sea, and air vehicles in dynamic motion. The focus of this thesis is the development of algorithms for improved performance of attitude and heading reference systems (AHRSs) and robotic vehicle navigation. inertial measurement unit (IMU) sensor bias estimation methods for use in the calibration of AHRSs and an adaptive attitude estimator operating directly of $SO(3)$ are reported. The reported algorithms provide online calibration and attitude estimation methods which enable more accurate navigation for robotic vehicles.

This thesis differentiates AHRSs into two categories – AHRSs that estimate true-North heading and those that estimate magnetic north heading. Chapters 3-5 report several novel algorithms for micro-electro-mechanical systems (MEMS) IMU sensor bias estimation. Observability, stability, and parameter convergence are evaluated in numerical simulations, full-scale vehicle laboratory experiments, and full-scale field trials in the Chesapeake Bay, MD.

Chapter 6 reports an adaptive sensor bias observer and attitude observer operating directly on $SO(3)$ for true-North gyrocompass systems that utilize six-degrees of freedom (DOF) IMUs with three-axis accelerometers and

three-axis angular rate gyroscopes (without magnetometers) to dynamically estimate the instrument's time-varying true-North attitude (roll, pitch, and geodetic heading) in real-time while the instrument is subject to a priori unknown rotations. Stability proofs for the reported bias and attitude observers, preliminary simulations, and a full-scale vehicle trial are reported.

The presented calibration methods are shown experimentally to improve calibration of AHRS attitude estimation over current state of the art sensor bias estimation methods, and this thesis presents a true-North gyrocompass system based on adaptive observers for use with strap-down IMUs. These results may prove to be useful in the development of navigation systems for small low-cost robotic vehicles.

Thesis Committee

Readers

Louis L. Whitcomb (Advisor)
Professor
Department of Mechanical Engineering
G.W.C. Whiting School of Engineering
Johns Hopkins University

Noah J. Cowan
Professor
Department of Mechanical Engineering
G.W.C. Whiting School of Engineering
Johns Hopkins University

Marin Kobilarov
Assistant Professor
Department of Mechanical Engineering
G.W.C. Whiting School of Engineering
Johns Hopkins University

Acknowledgments

Many people have helped me on my Ph.D. journey.

My adviser, Professor Louis L. Whitcomb, has been an amazing mentor. He has helped me become a better engineer and researcher and always ensured that I had the resources needed to conduct my research. I have benefited greatly from working with him and look forward to future collaborations.

I would also like to thank Professor Noah J. Cowan and Professor Marin Kobilarov for graciously agreeing to serve on my thesis committee.

The research reported in this thesis would not have been possible without the support of the National Science Foundation under NSF awards OCE-1435818 and IIS-1909182. In addition, I would like to thank Johns Hopkins University (JHU) Department of Mechanical Engineering for providing a 9 month Departmental Fellowship to support me for my first academic year as a Ph.D. student.

Thank you to all of my lab-mates from the DSCL – Laughlin, Abhi, Zak, JR, Annie, Cora, Tyler, and Rachel. You have all made working in our lab a great experience!! Thank you to the rest of my LCSR colleagues — especially Matt, Gowtham, Paul, Gabe, Shahriar, Farshid, and Chris.

Thank you to all of my friends outside of the lab for making the last five

and a half years a lot of fun – Arthur, Corinna, Dan, Gianna, Anu, Tracy, Harsh, Matt, Amy, Debjoy, Michelle, Andrew, Mikey, Ben, Steph, Meg, Dom.

Thank you to Jess and her fuzzy sidekick Wiki for being there on this journey. You are my best friend and have kept me sane throughout finishing up this thesis.

To my family – Mom, Dad, Carl, Grandma Gaby, Grandpa Gil, Grandma Sandra, Grandpa Art – Thank you for supporting me for almost 3 decades and for all your understanding and support during my time in graduate school!

Table of Contents

List of Tables

List of Figures

List of Acronyms

AUV autonomous underwater vehicle

AHRS attitude and heading reference system

COTS commercial-off-the-shelf

DOF degrees of freedom

DR dead-reckoned

DVL Doppler velocity log

EKF extended Kalman filter

FOG fiber optic gyroscope

GPS global positioning system

HTF hydrodynamic test facility

IGRF International Geomagnetic Reference Field

IMU inertial measurement unit

INS inertial navigation system

JHU Johns Hopkins University

MAVBE magnetometer and angular velocity bias estimator

MEMS micro-electro-mechanical systems

MLE maximum likelihood estimate

NED North-East-Down

PDS positive definite symmetric

PE persistently exciting

PSO particle swarm optimization

RLG ring laser gyro

RMSE Root mean square error

ROV remotely operated vehicle

UKF unscented Kalman filter

UUV unmanned underwater vehicle

UV underwater vehicle

UCO uniformly completely observable

WMM World Magnetic Model

Chapter 1

Motivation

The dynamic instrumentation and estimation of vehicle attitude, especially geodetic heading, is critical to the accurate navigation of land, sea, and air vehicles in dynamic motion. The need for accurate attitude estimation is particularly acute in the case of vehicles operating in global positioning system (GPS) denied environments (such as underwater). Smaller and lower-cost vehicles represent an additional challenge due to their limited sensor budget, small physical size, and limited energy storage capacity.

Over the past decade, the development of a new generation of small low-cost robotic vehicles has begun to enable oceanographic, environmental assessment, and national security missions that were previously considered impractical or infeasible (e.g. [8, 9, 14, 26, 40, 47, 66, 80]). These small low-cost robotic vehicles commonly employ micro-electro-mechanical systems (MEMS) inertial measurement units (IMUs) comprised of 3-axis MEMS magnetometers, angular rate sensors, and accelerometers to estimate local magnetic heading, pitch, and roll, typically to within several degrees of accuracy, but require careful soft-iron and hard-iron calibration and compensation to achieve these

accuracies. Moreover, magnetic attitude sensors must be recalibrated for soft-iron and hard-iron biases whenever the vehicle's physical configuration changes significantly (i.e. sensors or other payloads added or removed), as very commonly occurs on oceanographic marine and experimental robotic vehicles. Studies have shown that the accuracy of heading sensors is often the principal error source in overall navigation solutions [30]. Thus it is essential to estimate accurately and compensate for attitude sensor biases in order to achieve high accuracy attitude estimation.

This thesis differentiates attitude and heading reference systems (AHRSs) into two different classifications – those that estimate true-North heading and those that estimate magnetic north heading. The focus of this thesis is the estimation of attitude and IMU sensor biases for use in the calibration of these two different classes of AHRSs.

1.1 True-North Versus Magnetic Heading

True-North heading estimation differs from that of magnetic heading in that true-North heading is the direction towards the Earth's axis of rotation at the North Pole, while magnetic heading measures the direction of the horizontal component of the Earth's local magnetic field, which differs dramatically from true-North, often by many 10's of degrees and varies with geodetic location and over time – a difference termed *local magnetic variation*.

Magnetic heading AHRSs utilize magnetometers for measuring the Earth's local magnetic field vector and fuse that measurement with accelerometer measurements to generate a magnetic heading direction in the local level

plane. Magnetometers (including those employed in IMUs) are subject to two primary sensor calibration errors: hard-iron and soft-iron biases. Hard-iron biases are constant magnetometer sensor bias terms due to the permanent magnetic signature of the instrument and the vehicle. Soft-iron biases are non-constant magnetometer sensor bias terms due to the magnetic permeability of the instrument and the vehicle, and will vary with vehicle heading and attitude. For most IMU magnetometers, hard-iron biases dominate soft-iron biases.

The most commonly utilized model for 3-axis magnetometer hard-iron and soft-iron sensor bias is

$$m_m(t) = Tm_t(t) + m_b + \eta_m(t) \tag{1.1}$$

$$\tag{1.2}$$

where $m_m(t) \in \mathbb{R}^3$ is the measured magnetic sensor value in the instrument frame, $m_t(t) \in \mathbb{R}^3$ is the true magnetometer field vector in the instrument frame, $T \in \mathbb{R}^{3\times3}$ is a positive definite symmetric (PDS) matrix due to soft-iron effects, $m_b \in \mathbb{R}^3$ is the sensor bias due to hard-iron effects, and $\eta_m(t)$ is the zero-mean Gaussian measurement noise.

The gyroscope sensors (includes all MEMS IMUs) used in magnetic-North attitude sensors typically lack the sensitivity (the magnitude of Earth rate is orders of magnitude smaller than the magnitude of MEMS angular rate gyro sensor noise) to detect the 15°/hr angular rate of Earth and are commonly

modeled as

$$w_m(t) = \cancelto{0}{w_E(t)} + w_v(t) + w_b + \eta_w(t) \tag{1.3}$$

where $w_m(t) \in \mathbb{R}^3$ is the measured angular rate vector in instrument coordinates, $w_E(t) \in \mathbb{R}^3$ is the angular rate of the Earth (15°/hr), $w_v(t) \in \mathbb{R}^3$ is the angular rate of the instrument with respect to the local North, East, Down frame, $w_b \in \mathbb{R}^3$ is a constant measurement bias, and $\eta_w(t) \in \mathbb{R}^3$ is zero-mean Gaussian measurement noise.

In contrast, true-North gyrocompass systems use high-end gyroscopes, such as three-axes fiber optic gyroscopes (FOGs) or ring laser gyros (RLGs), which are sensitive enough ($\|w_E(t)\| \gtrsim \|\eta_w(t)\|$) to measure Earth's angular rate and are typically modeled as

$$w_m(t) = w_E(t) + w_v(t) + w_b + \eta(t) \tag{1.4}$$

where the terms are the same as in (1.3). Table 6.1, on page 127, compares the technical specifications of these different classes of IMUs. By fusing gyroscope and accelerometer measurements, true-North gyrocompass systems generate an estimate for the true-North heading direction and roll and pitch (local level).

In both classes of AHRSs, sensor biases vitiate the accuracy of attitude estimation of the systems. Hence, accurate estimation of sensor biases is essential for AHRSs. In magnetic heading systems, soft-iron and hard-iron magnetometer biases, T and m_b, are the most important biases to estimate and compensate for, and in true-North heading systems, accurate w_b estimation

and compensation is essential. In addition fo estimation and compensation of sensor biases, this thesis focuses on methods for performing on-line estimation and compensation of IMU sensor biases for use in both magnetic-North and true-North AHRSs.

1.2 Thesis Outline

The main contributions of this Thesis are presented in Chapters 3-6. Chapters 3-5 focus on novel on-line methods for the calibration of magnetic heading AHRSs, while Chapter 6 presents nonlinear adaptive observers for a true-North gyrocompass AHRS.

Chapter 2 - Preliminaries: Chapter 2 defines the coordinate frames, notation, and mathematic preliminaries used in this thesis.

Chapter 3 - Sensor Bias Identification in 9-DOF MEMS IMUs [61]: Nine degrees of freedom (DOF) inertial measurement units (IMUs) comprised of three-axis magnetometers, three-axis accelerometers, and three-axis angular rate sensors are commonly used in AHRSs. These systems fuse IMU measurements to generate estimates of the instrument's roll, pitch, and magnetic heading. However, their accuracy is limited by sensor measurement bias that is unknown *a priori*. Hence, accurate sensor bias estimation and compensation is essential for true attitude estimation. This chapter reports a novel adaptive sensor bias observer for sensor measurement biases in 9-DOF IMUs. The algorithm requires (i) smaller angular movements of the instrument than other reported sensor bias calibration methods, (ii) does not require *a priori* knowledge of local fields like the local magnetic field or the local gravity

vector, and (iii) does not require knowledge of the attitude of the instrument. Stability proofs, preliminary simulations, and a full-scale vehicle experimental evaluation are reported. These results were reporting in [61].

Chapter 4 - A Stable Adaptive Observer for Hard-Iron and Soft-Iron Bias Calibration and Compensation for Two-Axis Magnetometers [62]: This chapter addresses the problem of on-line estimation and compensation of the hard-iron and soft-iron biases of a 2-axis magnetometer under dynamic motion, utilizing only biased measurements from a 2-axis magnetometer.

The proposed adaptive observer formulates the relation between the true magnetic field vector and the magnetometer measurements as an algebraic system where the unknown biases enter linearly. The observer is shown to be globally stable. When the magnetometer measurements are persistently exciting (PE), the system is shown to be globally asymptotically stable, and the biases are shown to converge to their true values. The estimated biases are used to provide a calibrated magnetic field direction vector which is utilized to estimate magnetic geodetic heading.

The adaptive observer is evaluated in a numerical simulation and a full-scale vehicle trial. For the proposed observer: (i) knowledge of the instrument attitude is not required for sensor bias estimation, (ii) zero *a priori* knowledge of the local magnetic field vector magnitude or vector direction is needed for accurate AHRS calibration, (iii) the system is shown to be globally stable, (iv) the error system is shown to be globally asymptotically stable when the measured magnetometer signal is PE. (v) magnetometer hard-iron and soft-iron bias compensation is shown to dramatically improve dynamic heading

estimation accuracy. These results were reporting in 4.

Chapter 5 - Online 3-Axis Magnetometer Hard-Iron and Soft-Iron Bias and Angular Velocity Sensor Bias Estimation Using Angular Velocity Sensors for Improved Dynamic Heading Accuracy [63]: This chapter addresses the problem of dynamic on-line estimation and compensation of hard-iron and soft-iron biases of 3-axis magnetometers under dynamic motion in field robotics, utilizing only biased measurements from a 3-axis magnetometer and a 3-axis angular rate sensor. These results were developed in collaboration with Abhimanyu Shah and are reported in [63].

The proposed magnetometer and angular velocity bias estimator (MAVBE) utilizes a 15-state process model encoding the nonlinear process dynamics for the magnetometer signal subject to angular velocity excursions, while simultaneously estimating 9 magnetometer bias parameters (for both hard-iron and soft-iron bias) and 3 angular rate sensor bias parameters, within an extended Kalman filter (EKF) framework. Bias parameter observability is evaluated. The bias-compensated signals, together with 3-axis accelerometer signals, are utilized to estimate bias compensated magnetic geodetic heading.

Performance of the proposed MAVBE method is evaluated in comparison to the widely cited magnetometer-only TWOSTEP [2] method in numerical simulations, laboratory experiments, and full-scale field trials of an instrumented AUV in the Chesapeake Bay, MD, USA. For the proposed MAVBE, (i) instrument attitude is not required to estimate biases, and the results show that (ii) the biases are observable, (iii) the bias estimates converge rapidly to true bias parameters, (iv) only modest instrument excitation is required

for bias estimate convergence, and (v) compensation for magnetometer hard-iron and soft-iron bias dramatically improves dynamic heading estimation accuracy.

Chapter 6 - Adaptive Bias and Attitude Observer on the Special Orthogonal Group for True-North Gyrocompass Systems [58, 59, 60, 64, 65]: This chapter reports an adaptive sensor bias observer and attitude observer operating directly on $SO(3)$ for true-North gyrocompass systems that utilize six-DOF inertial measurement units IMUs with three-axis accelerometers and three-axis angular rate gyroscopes (without magnetometers). Most present-day low-cost robotic vehicles employ attitude estimation systems that employ micro-electromechanical systems MEMS magnetometers, angular rate gyros, and accelerometers to estimate magnetic attitude (roll, pitch, and magnetic heading) with limited heading accuracy. Present day MEMS gyros are not sensitive enough to dynamically detect the Earth's rotation, and thus cannot be used to estimate true-North geodetic heading. Relying on magnetic compasses can be problematic for vehicles which operate in environments with magnetic anomalies and those requiring high accuracy navigation as the limited accuracy ($> 1^{\circ}$ error) of magnetic compasses is typically the largest error source in underwater vehicle navigation systems. Moreover, magnetic compasses need to undergo time-consuming recalibration for hard-iron and soft-iron errors every time a vehicle is reconfigured with a new instrument or other payload, as very frequently occurs on oceanographic marine vehicles. In contrast, the gyrocompass system reported herein utilizes FOG IMU angular rate gyro and MEMS accelerometer measurements (without magnetometers)

to dynamically estimate the instrument's time-varying true-North attitude (roll, pitch, and geodetic heading) in real-time while the instrument is subject to a priori unknown rotations. This gyrocompass system is (i) immune to magnetic anomalies and (ii) does not require recalibration every time a new payload is added to or removed from the vehicle. Stability proofs for the reported bias and attitude observers, preliminary simulations, and a full-scale vehicle trial are reported that suggest the viability of the true-North gyrocompass system to provide dynamic real-time true-North heading, pitch, and roll utilizing a comparatively low-cost FOG IMU. Several different earlier approaches to these problems are reported in [58, 59, 60, 64], and the final version and results are reported in [65].

Chapter 7 - Conclusion: The thesis results are summarized and directions for future work are presented.

Appendix A - Johns Hopkins University (JHU) hydrodynamic test facility (HTF): This appendix reports the Johns Hopkins University (JHU) hydrodynamic test facility (HTF) [29] and its JHU remotely operated vehicle (ROV) and JHU Iver3 autonomous underwater vehicle (AUV) used for the design, development, and testing of oceanographic systems.

Intended to be blank.

Chapter 2

Preliminaries

This chapter summarizes the coordinate frames, notation, and math preliminaries used in this thesis. Section 2.1 defines the coordinate frames used throughout this thesis, Section 2.2 presents the rotation matrix and vector notation used, and Section 2.3 reports mathematical operators, propositions, and lemmas used throughout this thesis.

2.1 Coordinate Frames

We define the following coordinate frames:

- **Instrument Frame:** A frame, denoted (i), fixed in the IMU instrument.
- **North-East-Down (NED) Frame:** The NED frame, denoted (N), has its x-axis pointing North, its y-axis pointing East, its z-axis pointing down, and its origin co-located with that of the instrument frame.

Figure 2.1 illustrates these two coordinate frames.

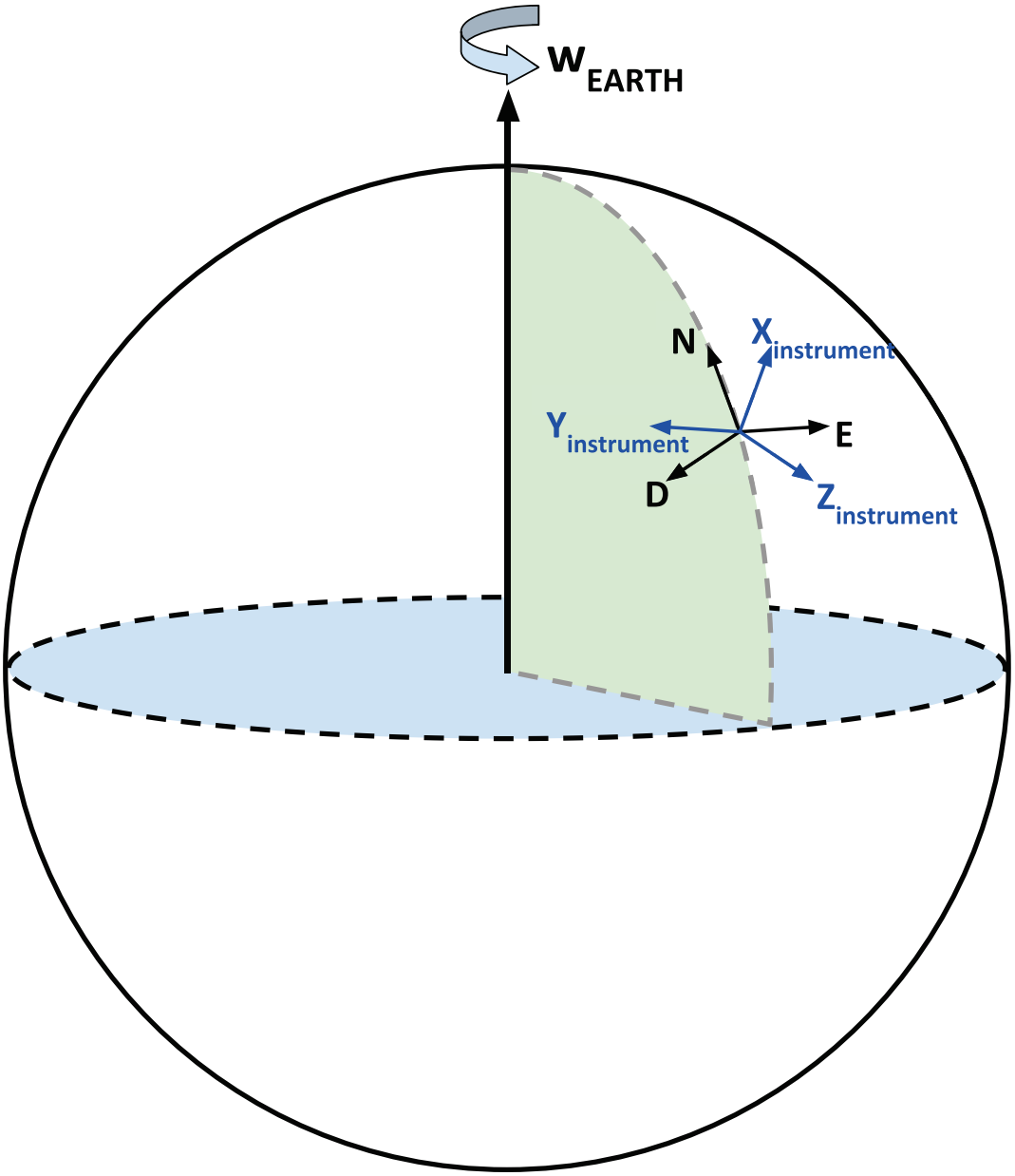

Figure 2.1: The North-East-Down (NED) and instrument coordinate frames are co-located.

2.2 Notation

For vectors, a leading superscript indicates the frame of reference and a following subscript indicates the signal source, thus ${}^{N}w_m$ is the measured instrument angular velocity in the NED frame and ${}^{i}a_m$ is the measured instrument linear acceleration in the instrument sensor frame.

For rotation matricies a leading superscript and subscript indicates the frames of reference. For example, ${}^{N}_{i}R$ is the rotation from the instrument frame to the NED frame.

2.3 Mathematical Preliminaries

This section presents operators and mathematical facts that will be used throughout this thesis.

2.3.1 Operators

The following operators will be used throughout this thesis.

Skew-Symmetric Operator: $\mathcal{J}$ is a mapping $\mathbb{R}^3 \rightarrow so(3)$, such that $\forall\ x \in \mathbb{R}^3$,

$$\mathcal{J}(x) = \begin{bmatrix} 0 & -x_3 & x_2 \\ x_3 & 0 & -x_1 \\ -x_2 & x_1 & 0 \end{bmatrix}, \tag{2.1}$$

where $x = [x_1\ x_2\ x_3]^T$. We define its inverse $\mathcal{J}^{-1} : so(3) \rightarrow \mathbb{R}^3$, such that $\forall x \in \mathbb{R}^3, \mathcal{J}^{-1}(\mathcal{J}(x)) = x$.

Jacobian Operator: $\mathbf{D}$ is a mapping $\mathbb{R}^m \rightarrow \mathbb{R}^{m\times n}$, such that for $x \in \mathbb{R}^n$ and $f : \mathbb{R}^n \rightarrow \mathbb{R}^m$, $\mathbf{D}_x[f(x)]_\mu$ gives the $m \times n$ Jacobian of $f(x)$ with respect to

x evaluated at μ.

Stack Operator: $(\cdot)^s$ is a mapping $\mathbb{R}^{m\times n} \to \mathbb{R}^{mn}$. For a matrix $A \in \mathbb{R}^{m\times n}$, the stack operator [55] is defined as

$$A^s = [a_{11} \ \dots \ a_{m1} \ a_{12} \ \dots \ a_{m2} \ a_{1n} \ \dots \ a_{mn}]^T. \tag{2.2}$$

Kronecker Product For a matrix $A \in \mathbb{R}^{p\times q}$ and $B \in \mathbb{R}^{r\times s}$, the Kronecker product [55] is defined as

$$A \otimes B = \begin{bmatrix} a_{11}B & \dots & a_{1q}B \\ \vdots & & \vdots \\ a_{p1}B & \dots & a_{pq}B \end{bmatrix}. \tag{2.3}$$

2.3.2 Mathematical Background

We will make use of the following mathematical facts:

Proposition: For $Q(t) \in so(3)$, the rotation matrix $R(t)$ can be computed by Rodrigues Equation [41]

$$R(t) = I_{3\times 3} + \gamma(t)Q(t) + \kappa(t)Q(t)^2 \tag{2.4}$$

where

$$\gamma(t) = \frac{\sin(\|q(t)\|)}{\|q(t)\|} \tag{2.5}$$

$$\kappa(t) = \frac{1-\cos(\|q(t)\|)}{\|q(t)\|^2} \tag{2.6}$$

$$q(t) = \mathcal{J}^{-1}(Q(t)). \tag{2.7}$$

Proposition: $\dot{q}(t)$ is related to $\dot{R}(t)$ by the mapping

$$R^T(t)\dot{R}(t) = \mathcal{J}(A(q(t))\dot{q}(t)) \tag{2.8}$$

where $A(q(t))$ is the right Jacobian of $R(t) = e^{\mathcal{J}(q(t))}$ with respect to the angular position vector $q(t) \in \mathbb{R}^3$. $A(q(t))$:

$$A\left(q(t)\right) = I_{3\times 3} - \phi(t)\mathcal{J}\left(q(t)\right) + \psi(t)\mathcal{J}^2\left(q(t)\right) \tag{2.9}$$

$$\phi(t) = \frac{1-\cos\left(\|q(t)\|\right)}{\|q(t)\|^2} \tag{2.10}$$

$$\psi(t) = \frac{\|q(t)\| - \sin\left(\|q(t)\|\right)}{\|q(t)\|^3} \tag{2.11}$$

and its inverse,

$$A^{-1}(q(t)) = I_{3\times 3} + \alpha\mathcal{J}(q(t)) + \beta(t)\mathcal{J}^2(q(t)) \tag{2.12}$$

where

$$\alpha = \frac{1}{2}, \tag{2.13}$$

$$\beta(t) = \frac{1}{\|q(t)\|^2} - \frac{1+\cos(\|q(t)\|)}{2\|q(t)\|\sin(\|q(t)\|)}, \tag{2.14}$$

are reported in [7].

If $A(q(t))$ is invertible, (2.8) can be rearranged as

$$\dot{q}(t) = A^{-1}\left(q(t)\right)\mathcal{J}^{-1}\left(R^T(t)\dot{R}(t)\right). \tag{2.15}$$

Definition (Persistent Excitation (PE)) [52]: A matrix function $\mathcal{W} : \mathbb{R}^+ \rightarrow$

$\mathbb{R}^{m\times m}$ is PE if there exists $T, \alpha_1, \alpha_2 > 0$ such that for all $t \geq 0$:

$$\alpha_1 I_m \geq \int_t^{t+T} \mathcal{W}(\tau)\mathcal{W}^T(\tau)\, d\tau \geq \alpha_2 I_m \tag{2.16}$$

where $I_m \in \mathbb{R}^{m\times m}$ is the identity matrix.

Definition: Uniform Complete Observability (UCO) [52] The system $[A(t), C(t)]$ is called uniformly completely observable (UCO) if there exist strictly positive constants β_1, β_2, δ, such that, $\forall t_0 \geq 0$

$$\beta_2 I \geq N(t_0, \delta) \geq \beta_1 I \tag{2.17}$$

where $N(t_0, \delta) \in \mathbb{R}^{n\times n}$ is the observability grammian

$$N(t_0, \delta) = \int_{t_0}^{t_0+\delta} \Phi^T(\tau, t_0)C^T(\tau)C(\tau)\Phi(\tau, t_0)\, d\tau \tag{2.18}$$

and $\Phi(t, t_0)$ is the transition matrix for $A(t)$ [51].

Lemma 1 : The following lemma is a variation of Lemma A.1 in [5]. Given a system of the following form:

$$\dot{x}(t) = A(t)x(t) + f(t) \tag{2.19}$$

$$y(t) = Cx(t) \tag{2.20}$$

where $x(t) \in \mathbb{R}^n$, and $y(t) \in \mathbb{R}^p$ such that

(i) $\lim_{t\to\infty} \|y(t)\| = 0$

(ii) $\lim_{t\to\infty} \|f(t)\| = 0$

(iii) $[A(t), C]$ is UCO;

then $\lim_{t\to\infty} \|x(t)\| = 0$.

Lemma 1 Proof: The proof follows the structure of the proof of Lemma A.1 in [5].

First, note that from (iii), the system

$$\dot{x}(t) = A(t)x(t) \tag{2.21}$$

$$y(t) = Cx(t) \tag{2.22}$$

is UCO. That is, $\exists \beta_1, \beta_2, \delta > 0$ such that $\forall t_0 \geq 0$, the observability grammian

$$N(t_0, \delta) = \int_{t_0}^{t_0+\delta} \Phi^T(\tau, t_0) C^T C \Phi(\tau, t_0)\, d\tau \tag{2.23}$$

satisfies (2.17).

Next, recall that the solution of the system (2.19) for any $t_0 \geq 0$ is given by

$$x(t) = \Phi(t, t_0)x(t_0) + \int_{t_0}^{t} \Phi(t, \tau) f(\tau)\, d\tau. \tag{2.24}$$

Then

$$
\begin{aligned}
N(t,\delta)x(t) &= \int_t^{t+\delta} \Phi^T(\tau,t)C^TC\Phi(\tau,t)\,d\tau\ x(t) \\
&= \int_t^{t+\delta} \Phi^T(\tau,t)C^TC\Phi(\tau,t)[\Phi(t,t_0)x(t_0) \\
&\quad + \int_{t_0}^{t} \Phi(t,s)f(s)\,ds]\,d\tau \\
&= \int_t^{t+\delta} \Phi^T(\tau,t)C^TC[x(\tau) \\
&\quad - \int_t^{\tau} \Phi(\tau,s)f(s)\,ds]\,d\tau \\
&= \int_0^{\delta} \Phi^T(\sigma+t,t)C^T[Cx(\sigma+t) \\
&\quad - \int_t^{\sigma+t} C\Phi(\sigma+t,s)f(s)\,ds]\,d\sigma \\
&= \int_0^{\delta} \Phi^T(\sigma+t,t)C^T[y(\sigma+t) \\
&\quad - \int_0^{\sigma} C\Phi(\sigma+t,v+t)f(v+t)\,dv]\,d\sigma
\end{aligned}
\tag{2.25}
$$

Since

- $\Phi(\sigma+t,t)$ and $\Phi(\sigma+t,v+t)$ are bounded (from (iii)) on $[0,\delta]$,
- $\lim_{t\to\infty} y(t) = 0$,
- and $\lim_{t\to\infty} f(t) = 0$,

then

$$\lim_{t\to\infty} N(t, t+\delta)x(t) = 0. \tag{2.26}$$

Thus, from (2.26) and (iii), we can conclude that

$$\lim_{t\to\infty} \|x(t)\| = 0. \tag{2.27}$$

Barbalat's Lemma [27]: Let $\phi : \mathbb{R} \to \mathbb{R}$ be a uniformly continuous function on $[0, \infty)$. Suppose that $\lim_{t\to\infty} \int_0^t \phi(\tau)\, d\tau$ exists and is finite. Then,

$$\lim_{t\to\infty} \phi(t) = 0. \tag{2.28}$$

Intended to be blank.

Chapter 3

Sensor Bias Identification in 9-DOF MEMS IMUs

3.1 Introduction

This chapter is based on the results and research reported in [61]. The chapter reports, to the authors' knowledge, the first method for doing real-time sensor bias estimation of 9-DOF IMUs without the need for knowledge of the instrument's attitude. In addition, the proposed algorithm requires smaller angular movements compared to common sensor bias estimation methods, does not require local field information, and can be implemented in real-time.

Nine DOF IMUs comprised of three-axis magnetometers, three-axis accelerometers, and three-axis angular-rate sensors are widely used in AHRSs for robotic vehicle navigation and in personal electronics such as smart-phones and tablets. AHRSs are comprised of two classes: AHRSs that estimate true-North heading and those that estimate magnetic-North heading. True-North heading AHRSs require angular rate sensors sensitive enough to dynamically estimate Earth-rate (typically fiber-optic or ring-laser gyros). Magnetic-North

heading AHRSs instead use magnetometers for estimating heading, as their angular rate sensors commonly are not sensitive enough to detect Earth-rate dynamically (i.e. all MEMS gyros). This chapter will focus on the ubiquitous latter class of AHRSs that employ angular rate sensors which lack the sensitivity to detect the Earth-rate signal. Magnetometers measure Earth's local magnetic field vector and are commonly used to determine the device heading. Accelerometers measure the linear acceleration and are commonly used as a low frequency measurement of Earth's local gravity vector (roll and pitch). Angular-rate gyroscopes measure the angular velocity of the device.

Several methods for doing magnetic heading attitude estimation with 9-DOF IMUs have been reported. Crassidis et al. provide a review of attitude estimation methods [12]. Nonlinear complementary filters for doing attitude estimation are reported by Hamel and Mahony [20], Mahony et al. [35], and Metni et al. [37, 38]. Wu et al. report a globally asymptoticly stable attitude observer on $SO(3)$ and a recent study by Costanzi et al. explores utilizing a FOG for doing attitude estimation under unknown magnetic disturbances [10].

These attitude observers, however, require accurate sensor bias estimation and calibration in order to achieve accuracy to within several degrees of accuracy. Moreover, magnetic attitude sensors must be recalibrated for soft-iron and hard-iron errors whenever the vehicle physical configuration changes significantly (i.e. sensors or other payloads added or removed, etc.). Studies have shown that the accuracy of these magnetic heading sensors can be a principal error source in overall navigation solutions [30]. Thus, it is essential

to accurately estimate sensor biases in order to achieve high accuracy attitude estimation.

Several methods for magnetometer bias estimation have been reported in recent years. Alonso and Shuster proposed the widely cited "TWOSTEP" method [1] for estimating magnetometer hard-iron sensor bias, and in another paper an extended method for calculating magnetometer scale and orthogonality factors as well [2]. Vasconselos et al. present magnetometer bias estimation as an ellipsoid fitting problem which can be solved with an iterative maximum likelihood estimate (MLE) approach [74]. Kok et al. [31] and Li and Li [33] fuse accelerometer measurements with magnetometer measurements to estimate magnetometer sensor bias. These methods, however, require large angular movements and are batch estimators that are not practical for on-line real-time estimation of magnetometer sensor bias.

Sensor biases change over time due to changes in sensor payload, temperature, etc., which make it imperative to estimate sensor biases in real time. Crassidis et al. report an extension to the TWOSTEP method based on the EKF [11] and Guo et al. present an alternative EKF approach for doing magnetometer sensor bias estimation [19]. Troni and Whitcomb [70, 72] report an adaptive method utilizing gyroscope measurements for doing magnetometer sensor measurement hard-iron bias estimation. However, while these approaches estimate magnetometer biases in real time they do not address real-time estimation of accelerometer and angular-rate gyroscope sensor bias which is needed for accurate dynamic attitude estimation.

George and Sukkarieh report an identifier for accelerometer and gyroscope

sensor bias [18]. However, they utilize GPS which is unavailable to robotic vehicles in GPS-denied environments (i.e. land and air vehicles without clear view of the sky, and all submerged underwater vehicles). Scandaroli et al. [54] and Scandaroli and Morin [53] also report a sensor bias estimator for 6-DOF IMUs (3-axis accelerometer and 3-axis gyroscope) utilizing computer vision. This method though is dependent on the presence of a vision system, which requires identification markers and a camera system which is unavailable for many robotic vehicle (e.g. many underwater vehicles (UVs)). In addition, Metni et al. and Pflimlin et al. report nonlinear complementary filters for estimating attitude and gyroscope sensor bias [37, 38, 50]. While these estimators identify angular-rate sensor bias or both angular-rate and linear acceleration sensor bias, they do not estimate sensor biases of full 9-DOF IMUs that are commonly used in attitude estimation systems.

This chapter is organized as follows: Section 3.2 reports the IMU measurement model. Section 3.3 reports the 9-DOF IMU sensor bias observer and stability proof. Section 3.4 presents numerical simulations. Section 3.5 presents experimental results. Section 3.6 summarizes and concludes.

3.2 9-DOF IMU Measurement Model

We define the following measurement models for 9-DOF IMUs:

$$^{i}a_{e}(t) = {}^{i}a_{g}(t) + {}^{i}a_{v}(t) + {}^{i}a_{b} \tag{3.1}$$

$$^{i}w_{e}(t) = {}^{i}w_{E}(t) + {}^{i}w_{v}(t) + {}^{i}w_{b} \tag{3.2}$$

$$^{i}m_{e}(t) = T{}^{i}m_{t}(t) + {}^{i}m_{b} \tag{3.3}$$

where $^{i}w_{e}(t)$ is the noise-free angular-rate measurement, $^{i}w_{E}(t)$ is the true angular velocity due to the rotation of the Earth, $^{i}w_{v}(t)$ is the true angular velocity due to the rotation of the instrument with respect to the NED frame, $^{i}w_{b}$ is the angular velocity sensor bias offset, $^{i}a_{e}(t)$ is the noise-free linear acceleration measurement, $^{i}a_{g}(t)$ is the true linear acceleration due to gravity and the Earth's rotation, $^{i}a_{v}(t)$ is the instrument's true linear acceleration with respect to Earth, $^{i}a_{b}$ is the linear accelerometer sensor bias offset, $^{i}m_{e}(t)$ is the noise-free magnetometer measurement, $^{i}m_{t}(t)$ is Earth's true magnetic field, T is the orthogonality matrix, and $^{i}m_{b}$ is the magnetometer sensor bias offset. T is a heading dependent magnetometer error that is commonly called soft-iron error, while the constant magnetometer bias, $^{i}m_{b}$, is called hard-iron error and is often the dominant magnetometer error source.

For many robotic vehicles, the gravitational field $^{i}a_{g}(t)$ dominates the vehicle linear acceleration ($^{i}a_{v}(t)$). Thus, it is common to employ the approximation

$$^{i}a_{e}(t) \approx {}^{i}a_{g}(t) + {}^{i}a_{b} \tag{3.4}$$

as a low-frequency estimate of (3.1) [10, 35, 50, 78]. The measurement noise in MEMS IMU angular rate sensors is many orders of magnitude larger than the Earth-rate signal ${}^{i}w_E(t)$. Hence, it is common to neglect the (undetectable) Earth-rate signal in MEMS IMU gyro measurement models. A previous study by Troni and Whitcomb [72] has shown that the orthogonality matrix, T, in the MicroStrain 3DM-GX3-25 MEMS IMU is close to the identity matrix. Therefore, T is approximated to be the identity matrix and the resulting sensor measurement model is

$$ {}^{i}a_e(t) = {}^{i}a_g(t) + {}^{i}a_b \tag{3.5} $$

$$ {}^{i}w_e(t) = {}^{i}w_v(t) + {}^{i}w_b \tag{3.6} $$

$$ {}^{i}m_e(t) = {}^{i}m_t(t) + {}^{i}m_b. \tag{3.7} $$

Hard-iron errors dominate soft-iron errors, and hence hard-iron bias estimation is the magnetometer sensor bias focused on in this chapter. We address soft-iron errors in Chapters 4 - 5.

3.3 9-DOF IMU Sensor Bias Observer

3.3.1 System Model

We consider the system model

$$ {}^{N}a_g = {}^{N}_{i}R(t)\left({}^{i}a_e(t) - {}^{i}a_b\right) \tag{3.8} $$

$$ {}^{N}m_t = {}^{N}_{i}R(t)\left({}^{i}m_e(t) - {}^{i}m_b\right) \tag{3.9} $$

where ${}^{N}_{i}R(t)$ is the rotation from the instrument frame, denoted i, to the NED frame, denoted N. Differentiating (3.8) and (3.9) and rearranging terms yields

$$ {}^{i}\dot{a}_e(t) = -\mathcal{J}\left({}^{i}w_e(t) - {}^{i}w_b\right)\left({}^{i}a_e(t) - {}^{i}a_b\right) \tag{3.10} $$

$$ \approx -\mathcal{J}\left({}^{i}w_e(t)\right)\left({}^{i}a_e(t) - {}^{i}a_b\right) + \mathcal{J}\left({}^{i}w_b\right){}^{i}a_e(t) \tag{3.11} $$

$$ {}^{i}\dot{m}_e(t) = -\mathcal{J}\left({}^{i}w_e(t) - {}^{i}w_b\right)\left({}^{i}m_e(t) - {}^{i}m_b\right) \tag{3.12} $$

$$ \approx -\mathcal{J}\left({}^{i}w_e(t) - {}^{i}w_b\right){}^{i}m_e(t) + \mathcal{J}\left({}^{i}w_e(t)\right){}^{i}m_b \tag{3.13} $$

where we employ the approximation that $\mathcal{J}\left({}^{i}w_b\right){}^{i}a_b \approx 0$ and $\mathcal{J}\left({}^{i}w_b\right){}^{i}m_b(t) \approx 0$, since the cross products between sensor biases are orders of magnitude smaller than the other signals.

3.3.2 9-DOF IMU Sensor Bias Observer

We consider the observer system model

$$ {}^{i}\dot{\hat{a}}_e(t) = -\mathcal{J}\left({}^{i}w_e(t)\right)\left({}^{i}\hat{a}_e(t) - {}^{i}\hat{a}_b(t)\right) + \mathcal{J}\left({}^{i}\hat{w}_b(t)\right){}^{i}\hat{a}_e(t) - k_a\Delta a(t) \tag{3.14} $$

$$ {}^{i}\dot{\hat{m}}_e(t) = -\mathcal{J}\left({}^{i}w_e(t) - {}^{i}\hat{w}_b(t)\right){}^{i}\hat{m}_e(t) + \mathcal{J}\left({}^{i}w_e(t)\right){}^{i}\hat{m}_b(t) - k_m\Delta m(t) \tag{3.15} $$

$$ {}^{i}\dot{\hat{w}}_b(t) = -K_{b_w}\mathcal{J}\left({}^{i}a_e(t)\right)\Delta a(t) - K_{b_w}\mathcal{J}\left({}^{i}m_e(t)\right)\Delta m(t) \tag{3.16} $$

$$ {}^{i}\dot{\hat{a}}_b(t) = K_{b_a}\mathcal{J}\left({}^{i}w_e(t)\right)\Delta a(t) \tag{3.17} $$

$$ {}^{i}\dot{\hat{m}}_b(t) = K_{b_m}\mathcal{J}\left({}^{i}w_e(t)\right)\Delta m(t) \tag{3.18} $$

where k_a and k_m are positive scalar gain constants, K_{b_w}, K_{b_a}, and K_{b_m} are constant positive definite diagonal gain matrices, and we define the error terms as

$$\Delta a(t) = {}^i\hat{a}_e(t) - {}^i a_e(t) \tag{3.19}$$

$$\Delta m(t) = {}^i\hat{m}_e(t) - {}^i m_e(t) \tag{3.20}$$

$$\Delta w_b(t) = {}^i\hat{w}_b(t) - {}^i w_b \tag{3.21}$$

$$\Delta a_b(t) = {}^i\hat{a}_b(t) - {}^i a_b \tag{3.22}$$

$$\Delta m_b(t) = {}^i\hat{m}_b(t) - {}^i m_b. \tag{3.23}$$

Note that in order to show that $\Delta a(t)$ and $\Delta m(t)$ are asymptotically stable, the gains k_a and k_m are chosen to be scalar gains instead of matrix gains.

3.3.3 Error System

The resulting error system is

$$\Delta\dot{a}(t) = -\mathcal{J}\left({}^{i}a_e(t)\right)\Delta w_b(t) + \mathcal{J}\left({}^{i}w_e(t)\right)\Delta a_b(t)$$
$$- k_a\Delta a(t) - \mathcal{J}\left({}^{i}w_e(t) - {}^{i}\hat{w}_b(t)\right)\Delta a(t) \tag{3.24}$$

$$\Delta\dot{m}(t) = -\mathcal{J}\left({}^{i}m_e(t)\right)\Delta w_b(t) + \mathcal{J}\left({}^{i}w_e(t)\right)\Delta m_b(t)$$
$$- \mathcal{J}\left({}^{i}w_e(t) - {}^{i}\hat{w}_b(t)\right)\Delta m(t) - k_m\Delta m(t) \tag{3.25}$$

$$\Delta\dot{w}_b(t) = -K_{b_w}\mathcal{J}\left({}^{i}a_e(t)\right)\Delta a(t) - K_{b_w}\mathcal{J}\left({}^{i}m_e(t)\right)\Delta m(t) \tag{3.26}$$

$$\Delta\dot{a}_b(t) = K_{b_a}\mathcal{J}\left({}^{i}w_e(t)\right)\Delta a(t) \tag{3.27}$$

$$\Delta\dot{m}_b(t) = K_{b_m}\mathcal{J}\left({}^{i}w_e(t)\right)\Delta m(t). \tag{3.28}$$

3.3.4 Stability

Consider the Lyapunov function candidate

$$V = \frac{1}{2}\Delta a^T(t)\Delta a(t) + \frac{1}{2}\Delta m^T(t)\Delta m(t) + \frac{1}{2}\Delta w_b^T(t)K_{b_w}^{-1}\Delta w_b(t)$$
$$+ \frac{1}{2}\Delta a_b^T(t)K_{b_a}^{-1}\Delta a_b(t) + \frac{1}{2}\Delta m_b^T(t)K_{b_m}^{-1}\Delta m_b(t) \tag{3.29}$$

where V is a smooth, positive definite, and radially unbounded function by construction. Differentiating (3.29) yields

$$\begin{aligned}
\dot{V} = &\left(-\Delta a^T(t)\mathcal{J}\left({}^i a_e(t)\right) + \Delta a^T(t)\mathcal{J}\left({}^i a_e(t)\right)\right)\Delta w_b(t) \\
&+ \left(-\Delta m^T(t)\mathcal{J}\left({}^i m_e(t)\right) + \Delta m^T(t)\mathcal{J}\left({}^i m_e(t)\right)\right)\Delta w_b(t) \\
&+ \left(\Delta a^T(t)\mathcal{J}\left({}^i w_e(t)\right) - \Delta a^T(t)\mathcal{J}\left({}^i w_e(t)\right)\right)\Delta a_b(t) \\
&+ \left(\Delta m^T(t)\mathcal{J}\left({}^i w_e(t)\right) - \Delta m^T(t)\mathcal{J}\left({}^i w_e(t)\right)\right)\Delta m_b(t) \\
&- \Delta a^T(t)\mathcal{J}\left({}^i w_e(t) - {}^i\hat{w}_b(t)\right)\Delta a(t) - \Delta m^T(t)\mathcal{J}\left({}^i w_e(t) - {}^i\hat{w}_b(t)\right)\Delta m(t) \\
&- k_a\|\Delta a(t)\|^2 - k_m\|\Delta m(t)\|^2 \\
= &-k_a\|\Delta a(t)\|^2 - k_m\|\Delta m(t)\|^2 \qquad (3.30) \\
\leq &\, 0. \qquad (3.31)
\end{aligned}$$

The time derivative of the Lyapunov candidate function is negative semi-definite, thus guaranteeing global stability of the system, but additional arguments are needed to show global asymptotic stability.

Since the Lyapunov function (3.29) is radially unbounded, bounded below by 0, and bounded above by its initial value, $V(t_0)$, due to (3.30), we can conclude that $\Delta a(t)$, $\Delta m(t)$, $\Delta w_b(t)$, $\Delta a_b(t)$, and $\Delta m_b(t)$ are bounded. If we make the assumption that the signals ${}^i a_e(t)$, ${}^i w_e(t)$, ${}^i m_e(t)$, and ${}^i w_b$ are bounded, then (3.24)-(3.28) are bounded, and hence (3.19)-(3.23) are uniformly

continuous. For all $t \geq 0$,

$$\left(\int_0^t \|\Delta a(\tau)\|^2 \, d\tau \right)^{1/2} \leq \left(\frac{1}{k_a} V(t = t_0) \right)^{1/2}, \tag{3.32}$$

$$\left(\int_0^t \|\Delta m(\tau)\|^2 \, d\tau \right)^{1/2} \leq \left(\frac{1}{k_m} V(t = t_0) \right)^{1/2}. \tag{3.33}$$

Hence, $\Delta a(t), \Delta m(t) \in L^2$. Therefore, from Barbalat's lemma [27], $\Delta a(t)$ and $\Delta m(t)$ are globally asymptotically stable at the origin. Hence,

$$\lim_{t \to \infty} \Delta a(t) = 0, \tag{3.34}$$

$$\lim_{t \to \infty} \Delta m(t) = 0. \tag{3.35}$$

Additional PE arguments beyond the scope of this chapter are required to show global asymptotic stability of the sensor biases; however preliminary numerical simulations and experimental results both demonstrate the bias observer to be asymptotically stable when the IMU sensor measurements are PE.

3.4 Simulation Evaluation

This section reports a preliminary evaluation of the bias-observer for 9-axis IMUs, described in Section 3.3, with numerical simulations.

3.4.1 Simulation Setup

The sensor bias observer was evaluated in two numerical simulations.

- Sensor measurement sampling was simulated at 100Hz.

- The observer gains used during the simulations are:

$$k_a = 1 \tag{3.36}$$

$$k_m = 1 \tag{3.37}$$

$$K_{b_w} = \begin{bmatrix} 0.025 & 0 & 0 \\ 0 & 0.025 & 0 \\ 0 & 0 & 0.125 \end{bmatrix} \tag{3.38}$$

$$K_{b_a} = \begin{bmatrix} 0.1 & 0 & 0 \\ 0 & 0.1 & 0 \\ 0 & 0 & 2 \end{bmatrix} \tag{3.39}$$

$$K_{b_m} = \begin{bmatrix} 0.5 & 0 & 0 \\ 0 & 0.5 & 0 \\ 0 & 0 & 5 \end{bmatrix} \tag{3.40}$$

- Simulations include sensor measurements with sensor noise representative of the LORD MicroStrain 3DM-GX3-25 AHRS (LORD Sensing, Williston, VT, USA) [39] — $\sigma_a = 0.00065$ g, $\sigma_w = 0.005$ rad/s, $\sigma_m = 0.001$ gauss.

- The simulation measurements include the sensor biases of:

$$w_b = \begin{bmatrix} 4 & -2 & 1 \end{bmatrix}^T /1000 \text{ rad/s}, \tag{3.41}$$

$$a_b = \begin{bmatrix} 2 & -1 & 1 \end{bmatrix}^T /1000 \text{ g}, \tag{3.42}$$

$$m_b = \begin{bmatrix} 2 & -5 & 3 \end{bmatrix}^T /10 \text{ gauss}. \tag{3.43}$$

- Simulations were for a latitude of 39.32°N and a longitude of 76.62°W.

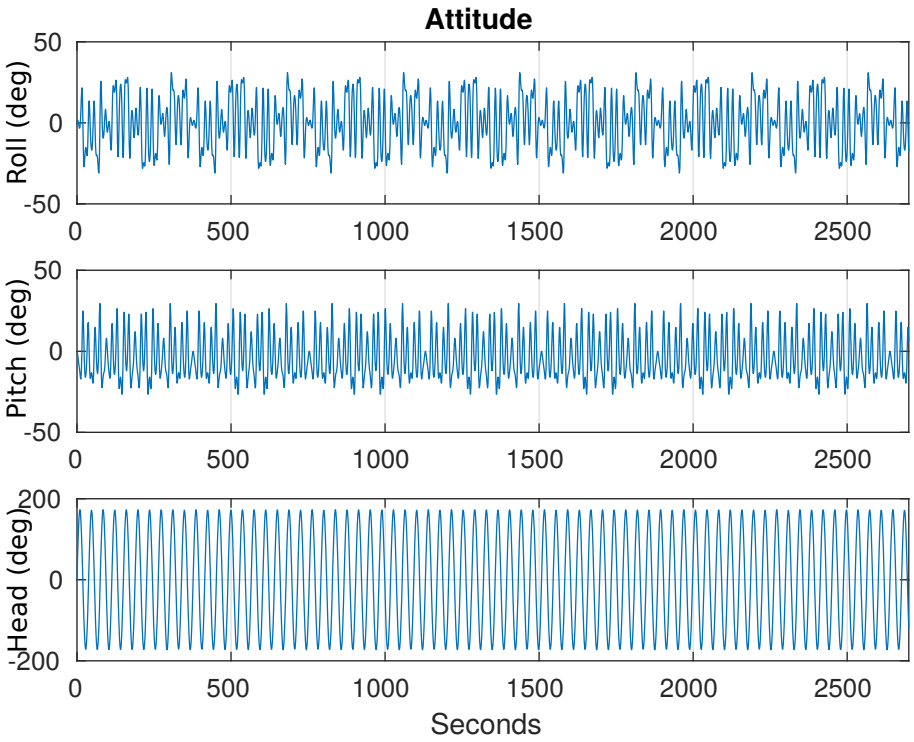

Figure 3.1: Attitude of the 9-DOF IMU during the Sim1 simulation.

- In Sim1, the simulated instrument is subject to roll and pitch changes of $\sim \pm 25^{\circ}$ and heading changes of $\sim \pm 180^{\circ}$. Figure 3.1 show the attitude of the instrument in Sim1.

- In Sim2, the simulated instrument experiences roll changes of $\sim \pm 100^{\circ}$, pitch changes of $\sim \pm 50^{\circ}$, and heading changes of $\sim \pm 180^{\circ}$. Figure 3.2 show the attitude of the instrument in Sim2.

3.4.2 Simulation Results

The estimated sensor bias errors for the two simulations are shown to converge to zero in Figures 3.3-3.5. Figure 3.3 reports the estimated accelerometer bias

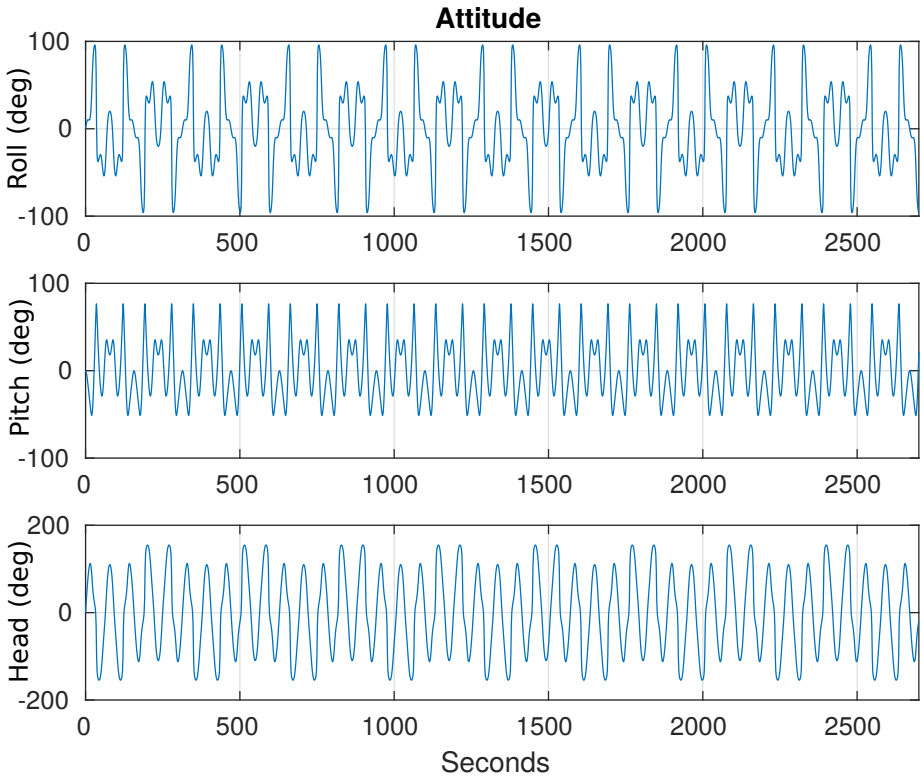

Figure 3.2: Attitude of the 9-DOF IMU during the Sim2 simulation.

error, Figure 3.4 reports the estimated angular-rate gyro bias error, and Figure 3.3 reports the estimated magnetometer hard-iron bias error. The reported bias errors converge to zero, demonstrating the convergence of the estimate sensor bias terms to their true values. In Sim1 and Sim2, all of the sensor biases converge. Sim1's sensor biases converge in $\sim$ 30 minutes, and in Sim2, the sensor biases converge within 10 minutes. The slow convergence of the Sim1 accelerometer's z-component when compared to Sim2 is due to the smaller attitude changes that the instrument is experiencing. In Sim1, the instrument experiences roll and pitch changes of $\sim \pm 25^{\circ}$, while in Sim2, the instrument experiences changes of $\sim \pm 90^{\circ}$. Like many adaptive identifiers, the rate of

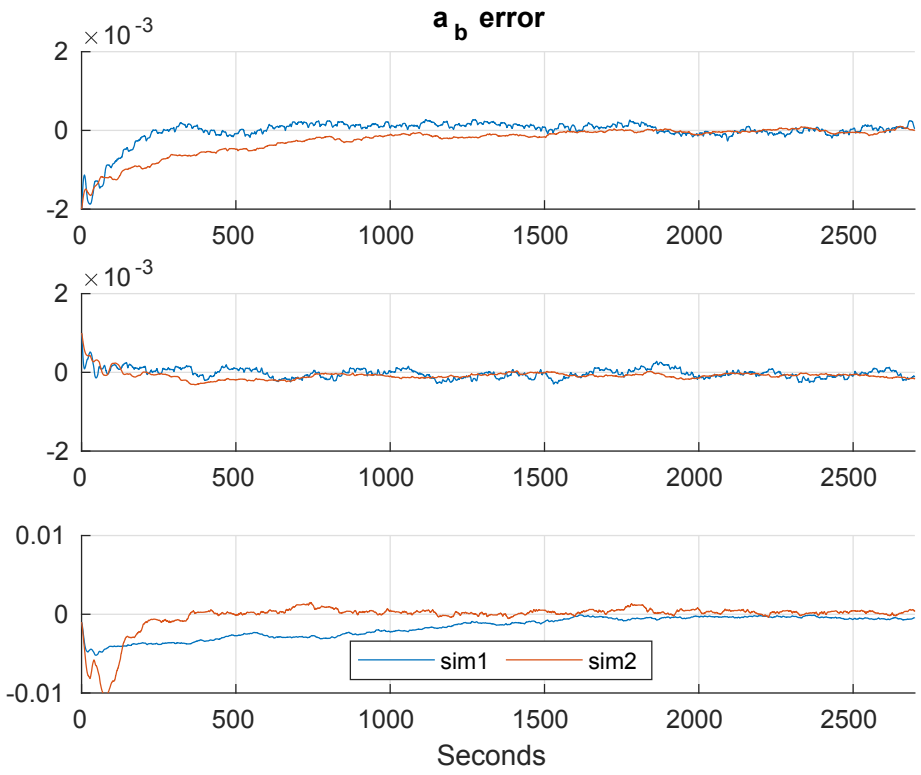

Figure 3.3: The accelerometer sensor bias estimate error is shown to converge to zero, demonstrating convergence of the estimated parameter to its true value.

convergence is a function of the degree of PE that the system is receiving. Hence, the biases converge faster in Sim2 when compared to Sim1 because Sim2 is experiencing larger changes in attitude.

Sim1 and Sim2 demonstrate convergence of the 9-DOF IMU's sensor biases while employing the reported adaptive observer. The simulation results suggest the practical utility of using the observer reported in Section 3.3 to conduct real-time sensor bias estimation in 9-DOF IMUs.

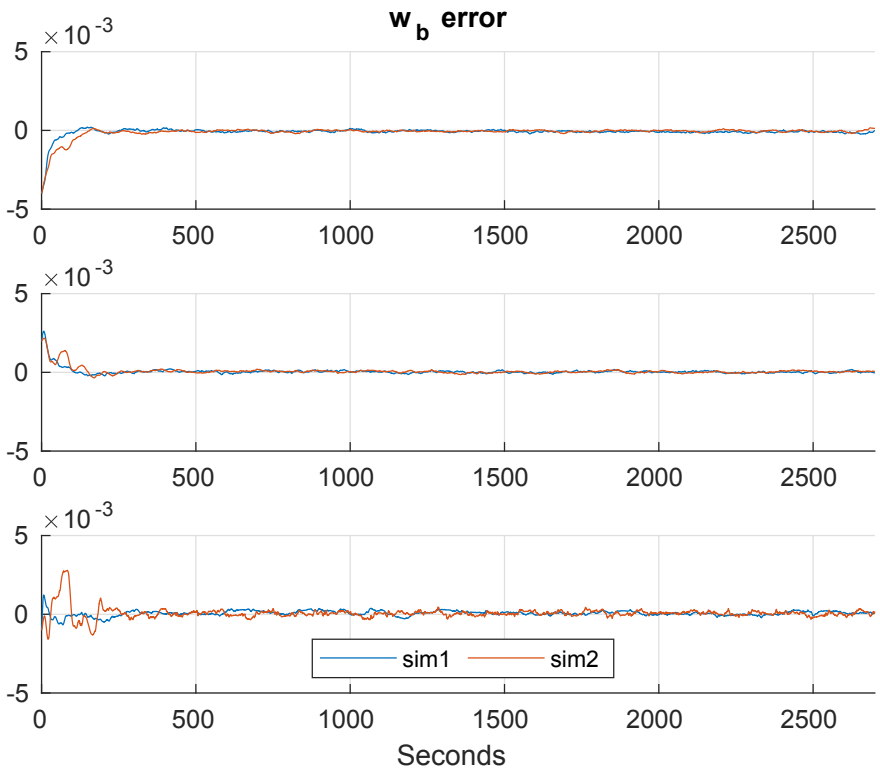

Figure 3.4: The angular-rate sensor bias estimate error is shown to converge to zero, demonstrating convergence of the estimated parameter to its true value.

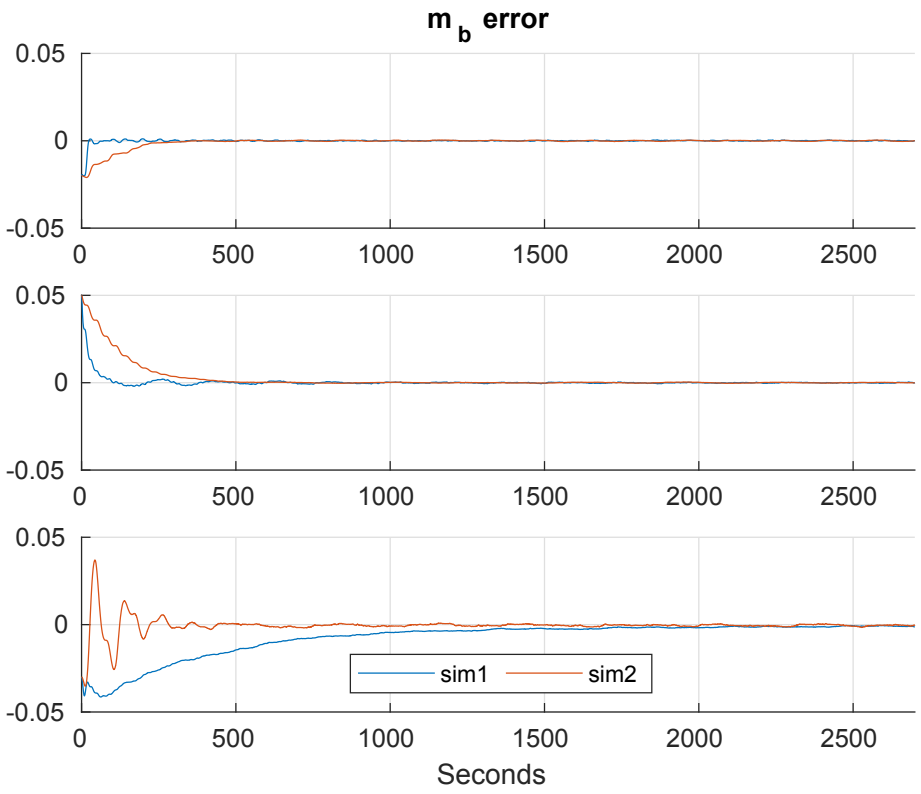

Figure 3.5: The hard-iron magnetometer sensor bias estimate error is shown to converge to zero, demonstrating convergence of the estimated parameter to its true value.

3.5 Experimental Evaluation

This section reports a preliminary evaluation of the bias-observer for 9-axis IMUs, described in Section 3.3, in a full-scale experimental trial with an IMU on an UV.

3.5.1 Test Facility

An experimental trial was performed with the Johns Hopkins University (JHU) remotely operated vehicle (ROV) equipped with a LORD MicroStrain 3DM-GX3-25 AHRS (LORD Sensing, Williston, VT, USA) [39] in the facility's 7.5 m diameter $\times$4 m deep fresh water tank. See Appendix A on page 189 for more information on the JHU ROV and the JHU hydrodynamic test facility (HTF).

3.5.2 Experimental Setup

The gyrocompass system is evaluated with a preliminary vehicle trial employing a LORD MicroStrain 3DM-GX3-25 AHRS [39].

- The observer gains used during the simulations are the same ((3.36)-(3.40)) as those used in the Sim1 and Sim2 simulations.
- Exp1 was conducted at a latitude of 39.32°N and a longitude of 76.62°W.
- The IMU was sampled at 100Hz.
- The ROV was commanded to execute smooth sinusoidal rotations ($\sim$ 180° in heading and $\sim$ 10° in roll and pitch) while in closed-loop control. The attitude of the instrument is reported in Figure 3.6.

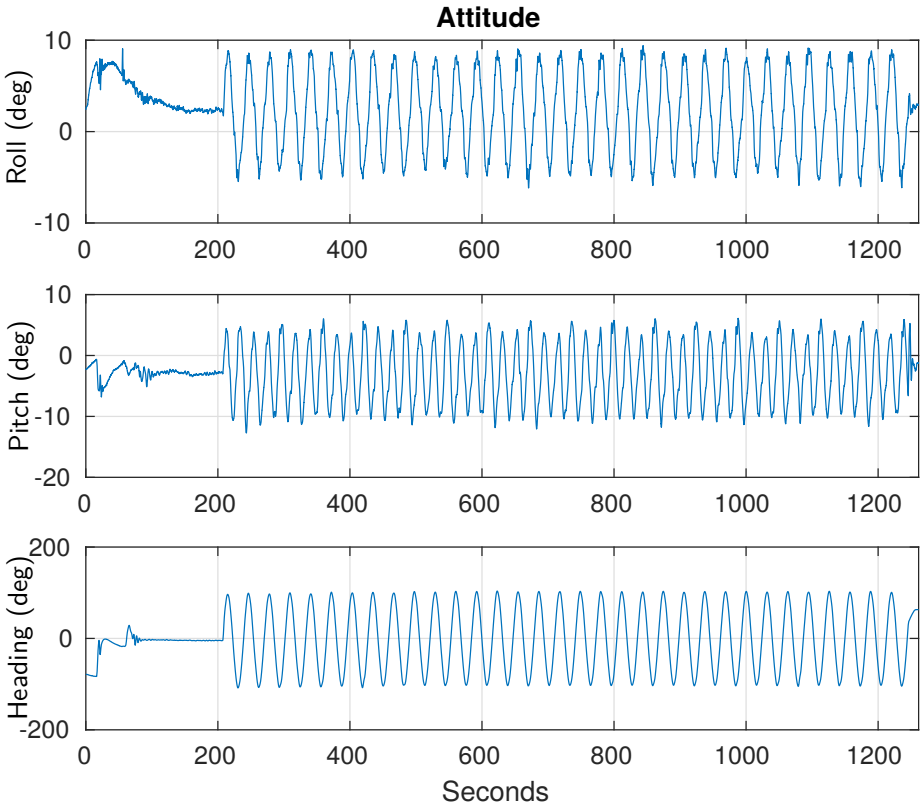

Figure 3.6: Vehicle attitude during the laboratory experiment.

3.5.3 Experimental Results

The laboratory experiment's sensor bias estimates are shown in Figures 3.7-3.9. Figure 3.7 reports the estimated accelerometer bias, Figure 3.8 reports the estimated angular-rate gyro bias, and Figure 3.9 reports the estimated magnetometer hard-iron bias. The results show that during this experimental evaluation of the reported sensor bias observer, the sensor biases converge. In this preliminary result, the observer took $\sim$ 10 minutes to converge. This is consistent with the convergence time of Sim2.

The experimental evaluation suggest the practical utility of using the

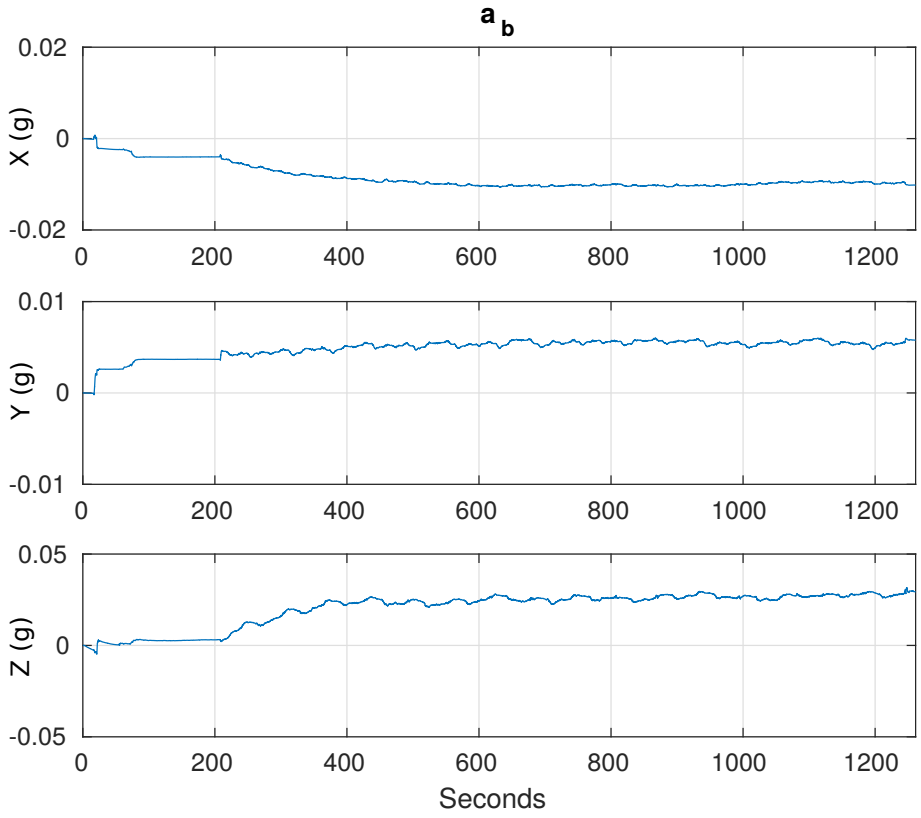

Figure 3.7: IMU accelerometer sensor bias estimation during the laboratory experiment.

observer to conduct real-time sensor bias estimation in 9-DOF IMUs. We are currently investigating improvements to the observer's adaptive gains to improve its rate of convergence.

3.6 Conclusion

This chapter reports the derivation and stability proof of an adaptive observer for sensor biases in 9-DOF IMUs. Preliminary simulations and a preliminary experimental evaluation using a MicroStrain 3DM-GX3-25 AHRS are

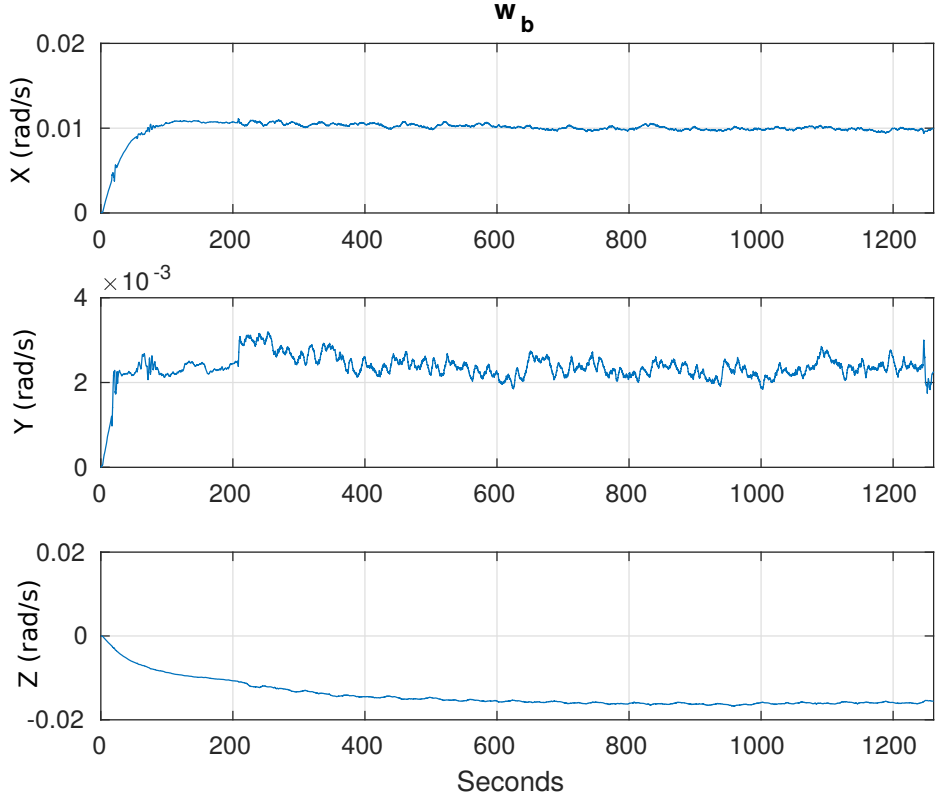

Figure 3.8: IMU angular rate gyro sensor bias estimation during the laboratory experiment.

presented.

The preliminary simulations and vehicle trial suggest, for the case of a rotating IMU, the asymptotic convergence of the sensor biases to their true values. Both the simulations and vehicle experiment demonstrate convergence of the sensor biases within $\sim$ 10 minutes.

In future studies, the author hopes to improve the time of convergence, extend proof to analytically show asymptotic stability of the sensor biases, and do thorough vehicle trials both in the lab and in the field.

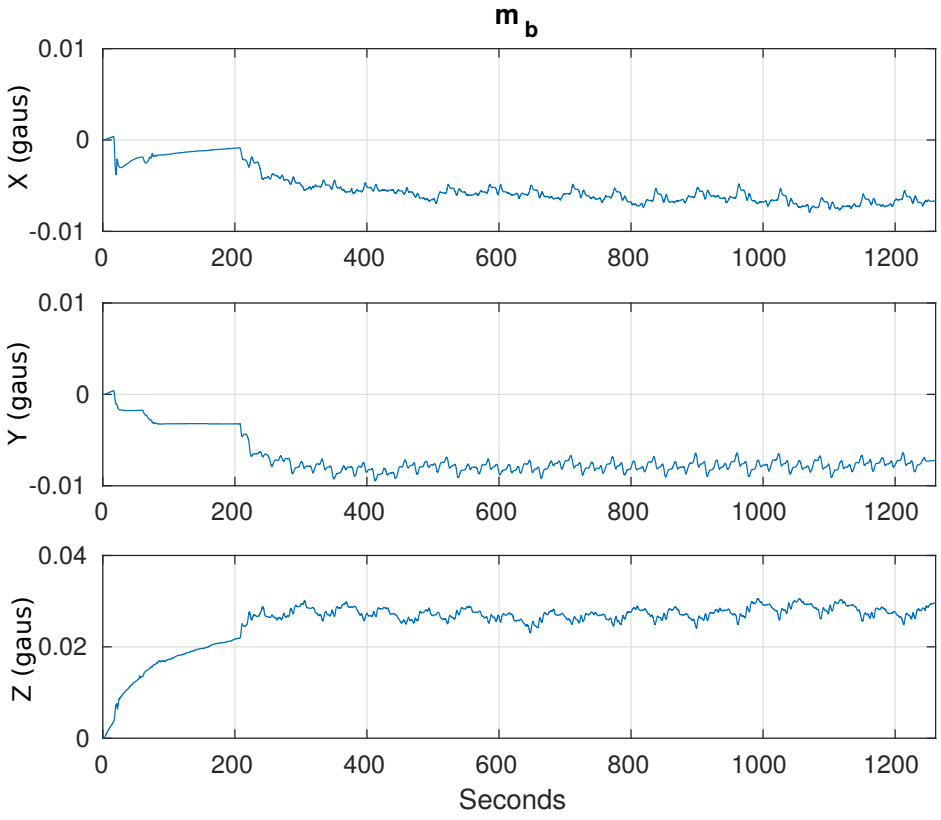

Figure 3.9: IMU magnetometer hard-iron sensor bias estimation during the laboratory experiment.

Chapter 4

A Stable Adaptive Observer for Hard-Iron and Soft-Iron Bias Calibration and Compensation for Two-Axis and Three-Axis Magnetometers

4.1 Introduction

This chapter is based on the research originally reported in [62]. Dynamic instrumentation and estimation of vehicle attitude, especially geodetic heading, is critical to the accurate navigation of land, sea, and air vehicles in dynamic motion. Many of these land and sea vehicles are passively stable in roll and pitch, and hence, experience relatively modest changes in roll and pitch during normal operation (e.g. surface vehicles, autonomous underwater vehicles (AUVs), and underwater remotely operated vehicles (ROVs)). For this class of vehicles, it is possible to use 2-axis magnetometers for estimating the heading of the vehicle. However, the accurate magnetic heading estimation is

commonly vitiated by very significant hard-iron and soft-iron magnetometer biases.

This chapter reports a novel adaptive observer for real-time estimation of 2-axis magnetometer hard-iron and soft-iron iron biases of *dynamic* (rotating and translating) 2-axis magnetometers without *a priori* knowledge of the instrument's attitude or the instrument's local magnetic field vector. Unlike previous on-line approaches which utilize the EKF, global stability of the error system is proved. Moreover, under a persistently exciting (PE) condition, the error system is shown to be globally asymptotic stable, and the sensor bias estimates are shown to converge to the true bias values. We report performance analyses in a numerical simulation study and in an actual full-scale experimental trial with a 2-axis magnetometer on the Johns Hopkins University (JHU) remotely operated vehicle (ROV) (Appendix A, Figure A.2).

Advantages of the proposed approach include the following: (i) knowledge of the instrument attitude or angular velocity is not required for sensor bias estimation, (ii) zero *a priori* knowledge of the local magnetic field vector magnitude or vector direction is needed, (iii) the system is shown to be globally stable, (iv) the error system is shown to be globally asymptotically stable when the measured magnetometer signal is PE. (v) magnetometer hard-iron and soft-iron bias compensation is shown to dramatically improve dynamic heading estimation accuracy.

4.1.1 Background and Motivation

Accurate sensing and estimation of heading is critical for precise navigation of a wide variety of vehicles. The need for accurate heading estimation is particularly acute in the case of vehicles operating in GPS-denied environments such as underwater. Small low-cost UVs commonly employ MEMS magnetometers to estimate local magnetic heading typically to within several degrees of accuracy, but require careful soft-iron bias and hard-iron bias calibration and compensation to achieve these accuracies. Moreover, magnetic heading sensors must be re-calibrated for soft-iron and hard-iron bias whenever the vehicle's physical configuration changes significantly (i.e. sensors or other payloads added or removed, etc.), as very frequently occurs on oceanographic marine vehicles. Studies have shown that the accuracy of these magnetic heading sensors can be a principal error source in overall navigation solutions [30]. Thus, when employing magnetic heading sensors it is essential to accurately estimate sensor biases in order to achieve high accuracy heading estimation.

In the design of surface and underwater oceanographic vehicles, great care is taken to isolate and separate on-board magnetic compasses from any possible time-varying on-board magnetic disturbance sources. Active electro-magnetic components are chosen to have closed magnetic flux-paths, and magnetic compass heading are located as far as possible from on-board passive magnetic, passive permeable, and active electro-magnetic components. With proper design, time-varying on-board magnetic disturbance can be rendered negligible. What remains an ubiquitous problem, however, and is the focus of this chapter, is the estimation and compensation for the the effects of the

magnetic bias ("hard iron") and permeability ("soft iron") of the entire vehicle on the compass heading.

4.1.2 Literature Review

Several methods for magnetometer bias estimation have been reported in recent years. Alonso and Shuster proposed the "TWOSTEP" method [1] for estimating magnetometer hard-iron sensor bias, and in later work, an extended method for calibrating magnetometer scale and orthogonality factors, or soft-iron bias, as well [2]. Vasconselos et al. present bias estimation (hard-iron and soft-iron) as an ellipsoid fitting problem which can be solved with an iterative MLE approach [74]. Many least squares methods are reported for the ellipsoid fitting problem (e.g. [3, 15, 16, 46]) and Wu et al. [79] frame the ellipsoid fitting problem as a particle swarm optimization (PSO). Kok et al. [31] and Li and Li [33] fuse accelerometer measurements with magnetometer measurements to estimate magnetometer sensor bias, and Papafotis and Sotiriadis [48] report an algorithm for three-axis accelerometer and magnetomoter calibration using a gradient decent method. These methods, however, are batch estimators that are not practical for on-line estimation of magnetometer sensor bias. In order to be used in real time, these methods most be modified to run over a sliding window or with an iterative approach.

Sensor biases change over time due to changes in sensor payload, temperature, local field disturbances, etc., which make it imperative to estimate sensor biases in real time. In [61, 70] the authors report adaptive methods utilizing magnetometer and gyroscope measurements for estimating 3-axis

magnetometer hard-iron sensor biases, but these approaches do not address soft-iron bias estimation.

Crassidis et al. report an extension to the TWOSTEP method based on the EKF [11] and Guo et al. present an alternative EKF approach for doing magnetometer sensor bias estimation [19]. Han et al. [21] report a gyroscope-aided EKF method for magnetic calibration. However, these studies do not report analytical guarantees of the stability or the convergence of the sensor biases to their true values.

Soken and Sakai [56] report a magnetometer calibration method using the TRIAD algorithm and an unscented Kalman filter (UKF). However, this method requires knowledge of the initial attitude of the instrument, has a slow convergence time, and the study reports no stability guarantees.

The present chapter reports a novel method for real-time soft-iron and hard-iron bias calibration for 2-axis magnetometers utilizing only biased measurements from a 2-axis magnetometer. The proposed algorithm is shown to be globally asymptotically stable when the measured magnetometer is PE, does not require local field information for calibrating the measured magnetic field vector direction, does not require any knowledge of the instrument's attitude or angular velocity, and can easily be implemented on-line in real-time.

4.1.3 Chapter Outline

This chapter is organized as follows: Section 4.2 gives an overview of the magnetometer measurement model. Section 4.3 reports the adaptive soft and

hard iron observer and Section 4.4 reports a least squares approach. Section 4.5 presents numerical simulation evaluation of the observer. Section 4.6 reports a full scale vehicle trial. Section 4.7 presents a 3-axis version of the adaptive observer. Section 4.8 summarizes and concludes.

4.2 Magnetometer Measurement Model

Magnetometers (including those employed in IMUs) are subject to two primary sensor calibration errors: hard-iron and soft-iron. Hard-iron errors are constant magnetometer sensor bias terms due to the permanent magnetic signature of the instrument and the vehicle. Soft-iron errors are non-constant magnetometer sensor bias terms due to the magnetic permeability of the instrument and the vehicle, and will vary with vehicle heading and attitude. For most IMU magnetometers, hard-iron errors dominate soft-iron errors.

We define the following measurement model for 2-axis magnetometers:

$$m_m(t) = T m_t(t) + b \tag{4.1}$$

where $m_m(t) \in \mathbb{R}^2$ is the noise-free magnetometer measurement, $m_t(t) \in \mathbb{R}^2$ is Earth's true magnetic field, $T \in \mathbb{R}^{2\times 2}$ is a diagonally-dominant PDS matrix representing soft-iron bias, and $b \in \mathbb{R}^2$ represents the magnetometer hard-iron bias.

4.3 Adaptive Soft-Iron and Hard-Iron Bias Observer

This section reports the derivation of a novel on-line adaptive observer for hard-iron and soft-iron magnetometer biases in 2-axis magnetometers. The biases are assumed to be very slowly time varying, and hence we model them as constant terms and update the estimates continuously.

4.3.1 Magnetometer Bias System Model

We can rearrange (4.1) as

$$m_t(t) = T^{-1}\left(m_m(t) - b\right). \tag{4.2}$$

Taking the inner product of (4.2) with itself results in

$$\|m_t(t)\|^2 = \left(m_m(t) - b\right)^T T^{-2}\left(m_m(t) - b\right) \tag{4.3}$$

$$= m_m^T(t)T^{-2}m_m(t) - 2m_m^T(t)T^{-2}b + b^T T^{-2}b. \tag{4.4}$$

Subtracting $b^T T^{-2} b$ from both sides results in

$$\phi = m_m^T(t)T^{-2}m_m(t) - 2m_m^T(t)T^{-2}b \tag{4.5}$$

where $\phi = \|m_t(t)\|^2 - b^T T^{-2} b$. Dividing both sides of (4.5) by ϕ results in

$$1 = m_m^T(t)\Gamma m_m(t) - 2m_m^T\alpha \tag{4.6}$$

where $\Gamma \in \mathbb{R}^{2\times 2}$ and $\alpha \in \mathbb{R}^2$ are defined as

$$\Gamma = T^{-2}/\phi \tag{4.7}$$

and

$$\alpha = T^{-2}b/\phi. \tag{4.8}$$

We note that this approach only works when ϕ is not close to zero. Thus, we require that the hard-iron bias is smaller than the magnitude of the true magnetic field vector. Fortunately, this condition is true for most magnetometers.

Using the identity

$$\text{vec}\,(AXB) = \left(B^T \otimes A\right) \text{vec}\,(X) \tag{4.9}$$

(4.6) can be written as

$$1 = \begin{bmatrix} m_m^T(t) \otimes m_m^T(t) & -2m_m^T(t) \end{bmatrix} \begin{bmatrix} \text{vec}\,(\Gamma) \\ \alpha \end{bmatrix} \tag{4.10}$$

where $\otimes$ is the Kronecker product and vec $(\cdot)$ is the vectorization (or "stack") operator [55].

Using the common assumption that the soft-iron bias term T is a PDS matrix, Γ is parameterized as

$$\Gamma = \begin{bmatrix} a & c \\ c & b \end{bmatrix}. \tag{4.11}$$

Using this parameterization and rearranging terms in (4.10), the system model becomes

$$1 = w^T(t)\theta \tag{4.12}$$

where

$$w(t) = \begin{bmatrix} m_x^2(t) \\ m_y^2(t) \\ 2m_x(t)m_y(t) \\ -2m_m(t) \end{bmatrix}, \tag{4.13}$$

$$\theta = \begin{bmatrix} t_p \\ \alpha \end{bmatrix}, \tag{4.14}$$

$$t_p = \begin{bmatrix} a \\ b \\ c \end{bmatrix}, \tag{4.15}$$

where $m_x(t) \in \mathbb{R}$ and $m_y(t) \in \mathbb{R}$ are the x and y components of magnetometer measurement signal $m_m(t)$ respectively, $w(t) \in \mathbb{R}^5$ is a known nonlinear time-varying function of the measured magnetometer signal $m_m(t)$, and $\theta \in \mathbb{R}^5$ is a constant vector encoding the true soft-iron and hard-iron bias parameters.

4.3.2 Adaptive Observer for Hard-Iron and Soft-Iron Bias

We note that the algebraic system (4.12) has the same form as the vector input, single output system presented in Chapter 3 of [42]. (4.12) can be rearranged such that the exact true plant takes the form

$$0 = w^T(t)\theta - 1. \tag{4.16}$$

Defining $\hat{\theta}(t)$ as the adaptive identifier's estimate of the (unknown) true

parameter θ, the identifier plant takes the form

$$e(t) = w^T(t)\hat{\theta}(t) - 1 \tag{4.17}$$

$$= w^T(t)\Delta\theta \tag{4.18}$$

where $e(t)$ as the error associated with the identifier plant, and $\Delta\theta(t)$ is the parameter error

$$\Delta\theta(t) = \hat{\theta}(t) - \theta. \tag{4.19}$$

Note that since θ is constant

$$\Delta\dot{\theta}(t) = \dot{\hat{\theta}}(t). \tag{4.20}$$

The adaptive observer's parameter update law for the parameter $\hat{\theta}(t)$ is chosen to be

$$\Delta\dot{\theta}(t) = -Kw(t)e(t) \tag{4.21}$$

$$\dot{\hat{\theta}}(t) = -Kw(t)w^T(t)\hat{\theta}(t) + Kw(t) \tag{4.22}$$

where $K \in \mathbb{R}^{5\times5}$ is a constant PDS adaptation gain matrix.

4.3.3 Stability Analysis

Consider the Lyapunov function candidate

$$V = \frac{1}{2}\Delta\theta^T(t)K^{-1}\Delta\theta(t). \tag{4.23}$$

where V is a positive definite, C^1, and radially unbounded function by construction. The time derivative of (4.23) is

$$\dot{V} = \Delta\theta^T(t)K^{-1}\Delta\dot{\theta}(t) \tag{4.24}$$

$$= -\Delta\theta^T(t)w(t)e(t) \tag{4.25}$$

$$= -\Delta\theta^T(t)w(t)w^T(t)\Delta\theta(t) \tag{4.26}$$

$$\leq 0. \tag{4.27}$$

Thus $\dot{V}$ is negative semi-definite, and the error system (4.21) is globally stable. If, in addition, $w(t)$ is PE [42, 52], the error system is globally asymptotically stable. That is, if there exists finite $\alpha, \beta, T > 0$ such that

$$\alpha I \leq \int_t^{t+T} w(\tau)w^T(\tau)\,d\tau \leq \beta I \tag{4.28}$$

for all $t \geq 0$ and I is the identity matrix, then the proposed observer is globally asymptotically stable and $\lim_{t\to\infty}\hat{\theta}(t) = \theta$. It is unclear how to show analytically that a PE $m_m(t)$ signal implies that $w(t)$ is PE. We were able to check numerically, however, that a variety of PE $m_m(t)$ signals all resulted in a PE $w(t)$, thus satisfying the conditions of (4.28). Moreover, the resulting numerically simulated system and the experimentally evaluated systems were both observed to be asymptotically stable.

4.4 Least Squares Soft-Iron and Hard-Iron Estimation

This section reports the derivation of a least squares approach for hard-iron and soft-iron magnetometer biases in 2-axis magnetometers to be used as a comparison to the adaptive observer presented in the previous section. As in the previous section, the biases modeled as constant terms.

From (4.12), the i^{th} measurement satisfies

$$1 = w_i^T \theta \tag{4.29}$$

where

$$w_i = \begin{bmatrix} m_{x,i}^2 \\ m_{y,i}^2 \\ 2m_{x,i}m_{y,i} \\ -2m_{m,i} \end{bmatrix}, \tag{4.30}$$

$m_{m,i}$ is the i^{th} magnetometer measurement and $m_{x,i}$, $m_{y,i}$ are the x and y components of $m_{m,i}$ respectively. By arranging the w_i vectors such that

$$W^T = \begin{bmatrix} w_1^T \\ w_2^T \\ \vdots \\ w_n^T \end{bmatrix} \tag{4.31}$$

(4.29) can be rewritten as

$$\begin{bmatrix} 1 \\ 1 \\ \vdots \\ 1 \end{bmatrix} = \begin{bmatrix} w_1^T \\ w_2^T \\ \vdots \\ w_n^T \end{bmatrix} \theta \tag{4.32}$$

$$= W^T \theta. \tag{4.33}$$

The least squares solution θ^* is then found by Moore-Penrose inverse

$$\theta^* = \left(WW^T\right)^{-1} W \begin{bmatrix} 1 \\ 1 \\ \vdots \\ 1 \end{bmatrix}. \tag{4.34}$$

4.5 Numerical Simulation Evaluation

The instantaneous estimated heading can then be computed as

$$\hat{\gamma} = atan2\left(-m_y, m_x\right) - \gamma_0, \text{ [71]} \tag{4.35}$$

where γ_0 is the known local magnetic variation and where $m_x \in \mathbb{R}$, $m_y \in \mathbb{R}$ are the x and y components, respectively, of the m_t signal.

4.5.1 Simulation Setup

The magnetometer sensor bias observer is evaluated in a numerical simulation.

- Sensor measurements were simulated to represent the magnetometer of the KVH 1775 IMU (KVH Industries, Inc., Middletown, RI, USA) [32].
- Magnetometer sensor measurement sampling was simulated at 20 Hz.

- Simulated magnetometer measurements include sensor noise of $\sigma_m = 0.002$ Gauss (G) which is consistent with the KVH 1775 IMU.

- The simulated hard-iron magnetometer measurement bias was

$$b = \begin{bmatrix} 0.06 \\ -0.07 \end{bmatrix} \text{G} \tag{4.36}$$

  which is consistent with hard-iron biases observed experimentally with the KVH 1775 IMU.

- The simulated soft-iron magnetometer measurement bias was

$$T = \begin{bmatrix} 1.1 & 0.2 \\ 0.2 & 0.95 \end{bmatrix}. \tag{4.37}$$

- Simulations were for a latitude of 39.32°N and a longitude of 76.62W.

- The simulated instrument was commanded to execute smooth sinusoidal rotations of roughly $\pm 300°$ in heading. Figure 4.4 reports the instrument's attitude during the first 35 seconds of the simulation with a period of of rotation of ~ 31 seconds.

- The observer's initial conditions were set to

$$\hat{\theta}(t_0) = \begin{bmatrix} 1 & 1 & 0 & 0 & 0 \end{bmatrix}^T / \phi \tag{4.38}$$

  where

$$\phi = \|m_t\|^2 \tag{4.39}$$

$$= \| \begin{bmatrix} 0.205796 & -0.040654 \end{bmatrix} \|^2 \text{ G}^2. \tag{4.40}$$

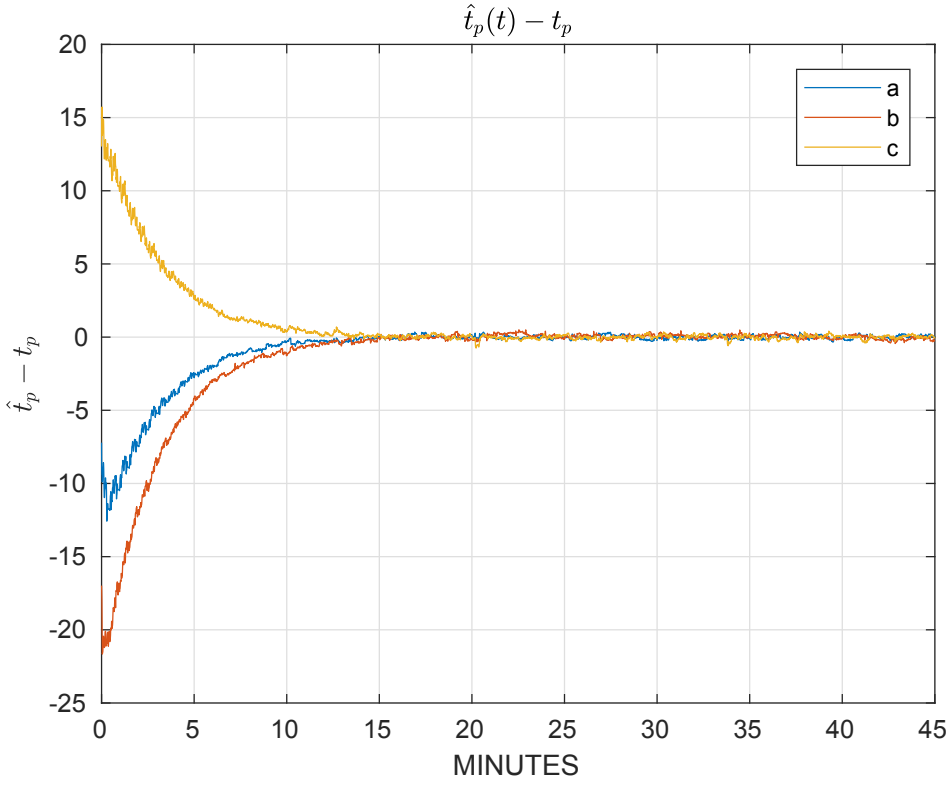

Figure 4.1: Simulation: The parameter error of the estimated $\hat{t}_p(t)$ from the true value t_p. a, b, c are the components of t_p as defined in (4.15).

- The gain matrix used during the simulation was

$$K = diag\left(\begin{bmatrix} 100 & 100 & 100 & 1 & 1 \end{bmatrix}\right). \tag{4.41}$$

4.5.2 Simulation Results

Figure 4.1 reports the parameter error of the estimated $\hat{t}_p(t)$ from the true value of t_p, and Figure 4.2 reports the parameter error of the estimated $\hat{b}(t)$ from the true value b where the recovered value for the estimated hard-iron

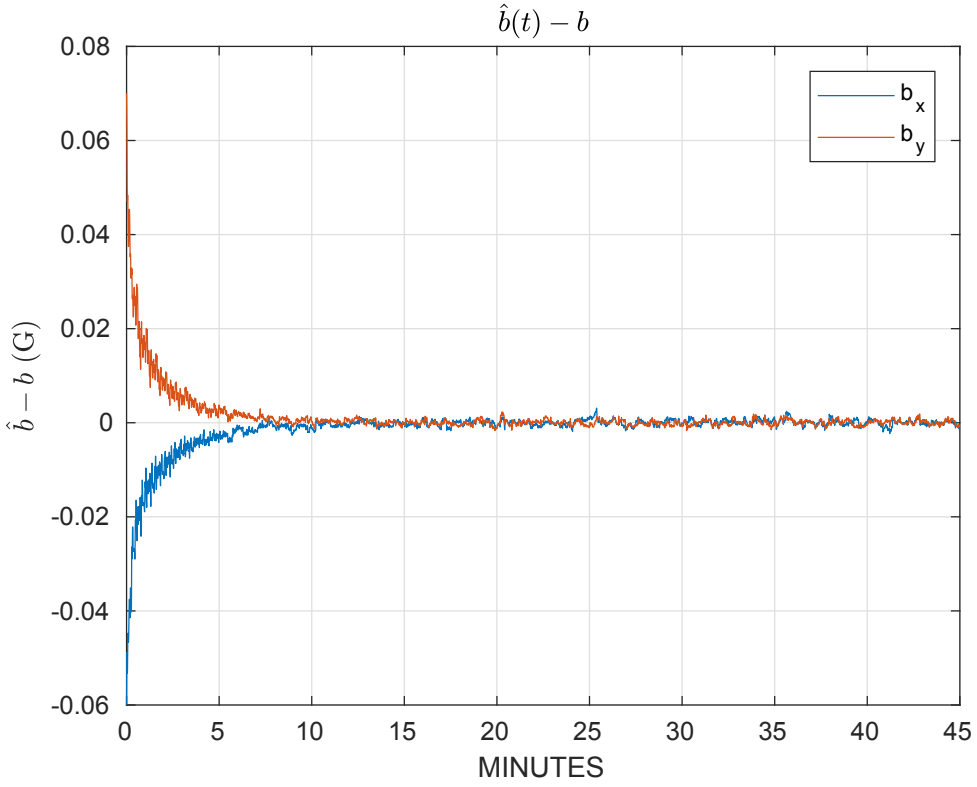

Figure 4.2: Simulation: The parameter error of the estimated $\hat{b}(t)$ from the true value b where b_x, b_y are the x and y components of the hard-iron sensor bias.

bias term $\hat{b}(t)$ is found by

$$\hat{b}(t) = \hat{\Gamma}^{-1}(t)\hat{\alpha}(t). \tag{4.42}$$

The simulation results show that when the magnetometer measurements are PE, the parameter estimates converge to their true values.

Note that Γ is T^{-2} scaled by $1/\phi$. Therefore, in order to recover the true soft-iron bias, T, knowledge of the true magnetic field magnitude is necessary. However, since the calibrated magnetometer measurement is commonly used as a reference direction in AHRSs [20, 78], recovering the true magnitude of

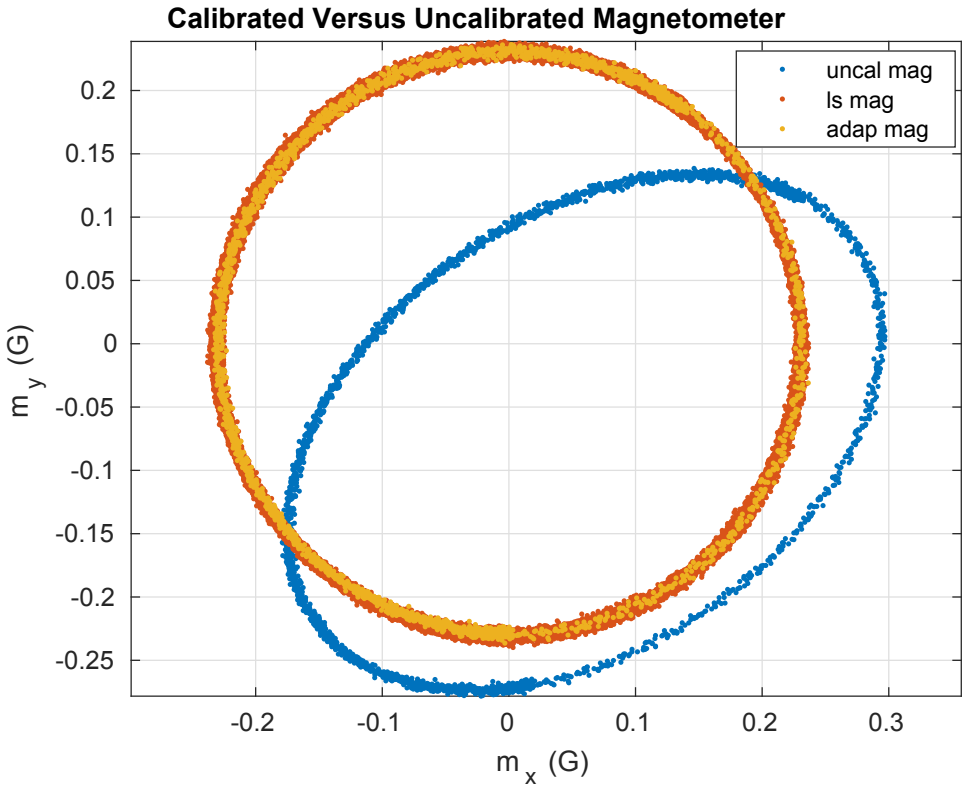

Figure 4.3: Simulation: Comparison of the uncalibrated (uncal), least squares (ls) calibrated, and adaptive observer (adap) calibrated magnetometer measurements.

T is **not** critical to the accurate estimation of heading. However, if $\|m_t(t)\|$ is known (For field vehicles, the local magnetic field strength is commonly estimated by magnetic field models like the World Magnetic Model (WMM) [43] or the International Geomagnetic Reference Field (IGRF) model [68].), ϕ can be recovered by

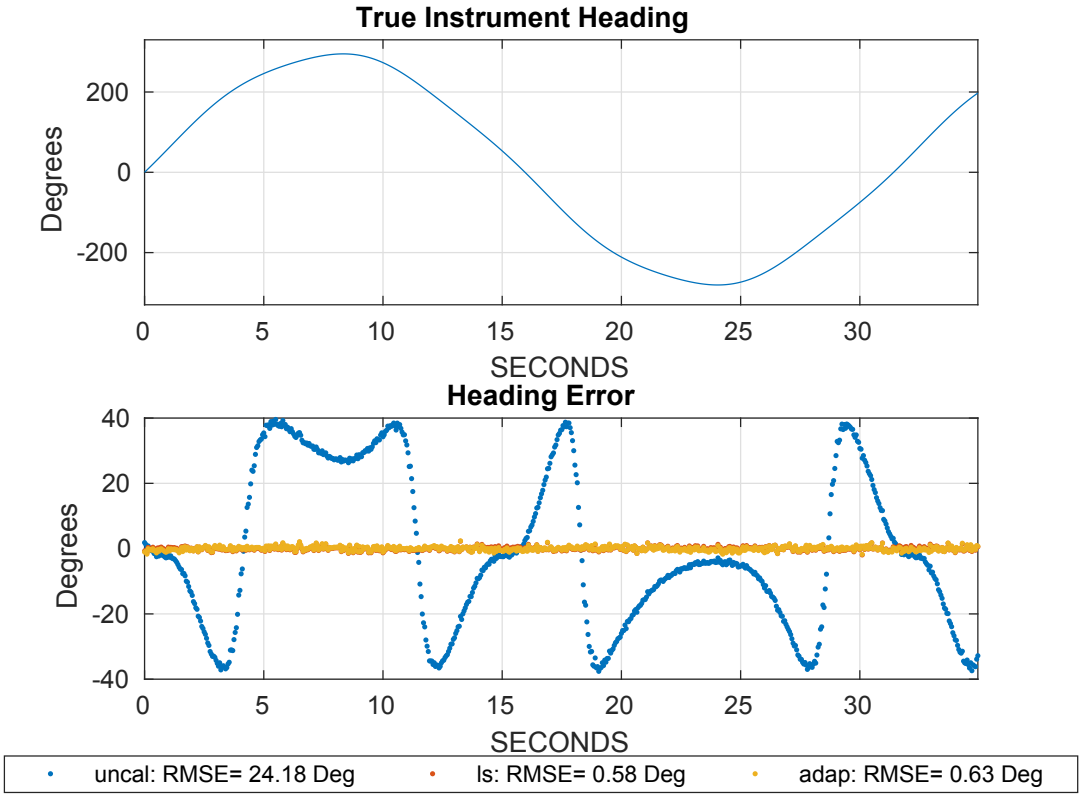

Figure 4.4: Simulation: *Top:* The true instrument heading from the first 35 seconds of the simulation. *Bottom:* Heading error corresponding to the uncalibrated (uncal), least squares (ls) calibrated, and adaptive observer (adap) calibrated magnetometers during the first 40 seconds of the simulation.

$$\phi = \|m_t\|^2 - b^T T^{-2} b \tag{4.43}$$

$$= \|m_t\|^2 - \phi b^T \Gamma b \tag{4.44}$$

$$= \frac{\|m_t\|^2}{1 + b^T \Gamma b} \tag{4.45}$$

and hence, the true T can be recovered.

Using the simulation's final parameter estimates, $\hat{\Gamma}(t_f)$ and $\hat{b}(t_f)$ to calibrate the magnetometer, the heading estimate of the instrument is calculated by (4.35). Figure 4.3 shows the comparison between the uncalibrated and calibrated magnetometer measurements and Figure 4.4 reports the corresponding heading and heading error during the first 35 seconds of the simulated experiment. The simulation shows that after the sensor bias estimates have converged, the calibrated magnetometer corresponds to a heading RMSE of 0.63°. This is a vast improvement over the heading RMSE 24.2° corresponding to the uncalibrated magnetometer and very close to the error corresponding to the least squares calibrated magnetometer of 0.58°.

4.6 Vehicle Experimental Evaluation

4.6.1 Experimental Test Facility

Experimental trials were performed with the JHU remotely operated vehicle (ROV), equipped with a KVH 1775 IMU (KVH Industries, Inc., Middletown, RI, USA) [32], in the 7.5 m diameter, 4 m deep fresh water test tank in the JHU HTF. The JHU ROV is passively stable in roll and pitch due to a large center-of-gravity to center-of-buoyancy separation, and experiences limited roll and pitch excursions in normal operation. See Appendix A on page 189 for more info on the JHU ROV and the JHU HTF.

4.6.2 Experimental Setup

The adaptive observer for hard-iron and soft-iron magnetometer sensor biases is evaluated with a full scale vehicle trial employing the MEMS magnetometer

in the KVH 1775 IMU.

- The magnetometer was sampled at 20 Hz.
- The magnetometer was aligned via a fixture to the ROV's iXBLUE PHINS inertial navigation system (INS) (iXblue SAS, Cedex, France). The PHINS attitude is used as ground truth during the experimental evaluation of the observer.
- The experiment was conducted at a latitude of 39.32°N and a longitude of 76.62W.
- The JHU ROV was commanded to execute smooth sinusoidal rotations of roughly $\pm 200^{\circ}$ in heading while in closed loop control. Figure 4.9 reports the instrument's attitude during the first 35 seconds of the simulation with a period of of rotation of ~ 65 seconds.
- The initial conditions for the sensor bias estimates are given by (4.38)-(4.40).
- The gain matrix K used during the vehicle trial was (4.41), the same as in the simulation evaluation.

4.6.3 Experimental Results

The estimated parameters from the experiment are shown in Figures 4.5 - 4.6 where the estimated hard iron bias term $\hat{b}(t)$ is calculated by (4.42). The vehicle trial results show that when the magnetometer measurements are PE, the parameter estimates converge to a steady-state value.

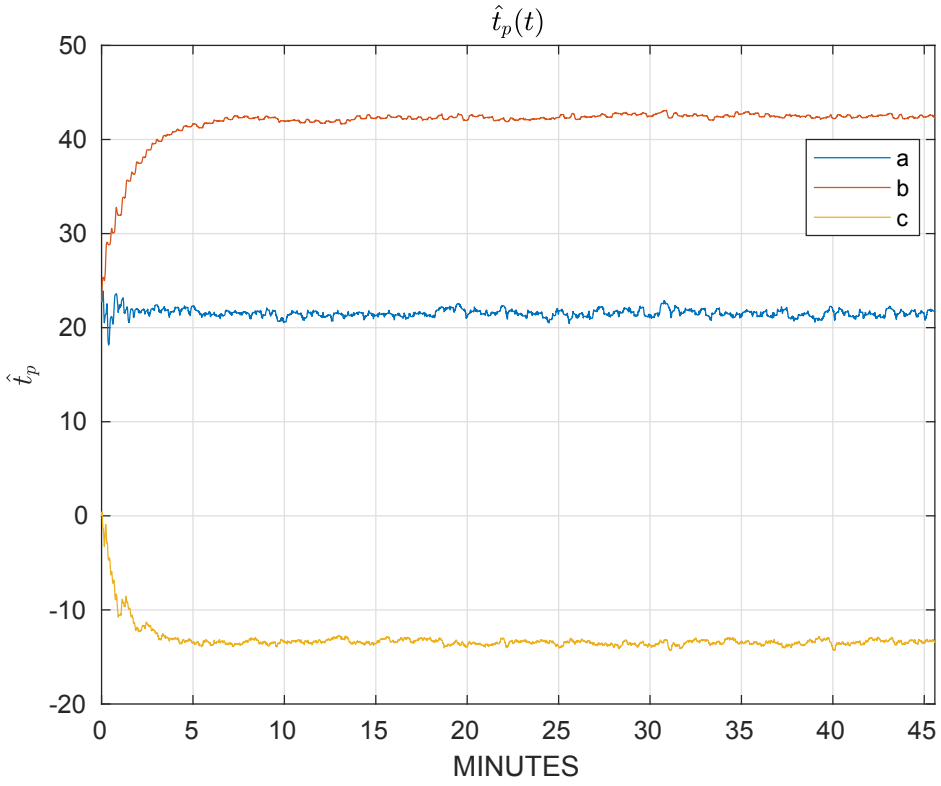

Figure 4.5: Vehicle Trial Experiment: The adaptive observer's estimated $\hat{t}_p(t)$ where a, b, c are the components of t_p as defined in (4.15).

In experimental trials, the true sensor biases are unknown, and thus the accuracy of the estimated biases cannot be measured directly. Instead, the accuracy of the heading estimate is used as an error metric for sensor bias estimation.

As discussed in Section 4.5.2, $\hat{t}_p(t)$ and $\hat{b}(t)$ can be used to calibrate the magnetometer measurements for a calibrated magnetic field reference direction that is used for heading estimation in AHRSs.

Figure 4.7 shows the comparison between the uncalibrated, least squares calibrated, and adaptive observer calibrated magnetometer measurements

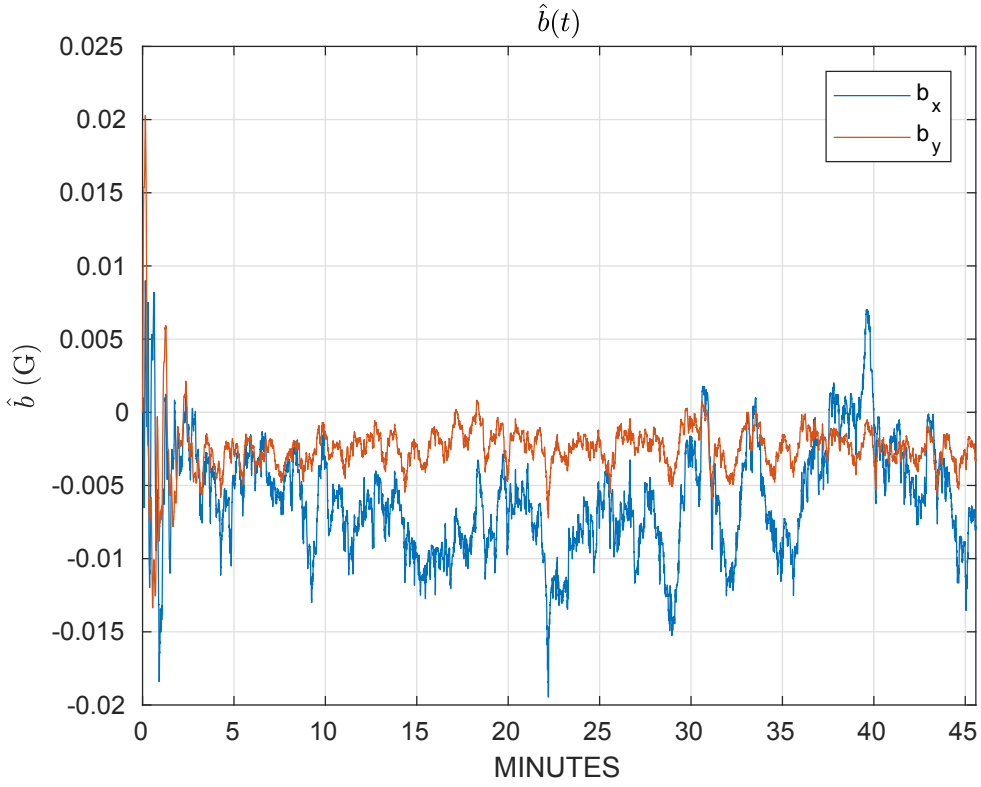

Figure 4.6: Vehicle Trial Experiment: The adaptive observer's estimated $\hat{b}(t)$ where b_x, b_y are the x and y components of the hard-iron sensor bias.

and Figure 4.8 reports the corresponding heading error during the first 400 seconds of the vehicle trial. The experiment shows that the adaptive observer calibrated magnetometer corresponds to a heading RMSE of 1.91°, which is identical to the heading RMSE corresponding to the least squares calibrated magnetometer and much improved over the heading RMSE of 8.77° of the uncalibrated magnetometer.

Figure 4.9 shows the true roll, pitch, and heading of the vehicle during the first 400 seconds of vehicle trial. The vehicle experienced very limited roll and pitch excursions during the vehicle trial.

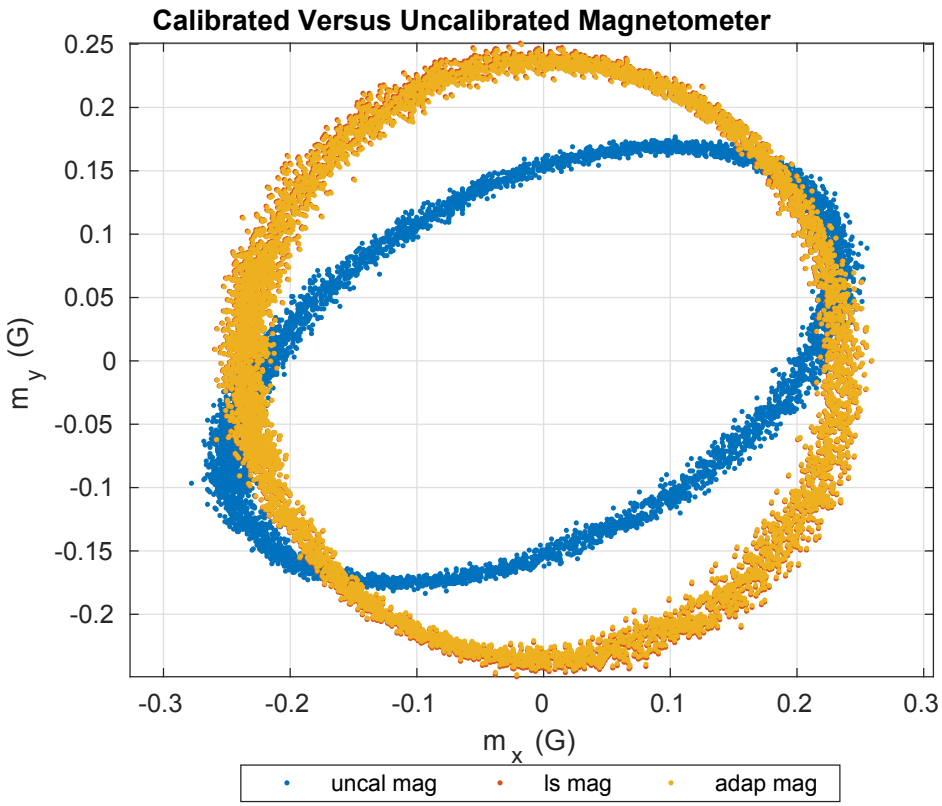

Figure 4.7: Vehicle Trial Experiment: Comparison of the uncalibrated (uncal), least squares (ls) calibrated, and adaptive observer (adap) calibrated magnetometer measurements.

Note that, in this experimental trial, the parameter initial condition was chosen to be far from the true parameter. Because of this, the estimated parameter had to evolve far from the initial condition to the true parameter. Hence, the gain matrix K was chosen to be large to facilitate fast convergence of the parameter. In the presence of measurement noise, smaller gains allow the estimated parameter to converge to a smaller neighborhood of the true parameter than higher gains. However, this increase in accuracy comes with a longer convergence time. The gain matrix K, used in the experimental evaluation, provided a balance of accuracy and fast convergence. It is important to note

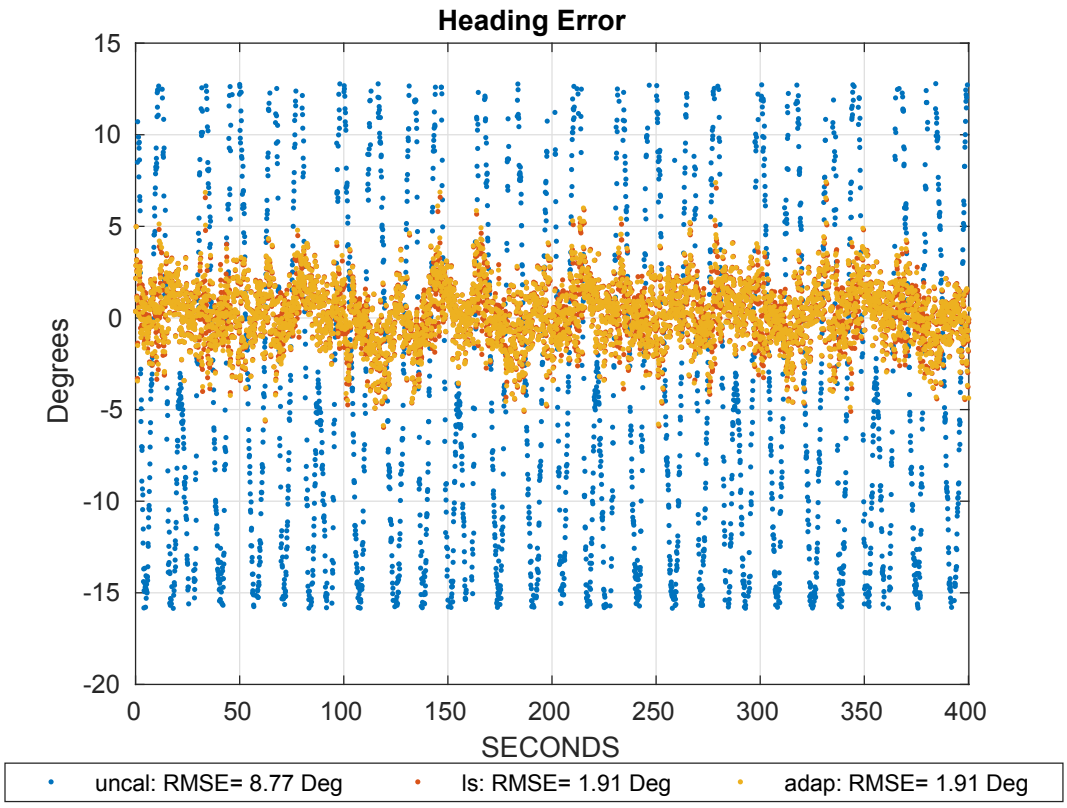

Figure 4.8: Vehicle Trial Experiment: Heading error corresponding to the uncalibrated (uncal), least squares (ls) calibrated, and adaptive observer (adap) calibrated magnetometers during the first 400 seconds of the vehicle trial experiment.

that in adaptive systems there is no method for choosing "ideal" gains. Instead the gain matrix K must be tuned empirically. The sensor noise, the amount of PE the instrument experiences, and the accuracy of the initial guess of the bias terms all affect the rate of convergence and the size of the neighborhood that the estimated parameters converge to. When tuning K, the diagonal gains should be chosen large enough such that the parameters converge to a steady-state neighborhood while small enough that the parameters do not oscillate. This is a balancing act as the higher the gains, the faster the parameters will converge to a neighborhood of the true parameters but the neighborhood will

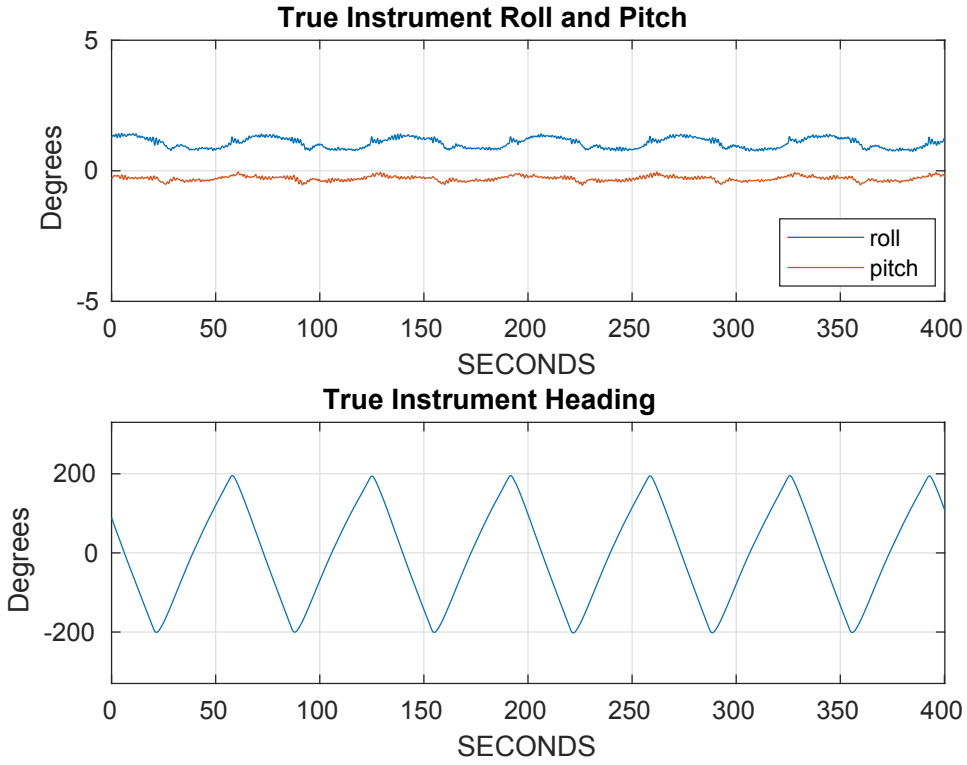

Figure 4.9: True instrument heading, pitch, and roll from the first 400 seconds of the vehicle trial experiment.

be larger. Similarly, the smaller the gains, the slower the convergence, but the neighborhood will be smaller.

In practice, after an initial calibration of the magnetometer, the previous parameter estimate could be used as an initial condition. Thus, after a rough alignment, a smaller gain matrix can be chosen to provide a more accurate estimate of the true parameter.

4.7 Adaptive Observer for Hard-Iron and Soft-Iron Bias for 3-Axis Magnetometers

Note that the algebraic system, (4.12), presented in Section 4.3 can be extended to the 3-axis case. This section reports the derivation of an extension to 3-axis magnetometers of the 2-axis adaptive observer for hard-iron and soft-iron magnetometer sensor biases presented in Section 4.3.

4.7.1 Magnetometer Bias System Model

Similar to (4.1), we define the measurement model for 3-axis magnetometers to be:

$$m_m(t) = Tm_t(t) + b \tag{4.46}$$

where $m_m(t) \in \mathbb{R}^3$ is the noise-free magnetometer measurement, $m_t(t) \in \mathbb{R}^3$ is Earth's true magnetic field, $T \in \mathbb{R}^{3\times 3}$ is a diagonally-dominant PDS matrix representing soft-iron bias, and $b \in \mathbb{R}^3$ represents the magnetometer hard-iron bias.

We can rearrange (4.46) as

$$m_t(t) = T^{-1}\left(m_m(t) - b\right). \tag{4.47}$$

Following the same method presented in Section 4.3, taking the inner product of (4.47) with itself and rearranging terms results in

$$1 = \begin{bmatrix} m_m^T(t) \otimes m_m^T(t) & -2m_m^T(t) \end{bmatrix} \begin{bmatrix} \text{vec}\left(\Gamma\right) \\ \alpha \end{bmatrix} \tag{4.48}$$

where $\phi = \|m_t(t)\|^2 - b^T T^{-2} b$ and $\Gamma \in \mathbb{R}^{2\times 2}$ and $\alpha \in \mathbb{R}^2$ are defined as

$$\Gamma = T^{-2}/\phi \tag{4.49}$$

and

$$\alpha = T^{-2}b/\phi. \tag{4.50}$$

Using the common assumption that the soft-iron bias term T^{-1} is a PDS matrix, Γ is parameterized as

$$\Gamma = \begin{bmatrix} a & d & e \\ d & b & f \\ e & f & c \end{bmatrix}. \tag{4.51}$$

Using this parameterization and rearranging terms in (4.48), the system model becomes

$$1 = w^T(t)\theta \tag{4.52}$$

where

$$w(t) = \begin{bmatrix} m_x^2(t) \\ m_y^2(t) \\ m_z^2(t) \\ 2m_x(t)m_y(t) \\ 2m_x(t)m_z(t) \\ 2m_y(t)m_z(t) \\ -2m_m(t) \end{bmatrix}, \tag{4.53}$$

$$\theta = \begin{bmatrix} t_p \\ \alpha \end{bmatrix}, \tag{4.54}$$

$$t_p = \begin{bmatrix} a \\ b \\ c \\ d \\ e \\ f \end{bmatrix}, \tag{4.55}$$

where $m_x(t) \in \mathbb{R}$, $m_y(t) \in \mathbb{R}$, $m_z(t) \in \mathbb{R}$ are the x, y, z components of magnetometer measurement signal $m_m(t)$ respectively, $w(t) \in \mathbb{R}^9$ is a known nonlinear time-varying function of the measured magnetometer signal $m_m(t)$, and $\theta \in \mathbb{R}^9$ is a constant vector encoding the true soft-iron and hard-iron bias parameters.

4.7.2 Adaptive Observer for Hard-Iron and Soft-Iron Bias

Similar to as in Section 4.3.2, the adaptive observer's parameter update law for the parameter $\hat{\theta}(t)$ is chosen to be

$$\Delta\dot{\hat{\theta}}(t) = -Kw(t)e(t) \tag{4.56}$$

$$\dot{\hat{\theta}}(t) = -Kw(t)w^T(t)\hat{\theta}(t) + Kw(t) \tag{4.57}$$

where $K \in \mathbb{R}^{9\times 9}$ is a constant PDS adaptation gain matrix.

4.7.3 Stability Analysis

Consider the Lyapunov function candidate

$$V = \frac{1}{2}\Delta\theta^T(t)K^{-1}\Delta\theta(t). \tag{4.58}$$

where V is a positive definite, C^1, and radially unbounded function by construction. The time derivative of (4.58) is

$$\dot{V} = \Delta\theta^T(t)K^{-1}\Delta\dot{\theta}(t) \tag{4.59}$$

$$= -\Delta\theta^T(t)w(t)e(t) \tag{4.60}$$

$$= -\Delta\theta^T(t)w(t)w^T(t)\Delta\theta(t) \tag{4.61}$$

$$\leq 0. \tag{4.62}$$

Thus $\dot{V}$ is negative semi-definite, and the error system (4.56) is globally stable. In addition, as in the 2-axis case, if $w(t)$ is PE [42, 52], the error system is globally asymptotically stable.

4.7.4 3-axis Adaptive Observer Simulation

The 3-axis observer is evaluated in two numerical simulations. The simulated magnetometer measurements include sensor noise of $\sigma_m = 0.002$ Gauss (G)

and sensor biases of

$$T = \begin{bmatrix} 1.10 & 0 & 0 \\ 0 & 0.95 & 0 \\ 0 & 0 & 1.1 \end{bmatrix}, \tag{4.63}$$

$$b = \begin{bmatrix} 0.06 & -0.07 & 0.03 \end{bmatrix}^T. \tag{4.64}$$

The observer's initial conditions were set to

$$\hat{\theta}(t_0) = \begin{bmatrix} 1 & 1 & 1 & 0 & 0 & 0 & 0 & 0 & 0 \end{bmatrix}^T / \phi \tag{4.65}$$

where

$$\phi = \|m_t\|^2 \tag{4.66}$$

$$= \| \begin{bmatrix} 0.20579 & -0.04065 & 0.46879 \end{bmatrix} \|^2 \, \mathrm{G}^2. \tag{4.67}$$

The gain matrix used was

$$K = diag([10\ 10\ 10\ 10\ 10\ 10\ 1\ 1\ 1]). \tag{4.68}$$

In **3Axis-Sim1**, the instrument experiences large changes in roll, pitch, and heading enabling full coverage of a sphere by the measure magnetic field vector. Figure 4.10 reports the true magnetic field, $m_t(t)$, from the simulation. Figures 4.11-4.12 report the parameter errors from **3Axis-Sim1**. The parameter errors are shown to converge to zero. Hence, when $w(t)$ is PE, the parameters converge to their true values.

In **3Axis-Sim2**, the instrument experiences smaller changes in roll and pitch than in **3Axis-Sim1**. Figure 4.13 reports the true magnetic field, $m_t(t)$.

Unlike in **3Axis-Sim1**, in **3Axis-Sim2**, the magnetometer experiences smaller rotations in roll and pitch. The limited motion of the instrument in **3Axis-Sim2** is shown in Figures 4.14-4.15 to not be enough for the convergence of the parameters to their true values. In **3Axis-Sim2**, the magnetic field vector does not cover enough of the sphere to allow accurate sensor bias estimation. Simulations have show that, the 3-axis adaptive observer requires roll and pitch magnitudes of $> 45^{\circ}$ in order fo the observer to converge to the true parameter values.

The 3-axis adaptive observer suffers from the same problem as using least-squares for doing magnetometer hard-iron and soft-iron calibration — they require large angular rotations and full coverage of the sphere in order for them to be used for accurate magnetometer sensor bias estimation. The 3-axis adaptive observer is not suitable for use in the many vehicles which are passively stable in roll and pitch and experience only limited motion in roll and pitch. This class of vehicles is unable to attain the roll and pitch angles required for the observer to accurately estimate the magnetometer soft-iron and hard-iron biases.

4.8 Conclusion

This chapter reports a novel adaptive observer for on-line, real-time estimation of hard-iron and soft-iron magnetometer biases in 2-axis magnetometers for use in AHRSs. AHRSs commonly use calibrated magnetometers as a measurement of the magnetic field direction for estimating heading. The accuracy of these systems rely on the calibrated magnetometer direction to be accurate,

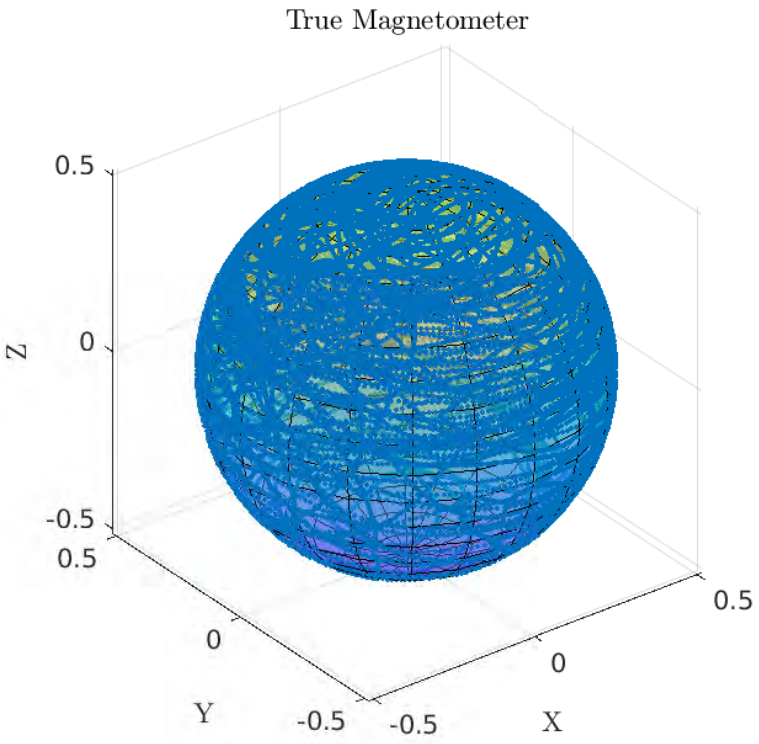

Figure 4.10: 3Axis-Sim1: True magnetic field vector, $m_t(t)$.

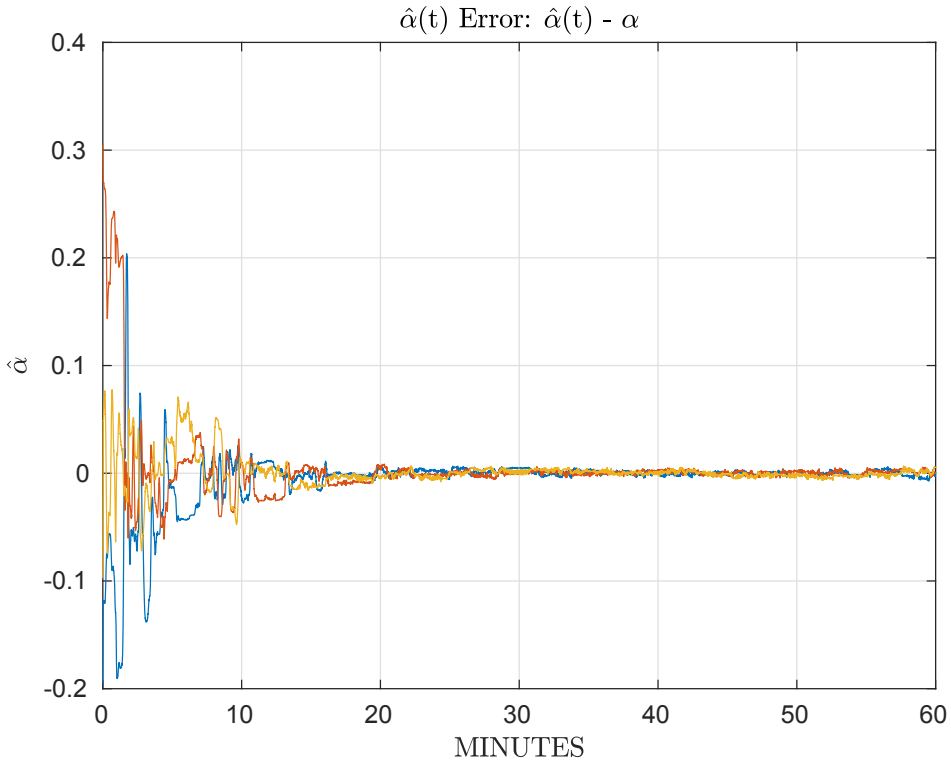

Figure 4.11: 3Axis-Sim1: Estimated $\hat{\alpha}(t)$ error.

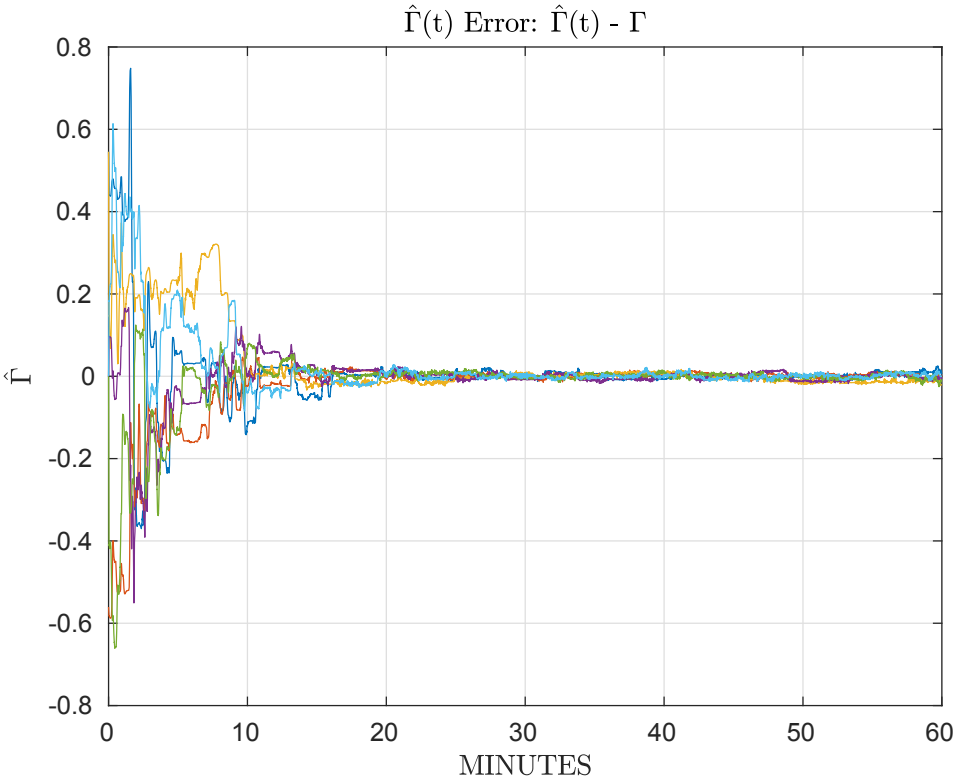

Figure 4.12: 3Axis-Sim1: Estimated $\hat{\gamma}(t)$ error.

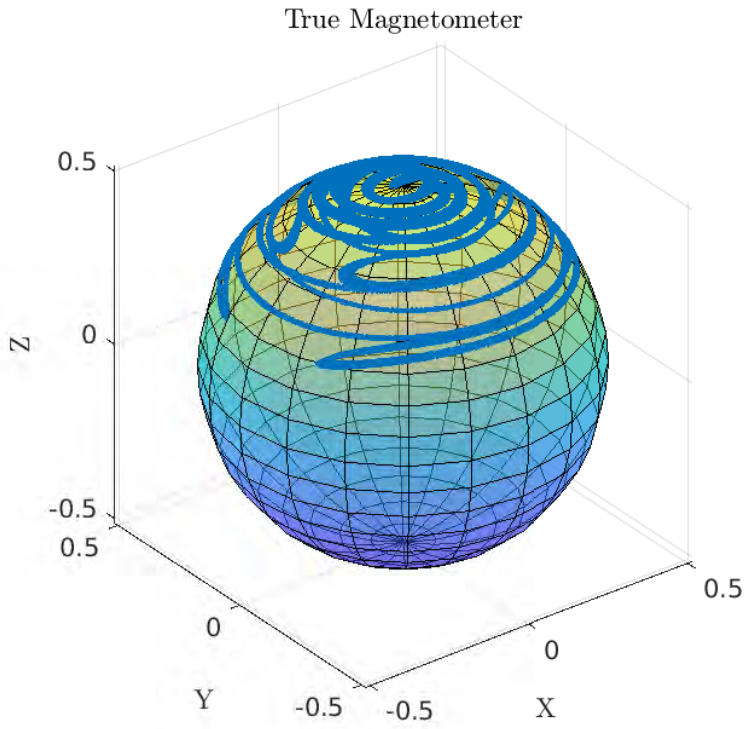

Figure 4.13: 3Axis-Sim2: True magnetic field vector, $m_t(t)$.

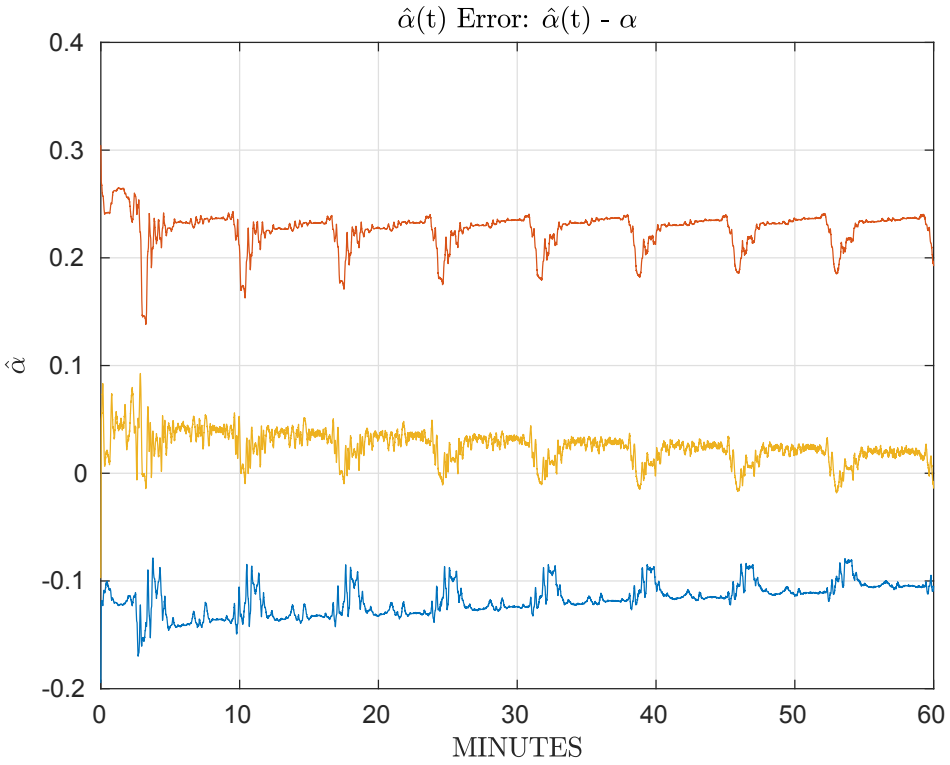

Figure 4.14: 3Axis-Sim2: Estimated $\hat{\alpha}(t)$ error.

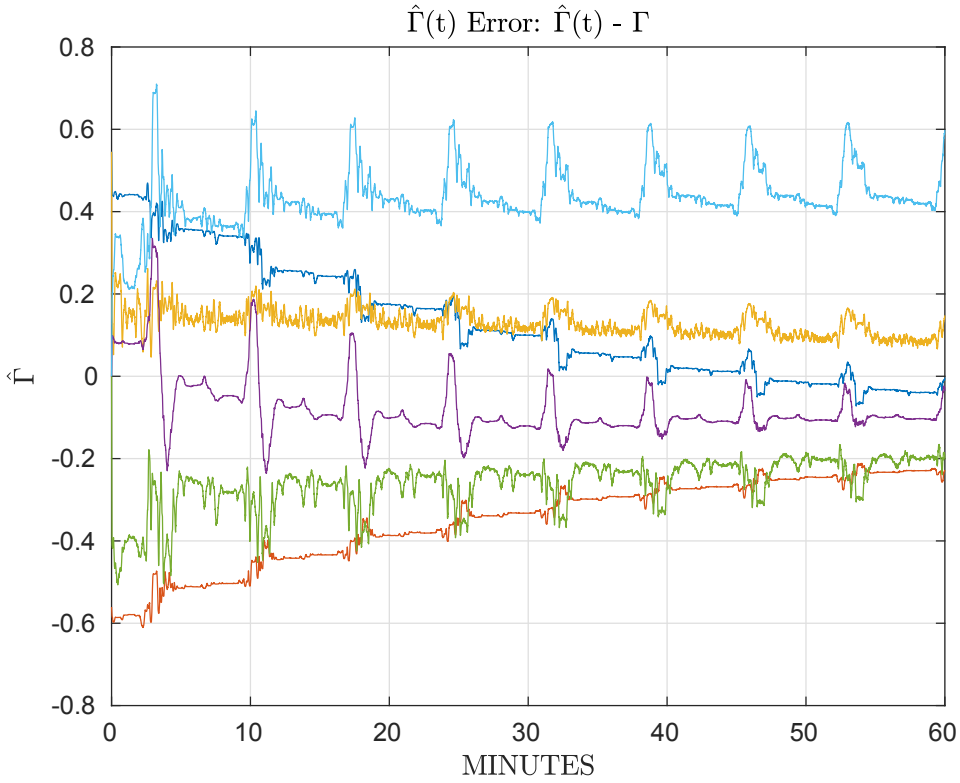

Figure 4.15: 3Axis-Sim2: Estimated $\hat{\gamma}(t)$ error.

but do not require the correct magnitude of the calibrated magnetometer. Estimating the magnetometer's soft-iron bias up to a scale factor preserves the calibrated magnetometer's direction. Hence, the proposed approach which observes a scaled version of T, can be utilized to bias-compensate magnetometers to provide accurate heading estimates.

The observer uses only magnetometer sensor signals, does not require knowledge of the instrument attitude, and is shown to be globally stable. When the measured magnetometer is PE, the observer is shown to be globally asymptotically stable where the estimated parameters converge to their true values. The simulation study and full-scale vehicle experiment suggest that the observer can be utilized to provide accurate magnetometer bias compensation for AHRS. The vehicle trial shows that the estimated parameters converge to a steady state and the calibrated magnetometer's corresponding heading estimate tracks ground truth heading to 1.9° RMSE which is the RMSE corresponding to the least squares calibration.

In addition to the 2-axis adaptive observer, a 3-axis extension of the observer is reported. The 3-axis observer however, is shown to suffer from the same drawbacks of most previously reported least-squares methods. Large angular rotations and full coverage of the sphere are required in order for the 3-axis observer to be used for accurate magnetometer sensor bias estimation. The 3-axis adaptive observer is not suitable for use in the class of vehicles which are passively stable in roll and pitch and the focus of this chapter. Chapter 5 addresses the problem of estimating the full 3-axis magnetometer soft-iron and hard-iron sensor biases in vehicles experiencing small roll and

pitch rotations.

In future studies, the authors hope to develop a coarse and fine alignment protocol to allow for fast convergence and accurate bias estimation and employ the observer in field trials.

Intended to be blank.

Chapter 5

Online Three-Axis Magnetometer Hard-Iron and Soft-Iron Bias and Angular Velocity Sensor Bias Estimation Using Angular Velocity Sensors for Improved Dynamic Heading Accuracy

5.1 Introduction

This chapter is based on the research originally reported in [63]. Abhimanyu Shah collaborated on this research and is a co-author of [63]. The dynamic instrumentation and estimation of vehicle attitude, especially geodetic heading, is critical to accurate navigation of land, sea, and air vehicles in dynamic motion. The utility of the ubiquitous 9-axis inertial measurement unit (IMU) (with 3-axis magnetometers, 3-axis angular rate sensors, and 3-axis accelerometers) for accurate heading estimation is commonly vitiated by very significant hard-iron and soft-iron magnetometer biases, as well as by angular-rate sensor

biases. Many previously reported bias estimation approaches are complicated by (i) the need to know the instrument's real-time attitude (heading, pitch, and roll), or (ii) the need for the instrument to experience very large attitude motion excursions (which may be infeasible for instruments mounted in many full-scale vehicles) like required by the TWOSTEP method [1, 2], many ellipsoid fitting methods, and the adaptive observer presented in Section 4.7.

This chapter reports a novel method for dynamic on-line estimation of hard-iron and soft-iron biases of 3-axis magnetometers under *dynamic* motion (rotation and translation) without any knowledge of the instrument's real-time attitude. Our approach is to formulate a nonlinear process dynamics model for the variation in the magnetic field vector over time as the instrument is subject to *a priori* unknown angular velocities. We report a 15-state bias estimator utilizing this process model that simultaneously estimates (i) a 3-axis dynamic process-model estimate of the true magnetic field vector, (ii) all 6 soft-iron bias magnetometer bias terms, (iii) all 3 hard-iron bias magnetometer bias terms, and (iv) all 3 angular velocity sensor bias terms. The proposed magnetometer and angular velocity bias estimator (MAVBE) is implemented as an extended Kalman filter (EKF) in which the difference between the estimated process model magnetometer measurement and the actual observed magnetometer measurement provide the EKF innovations. The 3-axis accelerometer signal is then utilized with the estimator signals to provide improved accuracy gyro-stabilized dynamic heading estimation. We report an observability analysis of the system. We report performance analysis and comparision to the widely cited magnetometer only TWOSTEP method [2] in a numerical simulation

study, in full-scale laboratory experimental trials with a 9-axis IMU on the Johns Hopkins University (JHU) remotely operated vehicle (ROV), Figure A.2, and in at-sea field experimental trials with a 9-axis IMU on the JHU Iver3 autonomous underwater vehicle (AUV) in the Chesapeake Bay, MD, USA, Figure A.3.

Advantages of the proposed MAVBE approach include the following: (i) knowledge of the instrument attitude is not required for sensor bias estimation, (ii) the system is shown to be observable, (iii) bias estimates converge rapidly to true bias parameters, (iv) only modest instrument excitation is required for bias estimate convergence, (v) magnetometer hard-iron and soft-iron bias compensation is shown to dramatically improve dynamic heading estimation accuracy.

5.1.1 Background and Motivation

Accurate sensing and estimation of attitude (i.e. geodetic heading, and roll and pitch referenced to the local gravitational field) are critical components of navigation systems for a wide variety of robotic vehicles. The need for accurate attitude estimation is particularly acute in the case of vehicles operating in GPS-denied environments such as underwater.

Over the past decade, the development of a new generation of small low-cost UVs has begun to enable oceanographic, environmental assessment, and national security missions that were previously considered impractical or infeasible (e.g. [8, 9, 47, 66, 80]). These small low-cost UVs commonly employ MEMS IMUs comprised of 3-axis MEMS magnetometers, angular rate sensors,

and accelerometers to estimate local magnetic heading, pitch, and roll, typically to within several degrees of accuracy, but require careful soft-iron and hard-iron calibration and compensation to achieve these accuracies. Moreover, magnetic attitude sensors must be recalibrated for soft-iron and hard-iron biases whenever the vehicle's physical configuration changes significantly (i.e. sensors or other payloads added or removed), as very commonly occurs on oceanographic marine vehicles. Studies have shown that the accuracy of magnetic heading sensors is often the principal error source in overall navigation solutions [30]. Thus it is essential to estimate accurately and compensate for attitude sensor biases in order to achieve high accuracy attitude estimation. However, common approaches for hard-iron and soft-iron bias calibration require significant angular motion of the instrument (which is impossible on many UVs and land vehicles). We show that the use of angular-rate signals in the proposed MAVBE method enables the calibration to be performed with smaller angular excursions of the instrument, thus enabling the calibration of land and underwater vehicle compasses.

5.1.2 Literature Review

A variety of methods for magnetometer bias estimation have been reported. Geophysics researchers commonly use batch methods for magnetometer calibration [6, 22]. Alonso and Shuster proposed the "TWOSTEP" method [1] for estimating magnetometer sensor bias, and an extended method for calculating magnetometer scale and orthogonality factors as well [2]. Vasconselos et al. report magnetometer bias estimation as an ellipsoid fitting problem which can

be solved with an iterative MLE approach [74]. Many least squares methods are reported for the ellipsoid fitting problem [3, 15, 16, 46] and Wu et al. [79] frame the ellipsoid fitting problem as a particle swarm optimization (PSO). Kok et al. [31] and Li and Li [33] fuse accelerometer measurements with magnetometer measurements to estimate magnetometer hard-iron sensor bias, and Papafotis and Sotiriadis [48] report an algorithm for three-axis accelerometer and magnetometer calibration using a gradient descent method. All of these methods, however, require large angular rotations of the instrument to achieve accurate bias estimation (which may be infeasible for instruments mounted in many full-scale vehicles) and, moreover, they are batch estimators that are not designed for on-line estimation of magnetometer sensor bias.

Sensor biases change over time due to changes in the configuration and payloads of the host vehicle, temperature, etc., which make it imperative to estimate sensor biases in real time. In [70], the authors report a novel method utilizing angular velocity measurements for estimating magnetometer hard-iron sensor biases, but the reported algorithm does not address soft-iron calibration and it assumes that the angular velocity sensor signal is already bias-compensated. In [61], the current author extended the work by [70] to include estimation of angular-rate gyroscope and accelerometer measurement biases, but this approach also does not address soft-iron magnetometer bias calibration.

Crassidis et al. report an extension to the TWOSTEP method based on the EKF [11] and Guo et al. report an alternative EKF approach for doing magnetometer sensor bias estimation [19]. However, these approaches require large

angular rotations of the instrument for accurate magnetometer calibration, similar to the batch methods mentioned above.

Soken and Sakai [56] report a magnetometer calibration method using the TRIAD algorithm and an UKF. However, this method requires knowledge of the initial attitude of the instrument and exhibits a lengthy convergence time.

Han et al. [21] report a gyroscope-aided EKF method for magnetic calibration. However, based upon our review of source code kindly provided by the original authors, this approach appears to integrate the angular rate forward in time which introduces random walk, thus it is not clear that it can be used continuously for a long period of time. In addition, their algorithm requires large angular rates for the hard iron bias to converge and appears to be unable to identify the hard or soft iron biases of high-end MEMS IMUs like the ones used in the current paper.

The present chapter reports a novel method for real-time estimation and compensation of 3-axis magnetometer soft-iron and hard-iron and angular rate sensor biases utilizing biased angular rate sensor measurements. The proposed MAVBE algorithm requires smaller angular motion compared to previously reported magnetometer bias estimation methods, does not require any knowledge of the instrument's attitude, can be implemented on-line in real-time, exhibits rapid estimate convergence, and requires only knowledge of the local magnetic field magnitude. If the local magnetic field magnitude is not known, the proposed method can still recover the direction of the magnetic field vector which is all that is needed for accurate navigation.

5.1.3 Chapter Outline

This chapter is organized as follows: Section 5.2 reports the exact deterministic process model, a discrete-time stochastic approximate process model, and an EKF formulation of the MAVBE. Section 5.3 discuses the evaluation of the MAVBE. Section 5.4 reports simulation evaluation of the proposed MAVBE approach for magnetometer and angular velocity sensor bias estimation, bias compensation, and heading estimation. Section 5.5 reports laboratory experimental evaluation of the MAVBE approach in full-scale UV laboratory experimental trials. Section 5.6 reports field experiments of the proposed MAVBE method in full-scale AUV field experiments in the Chesapeake Bay, MD, USA. Section 5.7 summarizes and concludes.

5.2 Magnetometer and Angular Velocity Bias Estimator (MAVBE) Formulation

This section reports the derivation of a novel online magnetometer and angular velocity bias estimator (MAVBE) for simultaneous hard-iron and soft-iron magnetometer and angular-rate sensor bias estimation and compensation. The biases are assumed to be very slowly time varying, and hence we model them as constant terms and update the estimates continuously.

5.2.1 Exact System Process Model

Magnetometers (including those employed in IMUs) are subject to two primary sensor calibration errors: hard-iron and soft-iron biases. Hard-iron

biases are constant magnetometer sensor bias terms due to the permanent magnetic signature of the instrument and the vehicle. Soft-iron biases are non-constant magnetometer sensor bias terms due to the magnetic permeability of the instrument and the vehicle, and will vary with vehicle heading and attitude. For most IMU magnetometers, hard-iron biases dominate soft-iron biases.

The most commonly utilized models for 3-axis magnetometer hard-iron and soft-iron bias, and for 3-axis angular velocity sensor bias are

$$m_m(t) = Tm_t(t) + m_b \tag{5.1}$$

$$w_m(t) = w_t(t) + w_b, \tag{5.2}$$

where $m_m(t) \in \mathbb{R}^3$ and $m_t(t) \in \mathbb{R}^3$ are the noise-free measured and true magnetometer values, respectively, in the instrument frame, $T \in \mathbb{R}^{3\times3}$ is a PDS matrix due to soft-iron effects, $m_b \in \mathbb{R}^3$ is the sensor bias due to hard-iron effects, $w_m(t) \in \mathbb{R}^3$ and $w_t(t) \in \mathbb{R}^3$ are the noise-free measured and true angular velocity signals, respectively, in the instrument frame, and $w_b \in \mathbb{R}^3$ is the angular velocity bias.

The PDS matrix T is parameterized as

$$T = \begin{bmatrix} a & b & c \\ b & d & e \\ c & e & f \end{bmatrix} \tag{5.3}$$

where we define $t_p \in \mathbb{R}^6$ as the vector of the 6 unique elements of T such that

$$t_p = \begin{bmatrix} a & b & c & d & e & f \end{bmatrix}^T. \tag{5.4}$$

Note that using this parameterization of T does not ensure that T is nonsingular. However in practice, we have observed T to be a diagonally dominant nonsingular matrix which results in our estimates of T to be far from singular. In order to ensure T to be nonsingular, one may try to estimate a triangular matrix corresponding to the Cholesky decomposition of T instead of T directly.

The true magnetometer value in the NED frame, ${}^{N}m_t \in \mathbb{R}^3$, is constant and is related to the true magnetometer value in the instrument frame by

$$ {}^{N}m_t = R(t)\ m_t(t), \tag{5.5} $$

where $R(t) \in SO(3)$ is the time varying rotation of the instrument frame with respect to the NED frame. Taking the time derivative of (5.5) yields

$$ 0 = \dot{R}(t)\ m_t(t) + R(t)\dot{m}_t(t). \tag{5.6} $$

Rearranging (5.6) yields

$$ \dot{m}_t(t) = -\mathcal{J}(w_t(t))m_t(t), \tag{5.7} $$

and substituting (5.2) yields

$$ \dot{m}_t(t) = -\mathcal{J}(w_m(t) - w_b)m_t(t). \tag{5.8} $$

Since the bias terms are assumed to be at most very slowly time varying, they are modeled as constants. Finally, the exact deterministic full state process

model can be written in state space form

$$\underbrace{\begin{bmatrix} \dot{m}_t(t) \\ \dot{m}_b \\ \dot{t}_p \\ \dot{w}_b \end{bmatrix}}_{} = \underbrace{\begin{bmatrix} -\mathcal{J}(w_m(t) - w_b)m_t(t) \\ \mathbb{O}_{3\times 1} \\ \mathbb{O}_{6\times 1} \\ \mathbb{O}_{3\times 1} \end{bmatrix}}_{} \tag{5.9}$$

$$\dot{\Phi}(t) \quad = \quad f\left(\Phi(t)\right), \tag{5.10}$$

with the measurement model as

$$\underbrace{\begin{bmatrix} m_m(t) \\ \|m_t(t)\|^2 \end{bmatrix}}_{} = \underbrace{\begin{bmatrix} T\, m_t(t) + m_b \\ m_t^T(t) m_t(t) \end{bmatrix}}_{} \tag{5.11}$$

$$z(t) \quad = \quad h(\Phi(t)) \tag{5.12}$$

where $\mathbb{O}_{m\times n}$ is a zero matrix of dimension $m \times n$, $\Phi(t) \in \mathbb{R}^{15}$ is the state vector, and $z(t) \in \mathbb{R}^4$ is the measurement. The w_b bias term is included in the state vector because we have a process model for it (bias is assumed to be constant), however the time-varying $w_m(t)$ term was excluded from the state since its process model is unknown. It is instead considered to be an exogenous input signal. Modeling $w_m(t)$ as a exogenous input is a common approach used in magnetometer calibration (e.g. [21, 56, 70]). Note that, unlike [70], herein we do not assume the angular velocity signal to be already bias-compensated.

As seen in (5.11), the measurement model requires knowledge of the magnitude of the local magnetic field vector which is available for most field vehicles via the WMM [43] or the IGRF model [68]. Note that if the local magnetic field vector magnitude is unknown, by setting $\|m_t(t)\|^2$ to a non-zero positive constant (e.g. Setting $\|m_t(t)\|^2 = 1$ will normalize the estimated

corrected magnetic field vector to 1.), the direction of the corrected magnetic field vector can still recovered, allowing accurate magnetic heading estimates.

5.2.2 MAVBE Process Model Linearization

The MAVBE EKF was implemented using a linear process model. The nonlinear dynamics given in (5.10) were linearized using an approach that follows closely from that used by Webster in [75]. The linearization of $f(\Phi)$ about an arbitrary operating point μ is given by

$$f(\Phi(t)) = f(\mu) + \mathbf{D}_{\Phi(t)}[\, f(\Phi(t))\,]_{\mu}(\Phi(t) - \mu) \; + H.O.T. \tag{5.13}$$

Neglecting the higher order terms ($H.O.T$), and rearranging yields

$$f(\Phi(t)) = \underbrace{\mathbf{D}_{\Phi(t)}[\, f(\Phi(t))\,]_{\mu}}_{A(\Phi(t))}\Phi(t) + \underbrace{f(\mu) - \mathbf{D}_{\Phi(t)}[\, f(\Phi(t))\,]_{\mu}\mu}_{u(\Phi(t))} \tag{5.14}$$

where $u(\Phi(t)) \in \mathbb{R}^{15}$ is referred to as the pseudo-control input and $A(\Phi(t)) \in \mathbb{R}^{15\times 15}$ is the Jacobian of $f(\Phi(t))$ with respect to $\Phi(t)$ evaluated at μ. Noting that $\Phi(t)$ is a function of time, the noise-free linearized process model is given by

$$\dot{\Phi} = A(\Phi(t))\Phi(t) + u(\Phi(t)) \tag{5.15}$$

$$z(t) = h\left(\Phi(t)\right) \tag{5.16}$$

where

$$A(\Phi(t)) = \mathbf{D}_{\Phi}[\, f(\Phi(t))\,]_{\mu} \tag{5.17}$$

$$= \begin{bmatrix} -\mathcal{J}(w_m(t) - w_b) & \mathbb{O}_{3\times 9} & -\mathcal{J}(m_t(t)) \\ \mathbb{O}_{12\times 3} & \mathbb{O}_{12\times 9} & \mathbb{O}_{12\times 3} \end{bmatrix}_{\mu}. \tag{5.18}$$

5.2.3 MAVBE Observability

The system (5.15)-(5.16) is observable on $[t_0, t_f]$ if and only if the observability Gramian

$$M(t_0, t_f) = \int_{t_0}^{t_f} \mathcal{H}^T(t, t_0) C^T(t) C(t) \mathcal{H}(t, t_0)\, dt \tag{5.19}$$

is full rank where $\mathcal{H}(t, t_0)$ is the state transition matrix [51] and $C(t)$ is the measurement Jacobian

$$C(t) = \mathbf{D}_{\Phi(t)}[\, h(\Phi(t))\,]_{\Phi(t)}. \tag{5.20}$$

It is unclear how to show analytically that a PE $w_m(t)$ signal results in a full-rank observability Gramian, and thus observability of the state vector. We were able to check numerically, however, that a variety of PE $w_m(t)$ signals result in a full-rank observability Gramian, and thus observability of the state vector.

5.2.4 MAVBE Process Model Discrete-Time Stochastic Approximation

Using the approach followed in [75], the noise-free continuous time system (5.15)-(5.16) can be approximated as the discrete-time stochastic system

$$\Phi_{k+1} = \bar{A}_k \Phi_k + \bar{B}_k u(\Phi_k) + w_k \tag{5.21}$$

$$z_k = h\left(\Phi_k\right) + v_k, \tag{5.22}$$

where $w_k \sim \mathcal{N}(0, Q)$ is the independent zero-mean Gaussian process noise and $v_k \sim \mathcal{N}(0, R)$ is the independent zero-mean Gaussian measurement noise. $\bar{A}_k$ is related to $A(t)$ at time $t = k$ by

$$\bar{A}_k = e^{A(\Phi_k)\tau} \tag{5.23}$$

where τ is the discretization time step. Similarly, $\bar{B}_k$ can be computed as

$$\begin{aligned} \bar{B}_k &= \int_0^\tau e^{A(\Phi_k)(\tau - s)}\, ds \\ &= e^{A(\Phi_k)\tau} \int_0^\tau e^{-A(\Phi_k)s} ds \\ &= \bar{A}_k \int_0^\tau e^{-A(\Phi_k)s} ds. \end{aligned} \tag{5.24}$$

5.2.5 MAVBE EKF For Magnetometer Bias Estimation

The process model used to predict the state is

$$\Phi'_k = \bar{A}_{k-1} \Phi_{k-1} + \bar{B}_{k-1} u_{k-1}, \tag{5.25}$$

and the predicted covariance matrix is

$$\Sigma'_k = \bar{A}_{k-1}\Sigma_{k-1}\bar{A}_{k-1}^T + Q, \tag{5.26}$$

where Q is the process noise covariance matrix (constant). The Kalman gain is given by

$$K_k = \Sigma'_k \bar{C}_k{}^T (\bar{C}_k \Sigma'_k \bar{C}_k{}^T + R)^{-1}, \tag{5.27}$$

where R is the measurement covariance matrix (constant), and

$$\bar{C}_k = \mathbf{D}_\Phi [\, h(\Phi_k) \,]_{\Phi'_k} \tag{5.28}$$

$$= \begin{bmatrix} T & \mathbb{I}_3 & \left(m_t^T(k) \otimes \mathbb{I}_3\right) D_{t_p}[T^s] \\ 2m_t^T(k) & \mathbb{O}_{1\times 3} & \mathbb{O}_{1\times 9} \end{bmatrix}_{\Phi'_k} \tag{5.29}$$

where $\mathbb{I}_n$ is the identity matrix of dimension $n \times n$. The updated state estimate is

$$\Phi_k = \Phi'_k + K_k(z_k - \bar{C}\Phi'_k). \tag{5.30}$$

The updated covariance estimate is

$$\Sigma_k = (\mathbb{I}_{15} - K_k\bar{C}_k)\Sigma'_k. \tag{5.31}$$

5.3 Magnetometer Bias and Angular Velocity Estimator (MAVBE) Performance Evaluation

The remainder of this chapter is concerned with evaluating the proposed MAVBE presented in Section 5.2 in comparison to previously reported approaches to magnetometer bias estimation. We report a comparative performance analysis of the proposed MAVBE to the widely cited batch-processing

TWOSTEP method reported by Alonso and Shuster [2]. The TWOSTEP algorithm is based on minimizing a negative-log-likelihood function which can have multiple minima and maxima. A centering procedure first step is used to provide a good initial estimate of the sensor bias, and then a second step iteratively solves for the local minimum. Note that Dinale provides an excellent overview of the TWOSTEP method, and that Appendix C.1 of [13] provides a reference Matlab implementation of the TWOSTEP method which proved to be very helpful when implementing the TWOSTEP comparison [13].

The performance of these approaches are evaluated in the following three ways:

1. First, in Section 5.4, we report the evaluation of these approaches in numerical simulations in which both the the true simulated bias values and the true simulated heading values are known exactly.

2. Second, in Section 5.5, we report the evaluation of these approaches in full-scale laboratory experimental trials with a laboratory testbed ROV in which the true sensor biases are unknown, and thus the accuracy of the estimated biases cannot be measured directly. Instead, the accuracy of the heading estimate is used as an error metric for sensor bias estimation. The heading estimate was computed using accelerometer and magnetometer signals from the MicroStrain 3DM-GX5-25 9-Axis IMU (LORD Sensing-MicroStrain, Williston, Vermont, USA) [39], together with the sensor bias estimates. In the laboratory experiments, the estimated heading was compared to the ground truth heading from a

high-end INS, the iXBlue PHINS III (iXBlue SAS, Cedex, France), with heading accuracy of 0.05° / cos(latitude). [24, 25].

3. Third, in Section 5.6, we report the evaluation of these approaches in full-scale sea-trials with the JHU Iver3 AUV, in which neither the true bias values nor the true heading is known. In the field experimental trials, vehicle XY navigation error is used as a proxy for the accuracy of the magnetometer calibration. The vehicle track is recalculated using Doppler dead reckoning for each magnetometer calibration method and compared to the GPS track of the vehicle. In addition to the TWOSTEP method, the proposed MAVBE is compared to L3 OceanServer's commercial solution for a calibrated magnetic compass using the OceanServer OS5000 magnetic compass [44].

5.3.1 Attitude Calculation

The vehicle coordinates are defined such that the x-axes is pointed forward on the vehicle, the y-axes is pointing starboard, and the z-axes down. Using this coordinate frame, the instantaneous estimated roll ϕ and pitch θ angles of the vehicle can be computed by [71]

$$\hat{\phi} = atan2\left(-a_y, -a_z\right), \tag{5.32}$$

$$\hat{\theta} = atan2\left(a_x, \sqrt{a_y^2 + a_z^2}\right), \tag{5.33}$$

where a_x, a_y, a_z are the x, y, z components, respectively, of the accelerometer signal. The calibrated magnetic field vector, $m(t)$, in the vehicle frame is

transformed to the local level frame by the relation ${}^{l}m = {}^{l}_{v}R(t)m(t)$ where ${}^{l}_{v}R(t) \in SO(3)$ is the rotation matrix using the roll and pitch estimates. Using the approach of [71], the instantaneous estimated heading can then be computed as

$$\hat{\gamma} = atan2\left(-{}^{l}m_y, {}^{l}m_x\right) - \gamma_0, \tag{5.34}$$

where γ_0 is the known local magnetic variation and where ${}^{l}m_x, {}^{l}m_y$ are the x, y components, respectively, of the ${}^{l}m$ signal.

5.3.2 Doppler Dead Reckoning Navigation

Doppler velocity logs (DVLs) are commonly used on UVs to measure vehicle three-axis velocity. When a DVL has bottom-lock, the instrument provides accurate measurements of the UV's three-axis velocity with respect to the fixed sea floor.

Using the roll, pitch, heading attitude of the vehicle, these velocity measurements can be transformed into world frame by [71]

$${}^{w}v(t) = {}^{w}_{v}R(t)\,{}^{v}_{i}R\,{}^{i}v(t) \tag{5.35}$$

where ${}^{v}_{i}R$ is the constant rotation matrix from the instrument coordinate frame to the vehicle coordinate frame, ${}^{w}_{v}R(t)$ is the time varying rotation matrix from the vehicle coordinate frame to the inertial world coordinate frame (the rotation matrix corresponding to the roll, pitch, heading of the vehicle), ${}^{i}v(t)$ is the vehicle's velocity in the DVL instrument's coordinate frame, and ${}^{w}v(t)$ is the world frame vehicle velocity. ${}^{w}v(t)$ can then be integrated to provide

the dead reckoning position estimate [76]

$$^{w}p(t) = {}^{w}p(t_0) + \int_{t_0}^{t} {}^{w}v(\tau)\, d\tau. \tag{5.36}$$

5.4 MAVBE Simulation Evaluation

5.4.1 Simulation Setup

The proposed bias estimation and compensation algorithm was evaluated in a numerical simulation using Matlab. Simulated IMU sensor measurements were generated by simulating sinusoidal vehicle motions. The simulated data was generated at 20 hz. Noise was added to this data with characteristics observed from experimental bench tests of a MicroStrain 3DM-GX5-25 [39]. The measured standard deviations of the simulated magnetometer and angular-rate sensors sampled at 20 hz and the simulated "true" sensor biases used during the simulated data generation, which are realistic sensor bias values for a MicroStrain 3DM-GX5-25 as observed from bench tests, are given in Table 5.1.

Table 5.1: Simulation Setup Parameters.

	Sensor Noise
σ_m	$[2\ 2\ 2]^T \cdot 10^{-4}$ G
σ_w	$[2.4\ 2.4\ 2.4]^T \cdot 10^{-4}$ rad/s
	Sensor Bias
m_b	$[0.6\ {-0.7}\ {-1}]^T \cdot 10^{-1}$ G
w_b	$[{-2}\ 3\ {-1}]^T \cdot 10^{-3}$ rad/s
t_p	$[1.1\ 0.1\ 0.03\ 0.95\ 0.01\ 1.2]^T$
	Sensor Bias Estimate Initial Values
$\hat{m}_b(t_0)$	$[0\ 0\ 0]^T$ G
$\hat{t}_p(t_0)$	$[1\ 0\ 0\ 1\ 0\ 1]^T$
$\hat{w}_b(t_0)$	$[0\ 0\ 0]^T$ rad/s

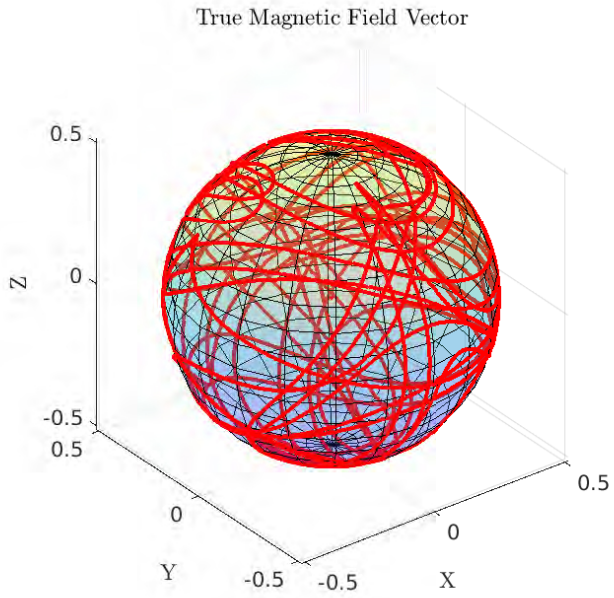

(a) **Sim1**: True magnetic field vector.

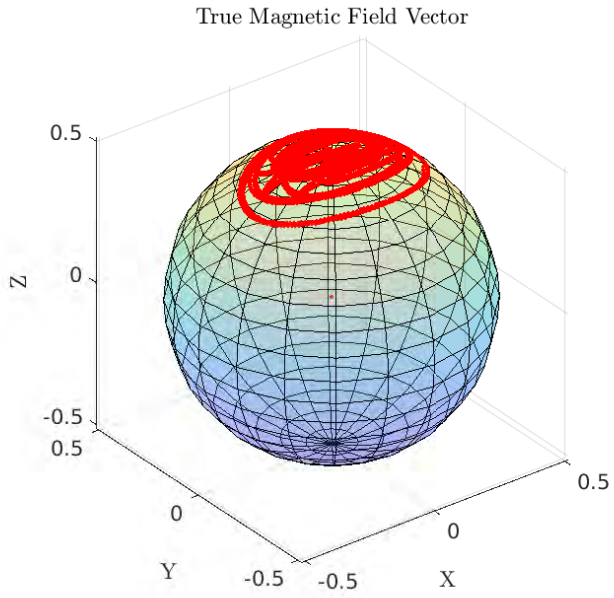

(b) **Sim2**: True magnetic field vector.

Figure 5.1: Simulation: The true magnetic field vectors in the instrument frame during the simulations.

The simulated instrument experienced smooth sinusoidal rotations. In **Sim1**, the instrument experiences changes in roll, pitch, and heading of $\pm 180^{\circ}$. However, in **Sim2** the instrument experiences smaller angular rotations with roll and pitch magnitudes of $< 50^{\circ}$ and heading of $\pm 180^{\circ}$. Figure 5.1 shows the true magnetic field in the instrument frame.

The MAVBE was executed at 10 hz, the initial conditions for the sensor biases estimates are given in Table 5.1, and the measurement covariance matrix, R, was populated with the square of the σ_m standard deviations along the diagonal entries such that

$$R = diag([4\ 4\ 4]) \cdot 10^{-8}, \tag{5.37}$$

and a process covariance matrix, Q, that works well is

$$Q = diag([1\ 1\ 1\ 1\ 1\ 1\ 1\ 1\ 1\ 1\ 1\ 1\ 0.01\ 0.01\ 0.01]) \cdot 10^{-10}. \tag{5.38}$$

Larger Q values resulted in quicker convergence, at the expense of more oscillatory final steady states, while lower Q values resulted in slower convergence, but a smoother final steady state. We selected Q empirically to provide a balance between convergence time and a smooth final steady state. In the future, two different process covariance matrices could be chosen for coarse and fine alignment in order to achieve fast convergence and a less oscillatory final steady state. Also, after an initial calibration, previous estimates for the sensor biases can be used as initial conditions to the MAVBE in order to greatly decrease convergence time of the proposed estimator.

Table 5.2: Table of estimated bias values for the two experiments.

	m_b (G)	t_p	w_b (°/s)
True	**[0.060 -0.070 -0.100]**	**[1.100 0.100 0.030 0.950 0.010 1.200]**	**[-0.002 0.003 -0.001]**
MAVBE Sim1	[0.059 -0.070 -0.100]	[1.099 0.100 0.030 0.949 0.010 1.200]	[-0.002 0.003 -0.001]
TWOSTEP Sim1	[0.064 -0.080 -0.084]	[1.100 0.100 0.030 0.950 0.010 1.200]	N/A
MAVBE Sim2	[0.060 -0.070 -0.096]	[1.100 0.100 0.030 0.950 0.010 1.192]	[-0.002 0.003 -0.001]
TWOSTEP Sim2	[0.062 -0.075 -0.123]	[1.148 0.104 0.031 0.992 0.009 1.317]	N/A

Table 5.3: Comparison of heading RMSEs between the calibration techniques.

Calibration Method	Sim1	Sim2
Uncalibrated	23.35°	19.21°
MAVBE	0.54°	0.58°
TWOSTEP	0.61°	1.42°

5.4.2 Simulation Results

The error in estimated sensor biases for the simulations are shown in Figures 5.2-5.3. The simulation results show that the MAVBE can accurately estimate the true values of m_b, t_p, and w_b. Since, in simulation, the true values of the biases are known, it is easy to verify that the biases estimates converge to the true bias values, and not to arbitrary incorrect values, which would generally be the case if $w_m(t)$ was not a PE signal.

Table 5.2 presents the biases estimated by the MAVBE and TWOSTEP methods during **Sim1** and **Sim2**. In addition, Table 5.3 lists the heading errors corresponding to using the biases from Table 5.2 for magnetometer calibration.

In **Sim1**, the resulting heading RMSE of the calibrated magnetometer from the MAVBE and TWOSTEP methods was similar at 0.54° and 0.61° RMSE respectively. In **Sim1**, the large angular rotations of the instrument provide rich magnetometer measurements, allowing both of the methods to find the true sensor biases. However, in **Sim2** the resulting heading RMSE of the calibrated magnetometer from the MAVBE and TWOSTEP methods differ.

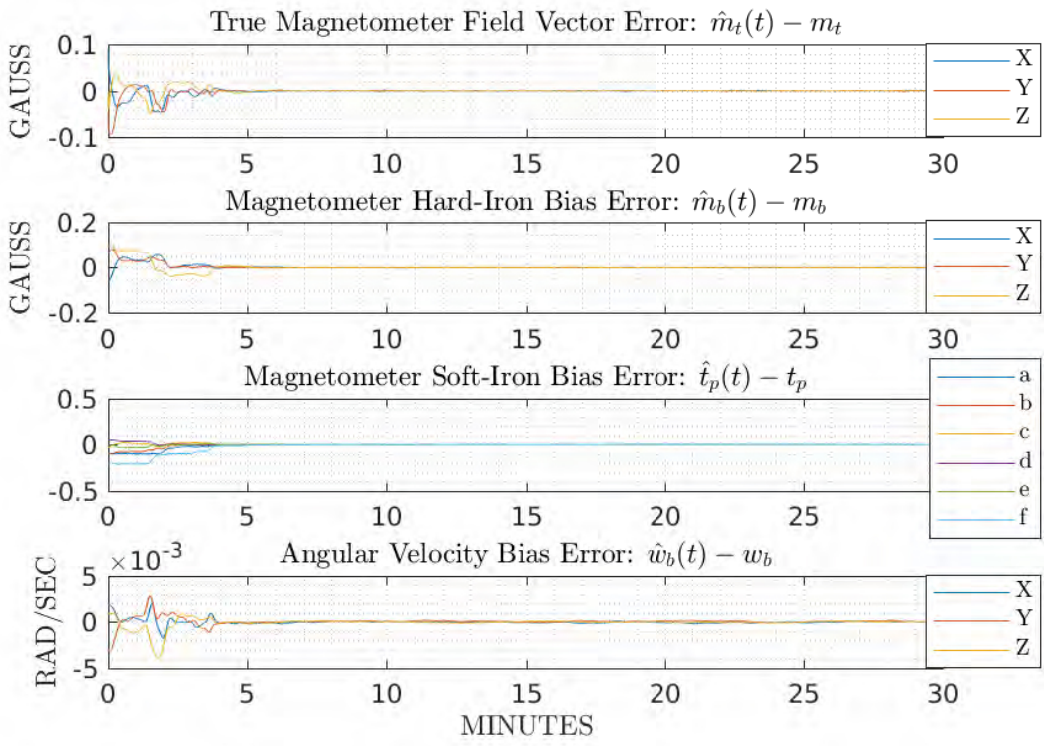

Figure 5.2: Simulation 1 Results. MAVBE magnetometer and angular rate sensor bias estimate errors converge to zero, i.e the estimated biases converge to their known true values.

The MAVBE method performs better, with a heading RMSE of 0.58°, than the TWOSTEP method with a heading RMSE of 1.42°. Since the magnetometer measurements in **Sim2** are less PE than in **Sim1** the use of the angular velocity measurements allows the MAVBE method to perform better than the magnetometer only TWOSTEP method.

Sim2 illustrates the main benefit of the proposed MAVBE. The modest attitude motion is sufficient for the MAVBE bias estimates to converge to their true values. However, in **Sim2**, the TWOSTEP method is unable to estimate all of the magnetometer bias terms accurately.

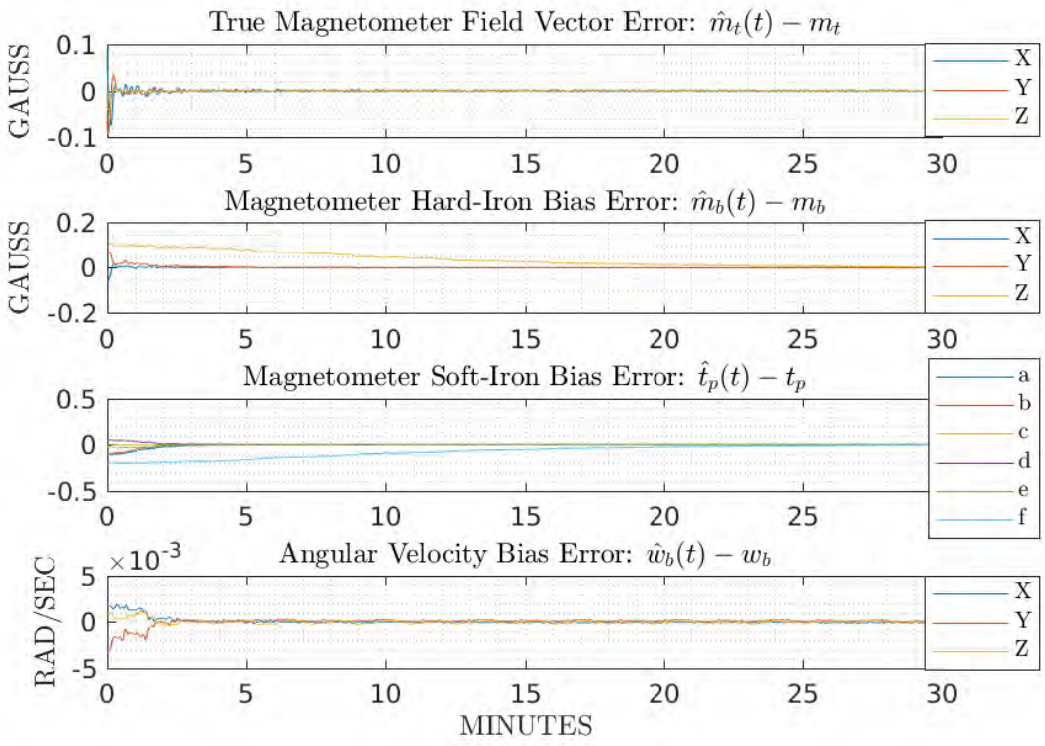

Figure 5.3: Simulation 2 Results. MAVBE magnetometer and angular rate sensor bias estimate errors converge to zero, i.e the estimated biases converge to their known true values.

The proposed MAVBE estimator's ability to converge to the proper biases while the instrument experiences modest changes in roll and pitch allows the method to be employed on most large full-scale ROVs, and some AUVs, which are typically very stable in roll and pitch, and hence, are unable to achieve larger roll and pitch changes required by many common methods like the TWOSTEP method for magnetometer calibration.

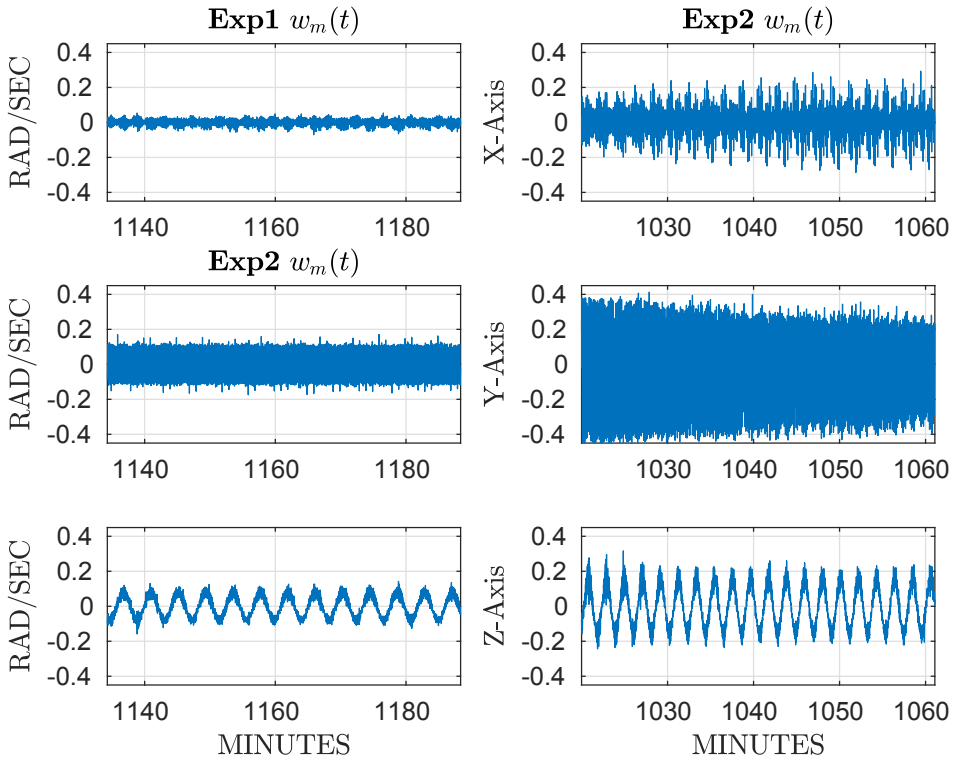

Figure 5.4: Laboratory Experiments: Exp1 and **Exp2** angular velocity measurements.

5.5 MAVBE Laboratory Experimental Evaluation

5.5.1 Experimental Test Facility

Experimental trials were performed with the JHU ROV, which is described in Appendix A.2 on page 189.

5.5.2 Experimental Setup

The JHU ROV was commanded to execute smooth sinusoidal rotations of roughly $\pm 180^\circ$ in heading and $\pm 15^\circ$ in pitch. Two experiments were conducted at different angular velocities. In experiment 1 (**Exp1**), the vehicle was

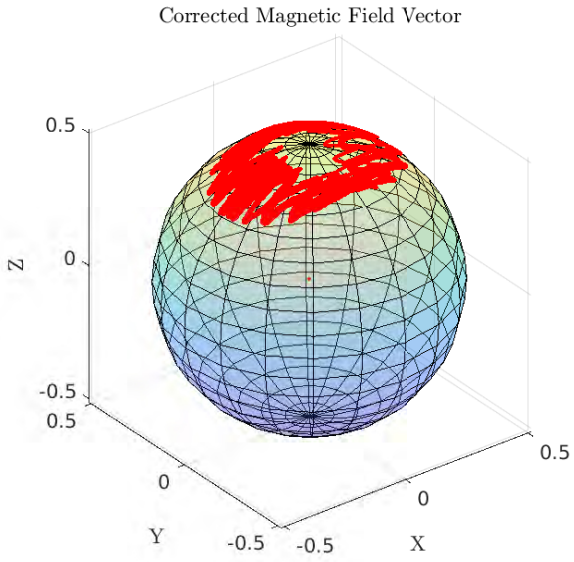

(a) **Exp1:** Corrected magnetic field vector

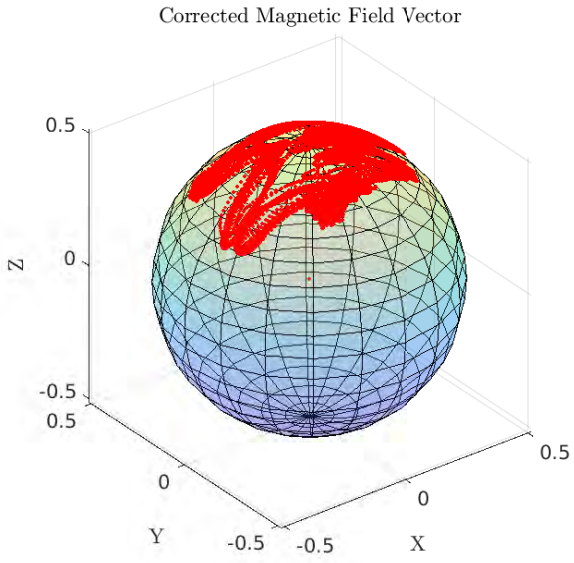

(b) **Exp2:** Corrected magnetic field vector

Figure 5.5: Laboratory Experiments: The corrected magnetic field vectors for **Exp1** and **Exp2**

.

Table 5.4: Table of estimated bias values for the two laboratory experiments.

	m_b (G)	t_p	w_b (°/s)
MAVBE Exp1	[0.053 0.006 0.171]	[0.662 0.005 0.028 0.634 0.009 0.974]	[0.0006 0.0019 0.0006]
TWOSTEP Exp1	[0.123 0.002 0.874]	[0.346 0.003 0.017 0.327 0.006 0.395]	N/A
MAVBE Exp2	[0.054 0.008 0.171]	[0.681 0.009 0.031 0.645 0.007 0.990]	[0.0002 0.0018 0.0005]
TWOSTEP Exp2	[0.106 0.024 0.070]	[0.629 0.010 0.012 0.600 -0.001 1.025]	N/A

Table 5.5: Comparison of heading RMSEs between different calibration techniques for the two laboratory experiments.

Calibration Method	Exp1	Exp2
Uncalibrated	23.34°	28.00°
MAVBE	0.75°	1.12°
TWOSTEP	2.88°	2.60°

subject to smaller angular velocities than in experiment 2 (**Exp2**). Figure 5.4 presents the measured angular velocities from the two laboratory experiments, and Figure 5.5 shows the corrected magnetic field vector during the **Exp1** and **Exp2** experiments. IMU data was logged at 20 hz using the MicroStrain 3DM-GX5-25. The initial conditions for the sensor bias estimates are the same as given in Table 5.1. The MAVBE was executed at 10 hz, and the process and measurement covariance matrices are given by (5.38) and (5.37), respectively.

5.5.3 Experimental Results

The sensor bias estimates for **Exp1** and **Exp2** are presented in Figures 5.6-5.7 and the final bias estimates in Table 5.4. The results show that the MAVBE sensor bias estimates converge to constant values. Since the true bias values are unknown, the final bias estimates were used for calibration of the magnetometer and angular rate sensors, enabling heading error to be used as an error metric. Table 5.5 reports the MAVBE's and TWOSTEP's calibrated magnetometer respective heading errors. In both laboratory experiments,

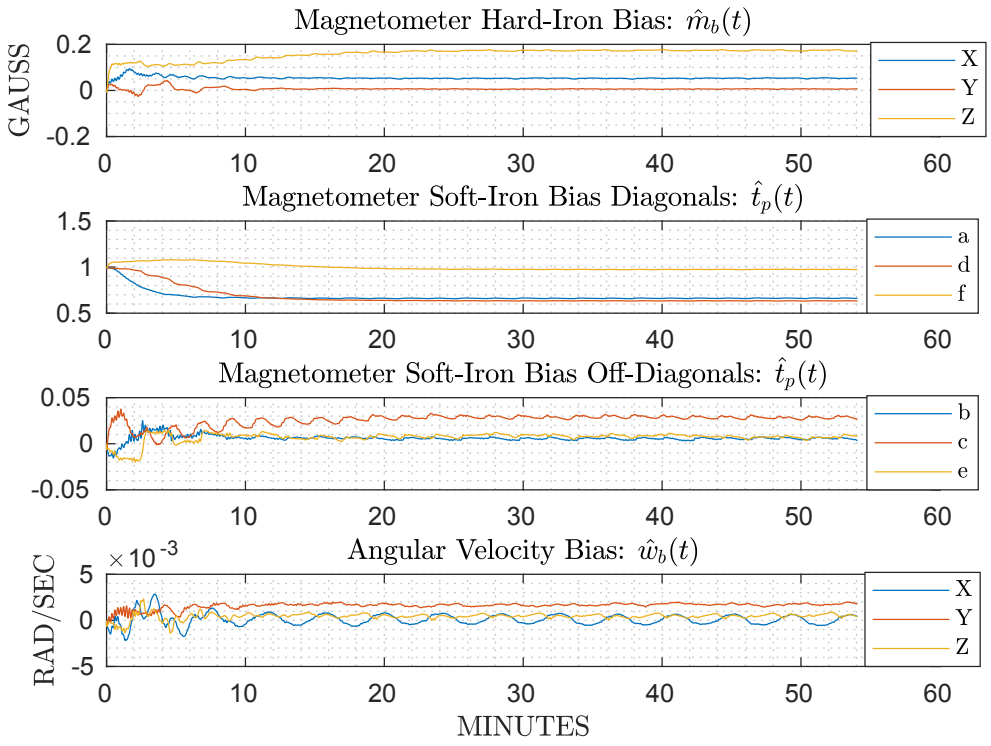

Figure 5.6: Experiment 1 (Exp1) Results: MAVBE magnetometer and angular rate sensor bias estimates converge to constant values.

the heading estimates corresponding to the MAVBE calibrated magnetometer closely tracks the ground truth value with a RMSE of roughly 1°. However, the TWOSTEP calibrated magnetometer leads to a worse RMSE of $> 2.5°$. The difference between the RMSE corresponding to the MAVBE and TWOSTEP calibration methods demonstrates the advantage of the MAVBE method for providing accurate magnetometer calibration on field vehicles which are unable to achieve the large roll and pitch changes required by many common methods like the TWOSTEP and ellipsoid fitting methods for magnetometer calibration.

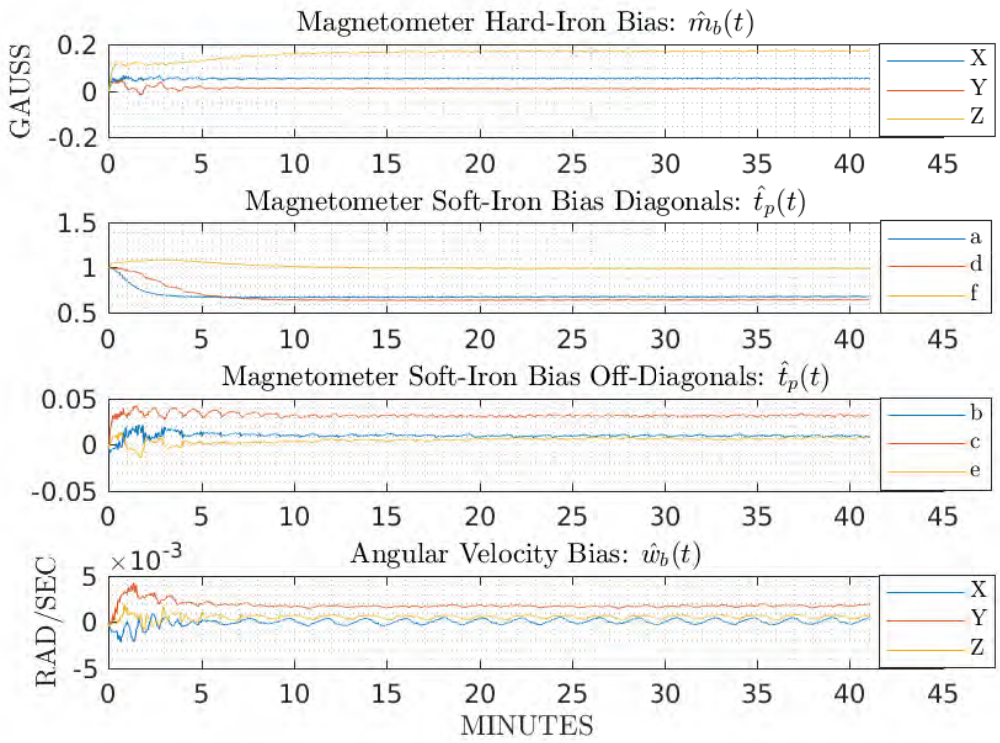

Figure 5.7: Experiment 2 (Exp2) Results: MAVBE Magnetometer and angular rate gyro bias estimates converge to constant values.

In addition, note that in Figures 5.6-5.7, the sensor bias estimates in **Exp2** converged faster than those in **Exp1**. This is due to the fact that the instrument in **Exp2** experienced higher angular velocities than in **Exp1** (seen in Figure 5.4). The increased excitement of the instrument in **Exp2** lead to a faster convergence time for the sensor bias estimates than those in **Exp1**.

5.6 MAVBE Field Trial Experimental Evaluation

5.6.1 Test Vehicle

Experimental fields trials were performed with the JHU's Iver3 AUV (L3 OceanServer, Fall River, MA, USA) [45] in the Chesapeake Bay, MD, USA. The JHU Iver3 AUV is described in Appendix A.3 on page 190.

5.6.2 Experimental Setup

The initial conditions for the sensor bias estimates are given in Table 5.1, the same as in the simulations.

The 3DM-GX5-25 IMU was sampled at 20 Hz. The MAVBE was executed at 10 hz, and the measurement covariance matrix, R, was populated with the square of the σ_m standard deviations along the diagonal entries such that R is (5.37), and the process covariance matrix, Q, is (5.38).

Before running the two field trials, a compass calibration for the Iver3's OS5000 magnetic compass [44] was completed per the instructions by L3 OceanServer [45]. Note that the JHU Iver3 AUV has its own L3 OceanServer proprietary magnetometer calibration method for the OS5000 magnetic compass based on heading sweeps and a look up table. This process is a two step process involving heading sweeps on a stand and an in-water compass calibration mission. During the field trials, the proposed MAVBE method is compared not only to the TWOSTEP method (as done in the simulation and laboratory experiments), but also to OceanServer's OS5000 commercial magnetic compass.

Table 5.6: Table of estimated bias values for the two field experiments.

	m_b (G)	t_p	w_b (°/s)
MAVBE Dive1	[-0.084 0.149 0.0146]	[0.986 0.002 -0.001 0.972 -0.002 0.955]	[0.0011 -0.0009 0.0005]
TWOSTEP Dive1	[-0.085 0.1468 -0.005] + [0.074 0.078 1.088]i	[-0.009 -0.006 -0.067 -0.006 -0.071 -0.990] + [0.003 0.003 0.037 0.003 0.039 0.539]i	N/A
MAVBE Dive2	[-0.084 0.149 0.020]	[0.970 0.002 -0.002 0.966 -0.003 0.947]	[0.0012 -0.0008 0.006]
TWOSTEP Dive2	[0.080 0.022 0.009] + [-0.057 -0.029 0.560]i	[-0.329 -0.017 0.067 -0.357 0.032 -0.992] + [0.008 0.004 -0.077 0.002 -0.040 0.754]i	N/A

Two field trials were conducted in Round Bay on the Chesapeake Bay, MD, USA. The JHU Iver3 AUV conducted two surface missions following cardinal and intercardinal heading directions. The trials were designed so that the JHU Iver3 AUV would follow track-lines along cardinal and intercardinal heading directions in order to ensure that the magnetometer is fully calibrated for all heading directions. The trials were conducted on the water surface to allow for GPS to be used as a navigation ground truth and in shallow water to allow for DVL bottom-lock velocity measurements. Two trials were conducted $\sim$ 4.5 hours apart (one in the morning and one in the afternoon) in order to confirm our assumption that the sensor biases were in fact slowly time varying and did not change drastically between experiments. Since the JHU Iver3 does not have a high-end INS (like used on the JHU ROV in the laboratory experiments) to compare heading estimates, XY navigation error is used as a proxy for the magnetometer calibration during the field trials. The recalculated dead reckoning navigation for each magnetometer calibration method is compared to the GPS track of the vehicle.

5.6.3 Experimental Results

The MAVBE's sensor bias estimates for **Dive1** and **Dive2** are presented in Figures 5.9 - 5.10 and Table 5.6. The results show that the MAVBE's sensor

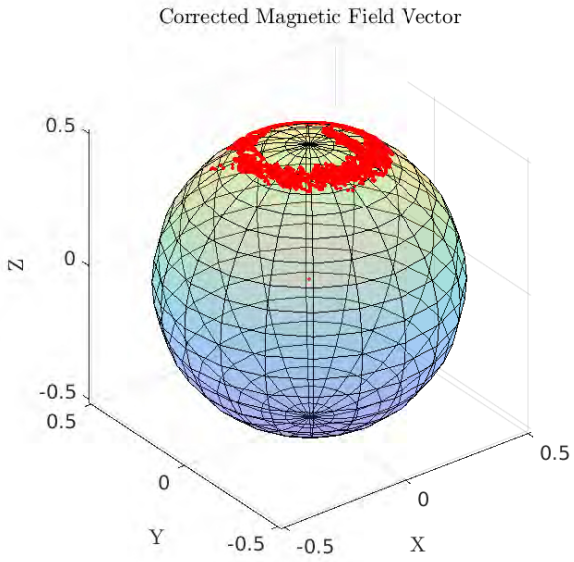

(a) **Dive1:** Corrected magnetic field vector.

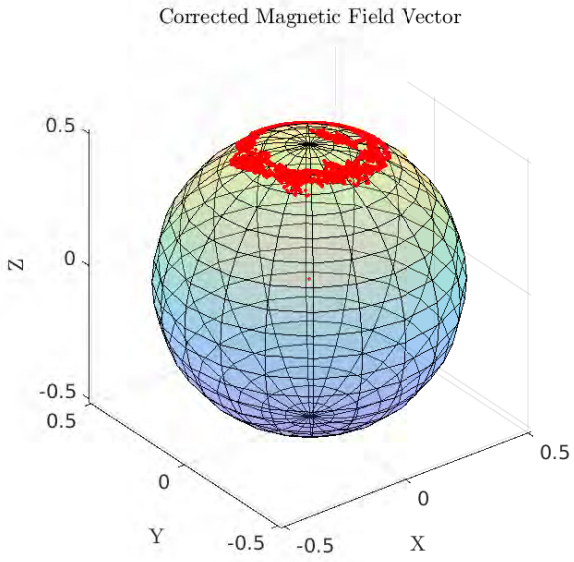

(b) **Dive2:** Corrected magnetic field vector.

Figure 5.8: Field Trials: The corrected magnetic field vectors for **Dive1** and **Dive2**

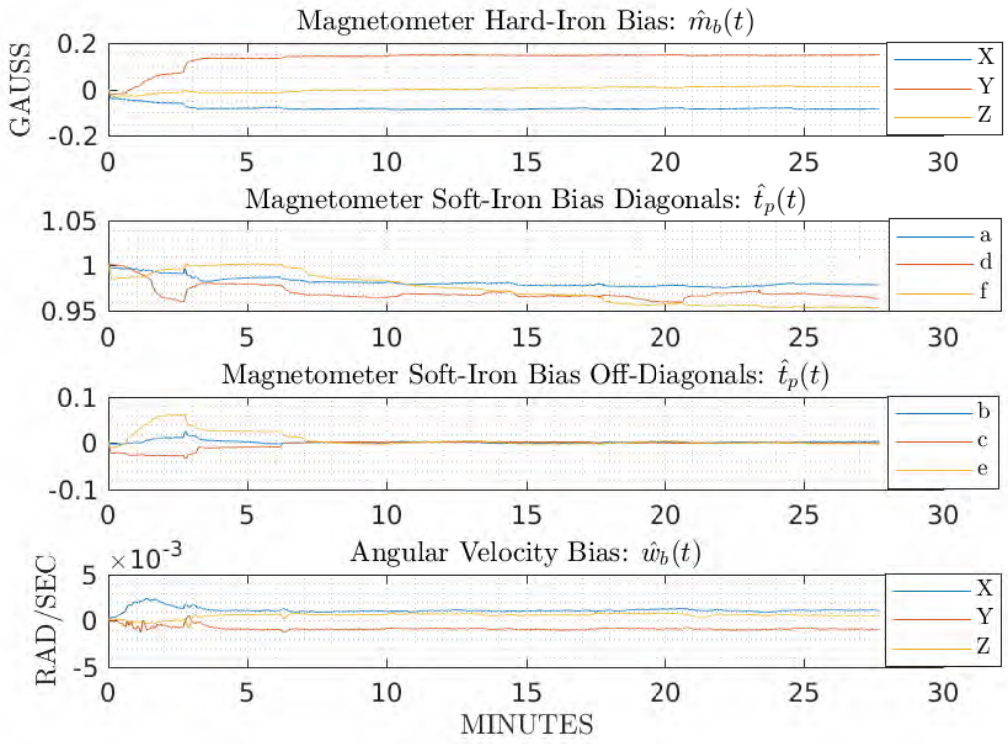

Figure 5.9: Dive 1 (Dive1) Results: MAVBE magnetometer and angular rate sensor bias estimates converge to constant values.

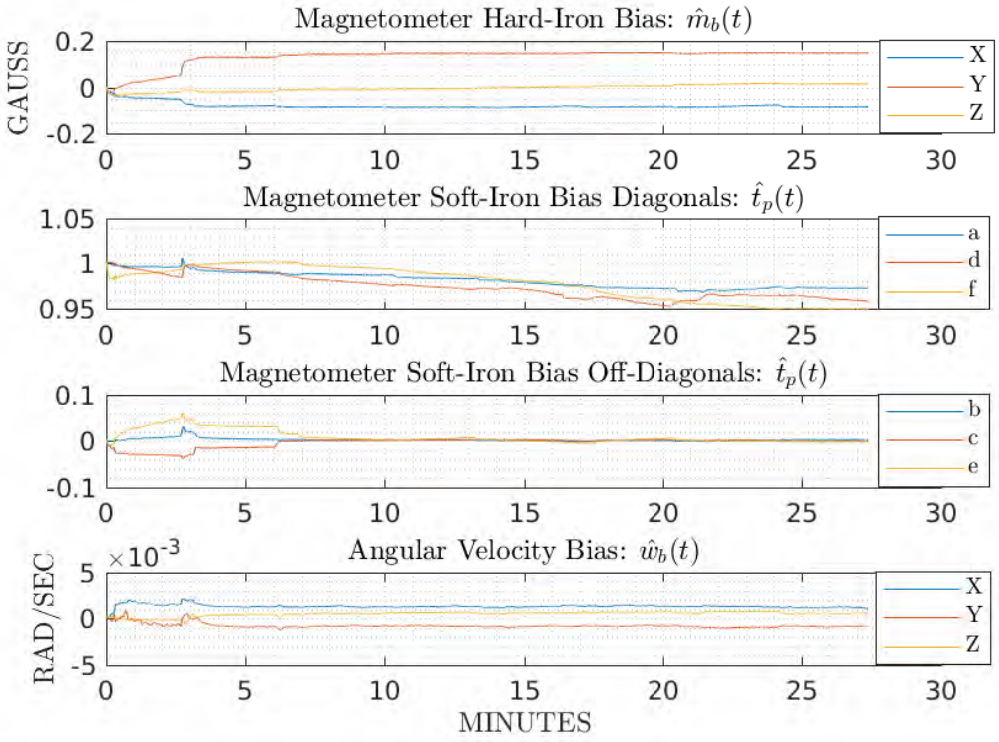

Figure 5.10: Dive 2 (Dive2) Results: MAVBE magnetometer and angular rate sensor bias estimates converge to constant values.

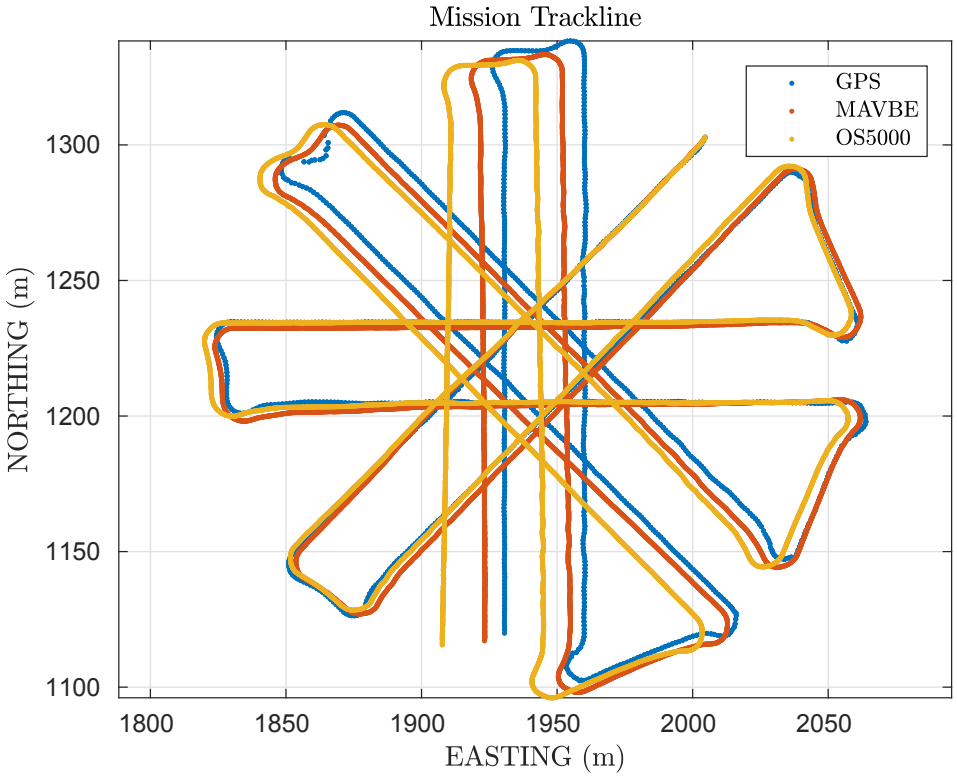

Figure 5.11: Dive 1 (Dive1) Navigation Tracks: Comparison of the Doppler dead reckoning navigation between the tracks from MAVBE compass calibration, the OS5000 calibrated compass, and the GPS ground truth track.

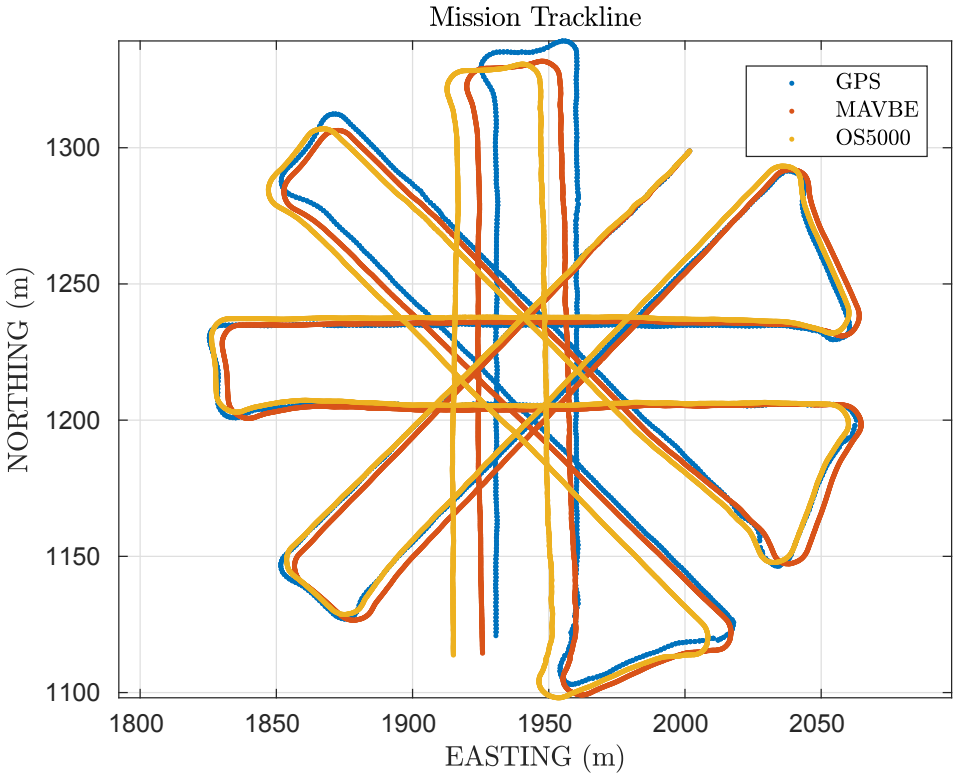

Figure 5.12: Dive 2 (Dive2) Navigation Tracks: Comparison of the Doppler dead reckoning navigation between the tracks from MAVBE compass calibration, the OS5000 calibrated compass, and the GPS ground truth track.

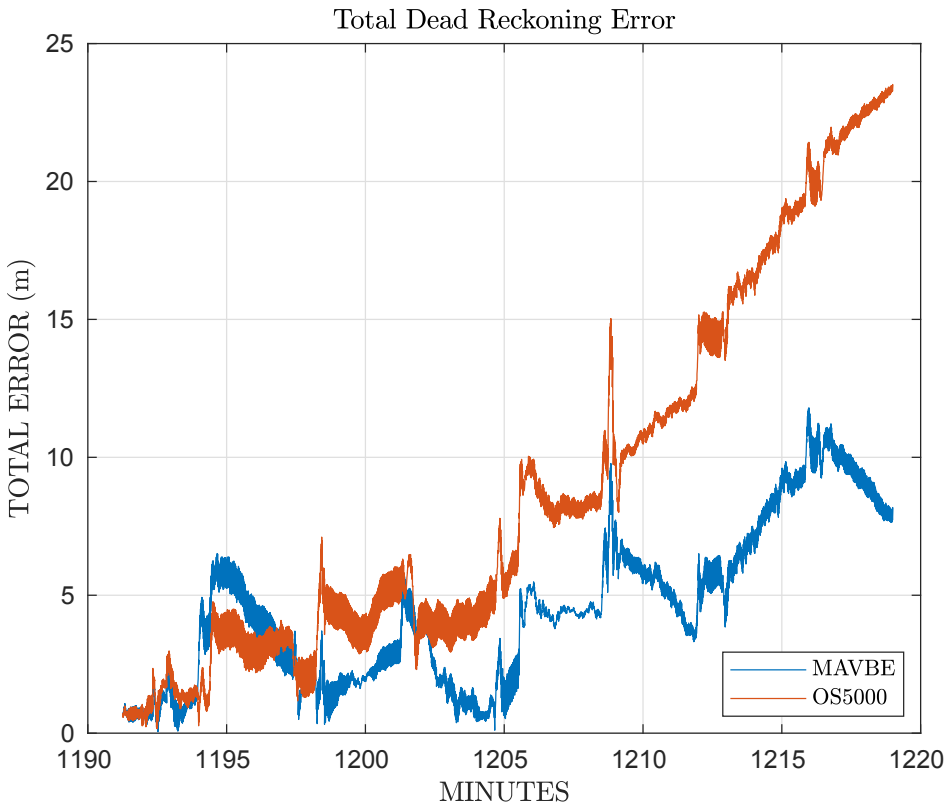

Figure 5.13: Dive 1 (Dive1) Navigation Error: Comparison of the Doppler dead reckoning navigation error of the tracks from MAVBE compass calibration and the OS5000 calibrated compass.

Figure 5.14: Dive 2 (Dive2) Navigation Error: Comparison of the Doppler dead reckoning navigation error of the tracks from MAVBE compass calibration and the OS5000 calibrated compass.

bias estimates converge to constant values. The final bias estimates were used for calibration of the magnetometer and angular rate sensor. Table 5.6 reports the final estimated sensor biases from **Dive1** and **Dive2** used for calibration. Figure 5.8 shows the corrected magnetic field vectors from the two field experiments. From Figure 5.8, it is evident that the Iver3 AUV experienced very little excitement in roll and pitch, and hence there is not great coverage of the sphere. As discussed earlier, common methods for magnetometer calibration like the TWOSTEP and ellipsoid fitting methods require sufficient excitement of the magnetometer for their convergence to the correct sensor bias estimates. During the two field experiments however, the AUV was stable in roll and pitch, and the TWOSTEP method was unable to accurately estimate the sensor bias. Table 5.6 reports the TWOSTEP estimated biases, which are clearly incorrect as they are found to be imaginary.

As reported in Table 5.6, the TWOSTEP algorithm failed to produce realistic bias estimates for either **Dive1** or **Dive2**. For these dives, the TWOSTEP method produced (physically meaningless) imaginary values for the magnetometer hard-iron and soft-iron estimates. Hence, the proposed MAVBE calibration is compared to the Iver3 AUV's calibrated OS5000 compass which relies on L3 OceanServers proprietary magnetometer calibration method based on heading sweeps and a look up table. In addition, since the Iver3 AUV does not have a high end INS to provide heading as a comparison to the calibrated magnetometer heading, Doppler navigation error is used as an error metric.

Figures 5.11-5.12 show the MAVBE and OS5000 calibrated magnetic compass navigation tracks in comparison with the GPS ground truth track, and

Figures 5.13-5.14 show the the respective two norm error of the navigation tracks. From Figures 5.13-5.14, we see that the MAVBE calibrated compass leads to more accurate Doppler dead reckoning navigation than the industry standard provided by L3 OceanServer's calibrated OS5000 magnetic compass. The navigation track error for the **Dive1** and **Dive2** field experiments demonstrate that the MAVBE calibrated MicroStrain 3DM-GX5-25 provides improved performance over the calibrated OS5000 compass. In addition, the field experiments demonstrate the ability of the MAVBE method to properly calibrate magnetometers on robotic vehicles which are stable in roll and pitch. This is in contrast to the TWOSTEP method which is unable to estimate the magnetometer hard-iron and soft-iron sensor bias during the field trials.

5.7 Conclusion

This chapter reports a novel method for online, real-time estimation of hard-iron and soft-iron magnetometer biases and angular rate sensor biases in inertial measurement units (IMUs) for use in AHRSs. AHRSs commonly use bias-compensated magnetometer measurements to estimate heading. By utilizing angular rate sensor measurements, smaller angular rotations of the instrument (in comparison to previously reported methods for magnetometer calibration) are required for accurate compensation of magnetometer and angular velocity sensor biases. Since the proposed estimator works with smaller changes in roll and pitch than previously reported methods, it can be implemented on real full-scale ROVs to provide online estimates of magnetometer sensor biases to allow real-time bias-compensation for these sensors.

Oceanographic underwater vehicles (UVs) and surface vehicles, which are commonly passively stable in roll and pitch, are unable to achieve the roll and pitch required for the common magnetometer calibration methods like the TWOSTEP and ellipsoid fitting methods. The simulations, laboratory experiments, and field trials show that the proposed MAVBE magnetometer calibration method provides improved performance over common methods like the TWOSTEP method and the OceanServer Iver3 AUV commercial solution. The TWOSTEP method was unable to estimate the magnetometer sensor biases during the field experiments due to the limited motion in roll and pitch. The ability of the proposed MAVBE method to accurately estimate magnetometer biases when there is limited excitation of the magnetometer signal illustrates the advantage of the proposed calibration method over common calibration methods like the TWOSTEP and ellipsoid fitting methods which fail when there is low coverage of the magnetometer on the sphere.

As demonstrated in the field experiments, the proposed method leads to improved position estimation of the Iver3 AUV over the TWOSTEP calibrated magnetometer and the calibrated OceanServer OS5000 magnetic compass.

In future studies, the authors hope to improve the convergence time of the estimator by developing coarse and fine alignment protocols. Different values for the process covariance matrix, Q, could be chosen during the coarse and fine alignment to enable both a fast convergence of the sensor biases and a smooth final steady state.

Chapter 6

Adaptive Bias and Attitude Observer on the Special Orthogonal Group for True-North Gyrocompass Systems

6.1 Introduction

This chapter is based on the research reported in [65]. This chapter reports two novel algorithms – one for real-time adaptive bias estimation of a *dynamic* (rotating) IMU *without* use of magnetometers or *a priori* knowledge of the instrument's attitude and one for estimating attitude directly on $SO(3)$ without linearization or an EKF. Preliminary simulation and experimental results of the reported true-North gyrocompass system employing a low-cost FOG IMU are reported.

Previous papers [58, 59, 60, 64] report earlier versions of this algorithm. The current chapter differs from this previous work [58, 59, 60, 64] by presenting a new formulation of the sensor bias estimation which relies on fewer

assumptions, generalizing the attitude algorithm to be used with general field vector measurements, presenting asymptotic stability proofs for the proposed observers, and providing an approach for choosing observer gains.

6.1.1 Background and Motivation

Accurate sensing and estimation of true-North geodetic heading and local level (roll and pitch) referenced to the local gravitational field (which we will refer to as true-North attitude) are critical components of high-accuracy navigation systems for a wide variety of robotic vehicles. The need for accurate true-North attitude estimation is particularly acute in the case of vehicles operating in GPS-denied environments (such as underwater) and in magnetically compromised environments (such as near ferromagnetic structures, buildings, or natural local magnetic anomalies). Smaller and lower-cost vehicles represent an additional challenge due to their limited sensor budget, small physical size, and limited energy storage capacity.

Over the past decade the development of a new generation of small low-cost UVs has begun to enable oceanographic, environmental assessment, and national security missions that were previously considered impractical or infeasible (e.g. [8, 9, 47, 66, 80]). This new generation of UVs often employ low-cost navigation systems that presently limit them to missions requiring only low-precision navigation of $\mathcal{O}$(1-100)m accuracy when submerged. High-end navigation approaches, of $\mathcal{O}$(0.1-10)m accuracy, traditionally require a Doppler sonar, costing \$20k-\$50k USD, and a North-seeking gyrocompass or INS, costing \$50k-\$250k. These high-end navigation approaches are largely

incompatible with low-cost AUVs with target total vehicle cost of $50k-$250k. Moreover, the high cost, large size, and high power-consumption of commercially available optical true-North seeking gyrocompasses is a principal barrier to the widespread use of high accuracy navigation for smaller and lower-cost UVs.

Most small low-cost UVs typically employ MEMS IMUs comprised of 3-axis MEMS magnetometers, gyros, and accelerometers to estimate local magnetic heading, pitch, and roll, typically to within several degrees of accuracy, but require careful soft-iron and hard-iron calibration and compensation to achieve these accuracies. Moreover, magnetic attitude sensors must be recalibrated for soft-iron and hard-iron errors whenever the vehicle's physical configuration changes significantly (i.e. sensors or other payloads added or removed, etc.), as very frequently occurs on oceanographic marine vehicles. Studies have shown that the accuracy of these magnetic heading sensors can be a principal error source in overall navigation solutions [30].

Recently, a new class of lower-cost (∼$20k USD), compact, and lower power FOG IMUs have become available — for example the commercial-off-the-shelf (COTS) KVH 1775 FOG IMU (KVH Industries, Inc., Middletown, RI, USA) – that provide sensor accuracies sufficient for estimation of true-North heading, pitch, and roll. This is in contrast to MEMS IMUs, which employ MEMS gyros that lack the sensitivity necessary to detect Earth-rate, and hence true-North heading, and thus rely on MEMS magnetometers to sense magnetic heading.

6.1.2 True-North Versus Magnetic Heading

True-North heading estimation differs from that of magnetic heading in that true-North is the direction towards the Earth's axis of rotation at the North Pole, while magnetic heading measures the direction of the horizontal component of the Earth's local magnetic field, which differs dramatically from true-North, often by many 10's of degrees – a difference termed *local magnetic variation*. The angular rate sensors (includes all MEMS IMUs) used in magnetic-North attitude sensors typically lack the sensitivity (the magnitude of Earth rate is orders of magnitude smaller than the magnitude of MEMS angular rate gyro sensor noise) to detect the angular rate of Earth ($15^\circ/\text{hr}$) and are commonly modeled as

$$w_m(t) = \cancelto{0}{w_E(t)} + w_v(t) + w_b + \eta(t) \tag{6.1}$$

where $w_m(t) \in \mathbb{R}^3$ is the measured angular rate vector in instrument coordinates, $w_E(t) \in \mathbb{R}^3$ is the angular rate of the Earth ($15^\circ/\text{hr}$), $w_v(t) \in \mathbb{R}^3$ is the angular rate of the instrument with respect to the local North-East-Down (NED) frame, $w_b \in \mathbb{R}^3$ is a constant measurement bias, and $\eta(t) \in \mathbb{R}^3$ is zero-mean Gaussian measurement noise. In contrast, true-North gyrocompass systems use high-end angular rate sensors, such as three-axes FOGs or RLGs, which are sensitive enough ($\|w_E(t)\| \gtrsim \|\eta(t)\|$) to measure Earth's angular rate and are typically modeled as

$$w_m(t) = w_E(t) + w_v(t) + w_b + \eta(t) \tag{6.2}$$

	IMU Grade	Accel. Sensor Type	Accel. Bias	Ang. Rate Sensor Type	Ang. Drift	Size, Weight, Power	Cost
(A)	High-End FOG/RLG	Mass	$\sim 1 - 10\mu$G	Optical	$< 1°/h$	5250 cm^3 4.5kg 14W	~$135K
(B)	Low-Cost FOG	MEMS	$\sim$ 1mG	Optical	$< 1°/h$	650 cm^3 0.7kg <5W	~$19K
(C)	MEMS	MEMS	~1 mG	MEMS	$> 10°/h$	12 cm^3 18g 0.4W	~$2K

Table 6.1: Comparison of (A) Conventional Navigation-Grade FOG/RLG IMUs, (B) Low-Cost FOG IMUs, and (C) MEMS IMUs Specifications. (A-B) are two classes of IMUs suitable for true-North gyrocompasses, and (C) are MEMS IMUs which do not have angular rate gyros sensitive enough to be used for true-North gyrocompass systems.

where the terms are the same as in (6.1). Table 6.1 compares these different classes of IMUs.

By fusing gyroscope and accelerometer measurements, true-North gyrocompass systems generate an estimate for the $w_E(t)$ component of the measured angular rate $w_m(t)$. Since the Earth's angular rate, $w_E(t)$, lies in the local North-down plane, the estimated angular-rate of Earth ($w_E(t)$) and the estimated gravity vector can be fused to estimate the true-North direction, roll, and pitch. We define the local North-down plane to be the plane that intersects the origin of the NED frame (defined in Section 2.1) and spans the North and down directions.

6.1.3 Chapter Organization

This chapter is organized as follows: Section 6.2 provides a literature review of attitude and sensor bias estimation. Section 6.3 presents the IMU sensor measurement model. Section 6.4 reports the sensor bias and East vector observer and stability proof. Section 6.5 numerically evaluates the observability gramian of the three simulations in order to analytically show asymptotic

stability of the observer present in 6.4. Section 6.6 presents the attitude observer and stability proof. Section 6.7 introduces the Gyrocompass system. Section 6.8 presents preliminary numerical simulations and experimental results. Section 6.9 summarizes and concludes.

6.2 Literature Review

Because field sensors, such as angular rate gyros and accelerometers, have significant sensor bias terms that typically vary strongly with instrument temperature and otherwise drift very slowly over time, it is necessary to simultaneously estimate field sensor bias terms AND estimate attitude. Section 6.2.1 reviews relevant literature on attitude estimation, and Section 6.2.2 reviews relevant literature on IMU sensor bias estimation.

6.2.1 Attitude Estimation

The majority of the attitude estimation literature addresses the case of magnetic heading attitude estimation using MEMS IMUs [12, 19, 20, 37, 38, 78]. [35] report an attitude nonlinear complementary filter on $SO(3)$. A recent study by [10] explores utilizing a FOG for attitude estimation under unknown magnetic disturbances. These studies however, differ from the current paper as they estimate magnetic-North heading, while the present paper presents an estimator for true-North heading.

[36] reports a method for estimating roll and pitch using a three-axis accelerometer and three-axis gyroscope IMU and a monocular camera. This approach however is impractical for many UV applications (e.g. when there

is poor visibility due to water turbidity, operating in the mid-water, operating in a region with a featureless bottom) and impossible for the many unmanned underwater vehicles (UUVs) that are not equipped with cameras and lights/strobes.

[4] report a nonlinear attitude observer based upon angular rate gyros and single body-fixed vector measurements of a constant "inertial vector" (e.g. 3-axis magnetometer) where the gyros and fixed-vector sensor are all assumed to be bias-free. A numerical simulation evaluation is reported.

Unlike AHRSs which use magnetometers to estimate magnetic heading, true-North gyrocompasses estimate geodetic true north without the use of magnetometers. Lèon Foucault first predicted that the gyroscope could be used as a compass in 1852. During the early twentieth century, Dr. Hermann Franz Joseph Hubertus Maria Anschütz-Kaempfe and Elmer Sperry began work on developing gyrocompasses based on the prior work by Foucault. In 1906, Anschütz-Kaempfe began designing a gyrocompass for his under ice submarine called "The U-Boat in Service of Polar Exploration" and conducted sea trials on the Deutschland in 1908. Shortly after in late 1907 or early 1908, Sperry began the development of his own gyrocompass [23].

The first practical gyrocompass system was patented by Elmer Sperry in 1911 [23, 57, 69]. Sperry's original gyrocompass was centered around a high accuracy mechanical gyroscope, and in WWI and WWII, Sperry gyrocompasses were widely equipped on warships and airplanes as the primary navigational instrument. While the first gyrocompass systems were mechanical, the invention of ring laser gyros (RLGs) in the 1960s [34] and fiber optic

gyroscopes (FOGs) in the 1970s [73] enabled optical gyroscopes to be used in gyrocompasses. It is commonly understood that most modern commercial of the shelf true-North gyrocompasses utilize a high-end gyroscope and accelerometer in an EKF framework to estimate sensor biases and attitude. The gyrocompass system reported in this chapter differs from previous gyrocompasses by utilizing full nonlinear adaptive observers without linearization.

Preliminary studies by the author [58, 59] suggest the practical utility of a low-cost FOG IMU as the primary sensor in a North-seeking gyrocompass system. These studies assume that sensor biases have been calculated and compensated for *a priori* and rely on the differentiation of accelerometer measurements for estimating true-North. Numerical simulation and experimental evaluations are reported.

[64] presents a true-North gyrocompass system which estimates true-North attitude without the need to differentiate accelerometer measurements and also addresses the problem of real time bias estimation for both gyros and accelerometers. The current chapter differs from the previous attitude observer by generalizing the algorithm to be used with general field vector measurements and provides a local asymptotic stability proof and observability analysis. Numerical simulation and full-scale vehicle experimental evaluations are reported.

6.2.2 Inertial Measurement Unit (IMU) Sensor Bias Estimation

Several methods for IMU measurement bias estimation have been reported in recent years. Much of this literature, though, focuses on magnetometer bias estimation [1, 2, 11, 17, 19, 31, 33, 61, 70, 72].

Many papers report results for gyro sensor bias estimation. However, most address MEMS gyro sensor bias estimation in which the angular rate due to Earth's rotation is ignored in the gyro measurement model. They use a measurement model similar to that of (6.1) and neglect the Earth rate term because Earth rate is dynamically undetectable with MEMS gyros.

[18] report an identifier for accelerometer and gyroscope sensor bias. However, they utilize GPS which is unavailable to submerged vehicles.

[53] and [54] also report a sensor bias estimator for 6-DOF IMUs utilizing computer vision. This method though is dependent on the presence of a computer vision system, which requires illumination of optical identification markers in the environment and a camera system which is unavailable for many robotic vehicles (e.g. many underwater vehicles).

[37, 38] and [50] report nonlinear complementary filters for estimating attitude and gyroscope sensor bias. While these estimators identify angular-rate sensor bias, they do not address linear acceleration sensor bias and do not distinguish the gyroscope sensor bias from Earth's angular velocity.

[60] addresses the problem of identifying and distinguishing the gyro bias from the Earth-rate signal. However, this reported approach requires knowledge of the instrument's real-time attitude.

[64] reports an adaptive sensor bias and north observer to be used in a true-North gyrocompass system *without a priori* knowledge of the instrument's attitude. The present chapter differs from this previous work by presenting a new formulation of the sensor bias estimation which relies on fewer assumptions, a proof of asymptotic stability (instead of only stability), and an approach for choosing observer gains.

6.3 Sensor Model

The sensor measurement models for angular rate and linear acceleration are

$$ {}^{i}w_e(t) = {}^{i}w_E(t) + {}^{i}w_v(t) + {}^{i}w_b \tag{6.3} $$

$$ {}^{i}w_m(t) = {}^{i}w_e(t) + {}^{i}\eta_w(t) \tag{6.4} $$

$$ {}^{i}a_e(t) = {}^{i}a_g(t) + {}^{i}a_v(t) + {}^{i}a_b \tag{6.5} $$

$$ {}^{i}a_m(t) = {}^{i}a_e(t) + {}^{i}\eta_a(t) \tag{6.6} $$

where ${}^{i}w_m(t) \in \mathbb{R}^3$ is the IMU measured angular-rate, ${}^{i}w_e(t) \in \mathbb{R}^3$ is the biased noise-free angular-rate, ${}^{i}w_E(t) \in \mathbb{R}^3$ is the true angular velocity due to the rotation of the Earth, ${}^{i}w_v(t) \in \mathbb{R}^3$ is the true angular velocity due to the rotation of the instrument with respect to the NED frame, ${}^{i}w_b \in \mathbb{R}^3$ is the angular velocity sensor bias offset, ${}^{i}\eta_w(t) \in \mathbb{R}^3$ is the zero-mean Gaussian angular velocity sensor noise, ${}^{i}a_m(t) \in \mathbb{R}^3$ is the IMU measured linear acceleration, ${}^{i}a_e(t) \in \mathbb{R}^3$ is the biased noise-free linear acceleration, ${}^{i}a_g(t) \in \mathbb{R}^3$ is the true linear acceleration due to gravity and the Earth's rotation, ${}^{i}a_v(t)$ is

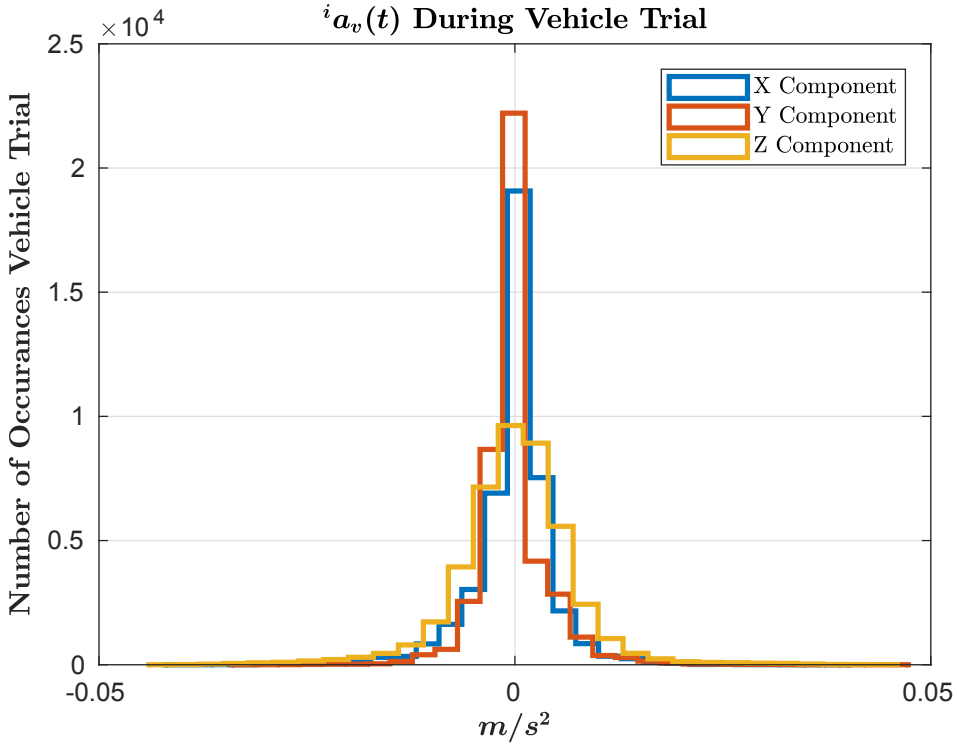

Figure 6.1: Histogram of the components of the vehicle acceleration experience by the JHU ROV during the vehicle trial. The vehicle acceleration data is from the high-end PHINS INS on the JHU ROV. As shown above, the vehicle experiences vehicle accelerations which are orders of magnitude smaller than gravity ($<< 9.81 \ \ m/s^2$).

the instrument's true linear acceleration with respect to Earth, ${}^{i}a_{b} \in \mathbb{R}^3$ is the linear accelerometer sensor bias, and ${}^{i}\eta_{a}(t) \in \mathbb{R}^3$ is the zero-mean Gaussian linear accelerometer sensor noise.

For many robotic vehicles, the gravitational field ${}^{i}a_{g}(t)$ dominates the vehicle linear acceleration (${}^{i}a_{v}(t)$). Thus, it is common to use the approximation

$$ {}^{i}a_{e}(t) \approx {}^{i}a_{g}(t) + {}^{i}a_{b} \tag{6.7} $$

as a low-frequency estimate of (6.5). This approximation, (6.7), is used in [10, 35, 50, 78]. Figure 6.1 presents the vehicle acceleration experienced by

the JHU ROV in the vehicle trial. From Figure 6.1, it is evident that the magnitude of the vehicle accelerations experienced in the vehicle trial are orders of magnitude smaller than the gravity vector.

Given (6.7), the sensor measurement model becomes

$$^{i}w_e(t) = {}^{i}w_E(t) + {}^{i}w_v(t) + {}^{i}w_b \tag{6.8}$$

$$^{i}w_m(t) = {}^{i}w_e(t) + {}^{i}\eta_w(t) \tag{6.9}$$

$$^{i}a_e(t) = {}^{i}a_g(t) + {}^{i}a_b \tag{6.10}$$

$$^{i}a_m(t) = {}^{i}a_e(t) + {}^{i}\eta_a(t). \tag{6.11}$$

Section 6.8.5 shows the proposed algorithms perform well in the experimental trial where the vehicle experienced small vehicle accelerations ($\|{}^{i}a_v(t)\| \approx 0$), thus empirically justifying the neglection of the vehicle acceleration term ${}^{i}a_v(t)$ in (6.7) for a slowly accelerating vehicle.

6.4 Sensor Bias and East Observer

This section reports the derivation and stability analysis of an adaptive sensor bias and East vector observer for six-DOF IMUs equipped with a three-axis accelerometer and three-axis angular rate gyroscope. The field sensor biases are assumed to be very slowly time varying, and hence we model them as constant terms and update their estimates continuously.

Note that to estimate true-North heading, the angular rate gyroscope must be sensitive enough to detect Earth-rate. The measurement noise of present-day angular rate gyros in MEMS IMUs is orders of magnitude larger than what is needed to detect the extremely minute signal of the Earth's rotation rate (15°/hr), thus, MEMS IMUs cannot be utilized to dynamically estimate directly true-North heading. At present, true-North attitude can only be successfully instrumented with high-end, angular-rate gyros that employ RLG or FOG angular rate sensors, or that employ large inertial-grade mechanical gyrocompasses. Although high-end angular-rate gyros are necessary for true-North gyrocompasses, the systems do not simply employ a better IMU (more precise, without ferromagnetic disturbances) to obtain more precise results using common algorithms utilizing magnetic heading sensors, but rather use the local gravity vector and Earth's rotation axis for estimating true-North attitude. This is impossible with an IMU that is not sensitive enough to detect Earth's rotation.

The present chapter reports a system that successfully estimates true-North attitude utilizing a new class of compact, low-power, and lower cost FOG IMUs.

6.4.1 System Model

We consider the system model

$$^{N}a_g = {}^{N}_{i}R(t)\,{}^{i}a_g(t) \tag{6.12}$$

$$^{N}e = {}^{N}_{i}R(t)\,{}^{i}e(t) \tag{6.13}$$

where the "East" vector,

$$^{i}e(t) = \mathcal{J}\left(^{i}w_E(t)\right)\,^{i}a_g(t), \tag{6.14}$$

is defined as the cross product of the Earth's rotation axis with the local gravity vector. Note that the proposed observer will not work well near the geographic north and south poles where the local gravity vector is close to collinear with the Earth's rotation axis.

Since $^{N}a_g$ and ^{N}e are constant in the NED frame, differentiating (6.12) and (6.13), rearranging terms, and substituting (6.8) yields

$$^{i}\dot{a}_g(t) = -\mathcal{J}\left(^{i}w_e(t) - {}^{i}w_b - {}^{i}w_E(t)\right)\,^{i}a_g(t) \tag{6.15}$$

$$^{i}\dot{e}(t) = -\mathcal{J}\left(^{i}w_e(t) - {}^{i}w_b - {}^{i}w_E(t)\right)\,^{i}e(t). \tag{6.16}$$

From (6.10), we know that

$$^{i}a_g(t) = {}^{i}a_e(t) - {}^{i}a_b \tag{6.17}$$

$$\begin{aligned} ^{i}\dot{a}_g(t) &= {}^{i}\dot{a}_e(t) - {}^{i}\dot{a}_b \\ &= {}^{i}\dot{a}_e(t). \end{aligned} \tag{6.18}$$

Substituting (6.10), (6.14), and (6.18) into (6.15) and (6.16) results in

$$\begin{aligned} ^{i}\dot{a}_e(t) &= -\mathcal{J}\left(^{i}w_e(t) - {}^{i}w_b\right)\,^{i}a_g(t) + {}^{i}e(t) \\ &= -\mathcal{J}\left(^{i}w_e(t) - {}^{i}w_b\right)\left({}^{i}a_e(t) - {}^{i}a_b\right) + {}^{i}e(t). \end{aligned} \tag{6.19}$$

Since the cross products between sensor biases and Earth-rate are orders of magnitude smaller than the other signals, we make the approximations that $\mathcal{J}\left({}^{i}w_b\right){}^{i}a_b \approx 0$ and $\mathcal{J}\left({}^{i}w_b + {}^{i}w_E(t)\right){}^{i}e(t) \approx 0$. Note that for the KVH FOG IMU used in the present chapter, $\|\mathcal{J}\left({}^{i}w_b\right){}^{i}a_b\|$ is order 10^{-7} and $\|\mathcal{J}\left({}^{i}w_b + {}^{i}w_E(t)\right){}^{i}e(t)\|$ is order 10^{-7}, while $\|\mathcal{J}\left({}^{i}w_e(t)\right)\left({}^{i}a_e(t) - {}^{i}a_b\right)\|$ is order $\geq 10^{-4}$, $\|\mathcal{J}\left({}^{i}w_b\right){}^{i}a_e(t)\|$ is order 10^{-1}, $\|{}^{i}e(t)\|$ is order 10^{-4}, and $\|\mathcal{J}\left({}^{i}w_e(t)\right){}^{i}e(t)\|$ is order $\|{}^{i}w_v(t)\| * 10^{-4}$.

The resulting plant is

$$ {}^{i}\dot{a}_e(t) = -\mathcal{J}\left({}^{i}w_e(t)\right)\left({}^{i}a_e(t) - {}^{i}a_b\right) + \mathcal{J}\left({}^{i}w_b\right){}^{i}a_e(t) + {}^{i}e(t) \tag{6.20} $$

$$ {}^{i}\dot{e}(t) = -\mathcal{J}\left({}^{i}w_e(t)\right){}^{i}e(t) \tag{6.21} $$

$$ {}^{i}\dot{w}_b = 0 \tag{6.22} $$

$$ {}^{i}\dot{a}_b = 0 \tag{6.23} $$

$$ y(t) = {}^{i}a_e(t). \tag{6.24} $$

6.4.2 Sensor Bias and East Observer Update Law

We propose the observer

$$ {}^{i}\dot{\hat{a}}_e(t) = -\mathcal{J}\left({}^{i}w_e(t)\right)\left({}^{i}\hat{a}_e(t) - {}^{i}\hat{a}_b\right) + \mathcal{J}\left({}^{i}\hat{w}_b\right){}^{i}\hat{a}_e(t) + {}^{i}\hat{e}(t) - k_a\Delta a(t) \tag{6.25} $$

$$ {}^{i}\dot{\hat{e}}(t) = -\mathcal{J}\left({}^{i}w_e(t)\right){}^{i}\hat{e}(t) - k_e\Delta a(t) \tag{6.26} $$

$$ {}^{i}\dot{\hat{w}}_b(t) = -k_{b_w}\mathcal{J}\left({}^{i}a_e(t)\right)\Delta a(t) \tag{6.27} $$

$$ {}^{i}\dot{\hat{a}}_b(t) = k_{b_a}\mathcal{J}\left({}^{i}w_e(t)\right)\Delta a(t) \tag{6.28} $$

$$ \hat{y}(t) = {}^{i}\hat{a}_e(t) \tag{6.29} $$

where k_a, k_e, k_{b_w}, and k_{b_a} are constant positive scalar gains, ${}^{i}\hat{a}_e(t)$, ${}^{i}\hat{e}(t)$, ${}^{i}\hat{w}_b(t)$, and ${}^{i}\hat{a}_b(t)$ are the estimates of ${}^{i}a_e(t)$, ${}^{i}e(t)$, ${}^{i}w_b$, and ${}^{i}a_b$ respectively, and

$$ \Delta a(t) = {}^{i}\hat{a}_e(t) - {}^{i}a_e(t) \tag{6.30} $$

$$ \Delta e(t) = {}^{i}\hat{e}(t) - {}^{i}e(t) \tag{6.31} $$

$$ \Delta w_b(t) = {}^{i}\hat{w}_b(t) - {}^{i}w_b \tag{6.32} $$

$$ \Delta a_b(t) = {}^{i}\hat{a}_b(t) - {}^{i}a_b \tag{6.33} $$

$$ \Delta y(t) = \hat{y}(t) - y(t) \tag{6.34} $$

are the corresponding error terms.

Note that in the proposed algorithm, the signals ${}^{i}w_e(t)$ and ${}^{i}a_e(t)$ are the only signals in the instrument frame needed for the algorithm to work. Knowledge of ${}^{N}a_g$ and ${}^{N}w_E$ is not needed.

6.4.3 Error System

The resulting error system is

$$\begin{aligned}\Delta\dot{a}(t) = &-\mathcal{J}\left({}^{i}w_e(t)\right)\Delta a(t) + \mathcal{J}\left({}^{i}w_e(t)\right)\Delta a_b(t) \\ &+ \mathcal{J}\left({}^{i}\hat{w}_b(t)\right)\Delta a(t) - \mathcal{J}\left({}^{i}a_e(t)\right)\Delta w_b(t) + \Delta e(t) - k_a\Delta a(t) \quad (6.35)\end{aligned}$$

$$\Delta\dot{e}(t) = -\mathcal{J}\left({}^{i}w_e(t)\right)\Delta e(t) - k_e\Delta a(t) \quad (6.36)$$

$$\Delta\dot{w}_b(t) = -k_{b_w}\mathcal{J}\left({}^{i}a_e(t)\right)\Delta a(t) \quad (6.37)$$

$$\Delta\dot{a}_b(t) = k_{b_a}\mathcal{J}\left({}^{i}w_e(t)\right)\Delta a(t) \quad (6.38)$$

$$\Delta y(t) = \Delta a(t). \quad (6.39)$$

6.4.4 Stability

Consider the Lyapunov function candidate

$$\begin{aligned}V = &\frac{1}{2}\Delta a^T(t)\Delta a(t) + \frac{1}{2k_e}\Delta e^T(t)\Delta e(t) + \frac{1}{2k_{b_w}}\Delta w_b^T(t)\Delta w_b(t) \\ &+ \frac{1}{2k_{b_a}}\Delta a_b^T(t)\Delta a_b(t) \quad (6.40)\end{aligned}$$

where V is a smooth, positive definite, and radially unbounded function by construction. Differentiating (6.40) results in

$$\begin{aligned}
\dot{V} &= \Delta a^T(t)\Delta\dot{a}(t) + \frac{1}{k_e}\Delta\dot{e}^T(t)\Delta e(t) + \frac{1}{k_{b_w}}\Delta\dot{w}_b^T(t)\Delta w_b(t) + \frac{1}{k_{b_a}}\Delta\dot{a}_b^T(t)\Delta a_b(t) \\
&= \left(-\Delta a^T(t)\mathcal{J}\left({}^i a_e(t)\right) + \Delta a^T(t)\mathcal{J}\left({}^i a_e(t)\right)\right)\Delta w_b(t) \\
&\quad + \left(\Delta a^T(t)\mathcal{J}\left({}^i w_e(t)\right) - \Delta a^T(t)\mathcal{J}\left({}^i w_e(t)\right)\right)\Delta a_b(t) \\
&\quad + \left(\Delta a^T(t) - \Delta a^T(t)\right)\Delta e(t) + \frac{1}{k_e}\Delta e^T(t)\mathcal{J}\left({}^i w_e(t)\right)\Delta e(t) \\
&\quad + \Delta a^T(t)\mathcal{J}\left({}^i\hat{w}_b(t) - {}^i w_e(t)\right)\Delta a(t) - k_a\Delta a^T(t)\Delta a(t) \\
&= -k_a\|\Delta a(t)\|^2 \\
&\leq 0.
\end{aligned} \tag{6.41}$$

Since k_a is a positive scalar, the time derivative of the Lyapunov function is negative semidefinite and the observer is globally stable.

Since (6.40) is radially unbounded, bounded below by 0, and bounded above by its initial value, $V(t_0)$, due to (6.41), we can conclude that $\Delta a(t)$, $\Delta e(t)$, $\Delta w_b(t)$, and $\Delta a_b(t)$ are bounded. If we make the assumption that the signals ${}^i a_e(t)$, ${}^i w_e(t)$, ${}^i w_b$, and ${}^i a_b$ are bounded, then (6.35)-(6.39) are bounded, and hence (6.30)-(6.33) are uniformly continuous.

For all $t \geq 0$,

$$-\int_{t_0}^{t} \dot{V}(\tau)\, d\tau = \int_{t_0}^{t} k_a \|\Delta a(\tau)\|^2\, d\tau$$

$$V(t_0) - V(t) = k_a \int_{t_0}^{t} \|\Delta a(\tau)\|^2\, d\tau$$

$$V(t_0) = k_a \int_{t_0}^{t} \|\Delta a(\tau)\|^2\, d\tau + V(t). \tag{6.42}$$

Since $V(t) \geq 0\ \forall t > t_0$, (6.42) can be written as

$$k_a \int_{t_0}^{t} \|\Delta a(\tau)\|^2\, d\tau \leq V(t_0)$$

$$\left(\int_{t_0}^{t} \|\Delta a(\tau)\|^2\, d\tau\right)^{1/2} \leq \left(\frac{V(t_0)}{k_a}\right)^{1/2}. \tag{6.43}$$

Hence, $\Delta a(t) \in L^2$ [27].

Since $\Delta a(t) \in L^2 \cap L^\infty$ and $\Delta \dot{a}(t)$ is bounded, from Corollary 2.9 in [42], we conclude that $\Delta a(t)$ is globally asymptotically stable at the origin,

$$\lim_{t \to \infty} \Delta a(t) = 0. \tag{6.44}$$

Note that we can rewrite the error system into the form

$$\dot{\theta}(t) = A(t)\theta(t) + f(t) \tag{6.45}$$

$$y(t) = C\theta(t) \tag{6.46}$$

where

$$\theta(t) = \begin{bmatrix} \Delta a(t) \\ \Delta e(t) \\ \Delta w_b(t) \\ \Delta a_b(t) \end{bmatrix}, \tag{6.47}$$

$$A(t) = \begin{bmatrix} 0 & g(t) \\ 0 & 0 \end{bmatrix}, \tag{6.48}$$

$$g(t) = \begin{bmatrix} I & -\mathcal{J}\left({}^{i}a_e(t)\right) & \mathcal{J}\left({}^{i}w_e(t)\right) \\ -\mathcal{J}\left({}^{i}w_e(t)\right) & 0 & 0 \end{bmatrix}, \tag{6.49}$$

$$f(t) = \begin{bmatrix} -\mathcal{J}\left({}^{i}w_e(t) - \hat{w}_b(t)\right) - k_a I \\ -k_e I \\ -k_{b_w}\mathcal{J}\left({}^{i}a_e(t)\right) \\ k_{b_a}\mathcal{J}\left({}^{i}w_e(t)\right) \end{bmatrix} \Delta a(t), \tag{6.50}$$

$$C = \begin{bmatrix} I & 0 & 0 & 0 \end{bmatrix}, \tag{6.51}$$

and $I \in \mathbb{R}^{3\times 3}$ is the identity matrix. Since $\lim_{t\to\infty} \Delta a(t) = 0$, we conclude that

(i) $\lim_{t\to\infty} \|y(t)\| = 0$

(ii) $\lim_{t\to\infty} \|f(t)\| = 0$

Thus, if $[A(t), C]$ is UCO, from Lemma 1, page 16, we conclude the error system is asymptotically stable and hence

$$\lim_{t\to\infty} \|\theta(t)\| = 0. \tag{6.52}$$

We conclude that, if ${}^{i}a_e(t)$, ${}^{i}w_e(t)$, ${}^{i}w_b$, and ${}^{i}a_b$ are bounded and $[A(t), C]$ is

UCO, then the system is asymptotically stable. Note that for UVs, the signals ${}^{i}a_e(t)$, ${}^{i}w_e(t)$, ${}^{i}w_b$, and ${}^{i}a_b$ are all bounded (see Figure 6.18 for the sensor measurements from the numerical simulations and vehicle trial), so convergence of the observer is dependent on $[A(t), C]$ being UCO. In our case, where $A(t)$ depends on the coupled exogenous signals ${}^{i}w_e(t)$ and ${}^{i}a_e(t)$, it is not obvious that $\Phi(t, t_0)$ (the transition matrix for $A(t)$) has a closed-form solution for non-trivial ${}^{i}w_e(t)$ and ${}^{i}a_e(t)$, and, in consequence, it is not clear how to prove analytically that the observability grammian $N(t_0, \delta)$, defined in (2.18), satisfies (2.17). It is easy to verify numerically that when ${}^{i}w_e(t)$ and ${}^{i}a_e(t)$ are PE, $[A(t), C]$ is UCO. Conversely, it is also easy to verify numerically that when ${}^{i}w_e(t)$ and ${}^{i}a_e(t)$ are not PE, $[A(t), C]$ is not UCO. Section 6.5 reports numerical evaluations of the observability gramian for the simulation data presented in Section 6.8.

6.5 Uniform Complete Observability (UCO) Of The Sensor Bias and East Observer

As stated in Section 6.4.4, asymptotic convergence of the sensor bias and East observer to the true values is dependent on $[A(t), C]$ being uniformly completely observable (UCO). However, it is not obvious that $\Phi(t, t_0)$, the transition matrix for $A(t)$, has a closed-form solution for non-trivial ${}^{i}w_e(t)$ and ${}^{i}a_e(t)$ and, in consequence, it is not clear how to prove analytically that the observability gramian

$$N(t_0, \delta) = \int_{t_0}^{t_0+\delta} \Phi^T(\tau, t_0) C^T C \Phi(\tau, t_0)\, d\tau \tag{6.53}$$

satisfies (2.17).

We have, however, verified numerically that when ${}^{i}w_e(t)$ and ${}^{i}a_e(t)$ are PE, $[A(t), C]$ is UCO. Figures 6.3-6.5 present the instrument measurements from the three simulations. The following subsections present results from numerically evaluating the observability gramian of the three simulations.

6.5.1 Sim1 Simulation

In **sim1**, ${}^{i}w_e(t)$ and ${}^{i}a_e(t)$ are constant (i.e. heading, pitch, and roll are all uniformly zero), and thus, not persistently exciting (PE). Hence, the observability gramian for $[A(t), C]$ is not full rank and $[A(t), C]$ is not UCO. Numerically, we can verify that $\text{rank}\,(N(0, 60)) = 6$, $\sigma_{min}(N(0, 60)) = 4.59 \times 10^{-12}$, and $\sigma_{max}(N(0, 60)) = 6.96 \times 10^{6}$ (full rank occurs when $\text{rank}\,(N(0, 60)) = 12$).

6.5.2 Sim2 Simulation

In **sim2**, the vehicle only experiences changes in heading only, with uniformly zero roll and pitch, and ${}^{i}w_e(t)$ and ${}^{i}a_e(t)$ are not PE. Hence, the observability gramian for $[A(t), C]$ is not full rank and $[A(t), C]$ is not UCO. Numerically, we can verify that $\text{rank}\,(N(0, 60)) = 10$, $\sigma_{min}(N(0, 60)) = 3.76 \times 10^{-12}$, and $\sigma_{max}(N(0, 60)) = 6.90 \times 10^{6}$ (full rank occurs when $\text{rank}\,(N(0, 60)) = 12$).

6.5.3 Sim3 Simulation

In **sim3**, the vehicle experiences changes in roll, pitch, and heading, and ${}^{i}w_e(t)$ and ${}^{i}a_e(t)$ are PE. The observability gramian for $[A(t), C]$ can be shown

numerically to be full rank and, in consequence, $[A(t), C]$ is UCO. Numerically, we can verify that rank $(N(0,60)) = 12$, $\sigma_{min}(N(0,60)) = 1.04$, and $\sigma_{max}(N(0,60)) = 4.89 \times 10^6$ (full rank occurs when rank $(N(0,60)) = 12$).

6.5.4 Conclusion

We conclude from numerically evaluating the observability gramians over $t = [0,60]$ from the three simulations, that when ${}^{i}w_e(t)$ and ${}^{i}a_e(t)$ are PE (**sim3**), the observer is asymptotically stable. Note that during **sim2**, although the observability gramian is not full rank, excitement in heading (**sim2**) causes the observability gramian to be rank 10, which is a higher rank than in the case of a stationary instrument (**sim1**).

6.6 Attitude Observer

This section reports the derivation and stability analysis of an attitude observer that estimates directly on $SO(3)$. The observer is inspired in part by the research of [35] on nonlinear complementary filters on $SO(3)$ and research by [28] on adaptive identification on $SO(3)$. The general terms x and z are used because the observer is not limited to the problem of true-North attitude estimation — it can also be applied (for example) to magnetometer-IMU systems for attitude estimation with respect to local magnetic-North.

6.6.1 Plant

Consider the plant

$$^{N}x = {}^{N}_{i}R(t)\,{}^{i}x(t) \tag{6.54}$$

$$^{N}z = {}^{N}_{i}R(t)\,{}^{i}z(t) \tag{6.55}$$

where ${}^{i}x(t)$ and ${}^{i}z(t)$ are orthogonal such that ${}^{i}x^{T}(t)\,{}^{i}z(t) = 0$. The signals ${}^{N}x \in \mathbb{R}^3$, ${}^{i}x(t) \in \mathbb{R}^3$, ${}^{N}z \in \mathbb{R}^3$, and ${}^{i}z(t) \in \mathbb{R}^3$ are known and non-zero. The rotation matrix ${}^{N}_{i}R(t) \in SO(3)$ is unknown.

6.6.2 Identification Plant

Define ${}^{N}_{i}\hat{R}(t) \in SO(3)$ to be the estimate of ${}^{N}_{i}R(t)$, and ${}^{N}\hat{x}, {}^{N}\hat{z} \in \mathbb{R}^3$ to be the estimated plant output

$$^{N}\hat{x} = {}^{N}_{i}\hat{R}(t)\,{}^{i}x(t) \tag{6.56}$$

$$^{N}\hat{z} = {}^{N}_{i}\hat{R}(t)\,{}^{i}z(t), \tag{6.57}$$

where ${}^{i}x(t), {}^{i}z(t)$ are "field vectors". In out particular instance, the field vectors are ${}^{i}a_{g}(t), {}^{i}e(t)$ respectively.

6.6.3 Parameter Error

The parameter error is defined as

$$\tilde{R}(t) = {}^{N}_{i}R^{T}(t)\,{}^{N}_{i}\hat{R}(t). \tag{6.58}$$

When ${}^{N}_{i}\hat{R}(t) = {}^{N}_{i}R(t)$, ${}^{N}_{i}R^{T}(t)\,{}^{N}_{i}\hat{R}(t) = I$ where I is the 3×3 identity matrix.

6.6.4 Attitude Observer Update Law

We choose the update law

$$ {}^N_i\dot{\hat{R}}(t) = {}^N_i\hat{R}(t)\mathcal{J}\left(\tilde{x}(t) + \tilde{z}(t) + {}^i w_e(t) - {}^i w_b - {}^N_i\hat{R}^T(t)\,{}^N w_E\right). \tag{6.59} $$

where the $\tilde{x}(t) \in \mathbb{R}^3$ and $\tilde{z}(t) \in \mathbb{R}^3$ are local field vector error terms defined, respectively, as

$$ \tilde{x}(t) = k_x(t)\mathcal{J}\left({}^i x(t)\right) {}^N_i\hat{R}^T(t)\,{}^N x \tag{6.60} $$

$$ \tilde{z}(t) = k_z(t)\mathcal{J}\left((I - P(t))\,{}^i z(t)\right) {}^N_i\hat{R}^T(t)\,{}^N z \tag{6.61} $$

where the projection matrix, $P(t)$, and normalized vector ${}^i\bar{x}(t)$ are defined as

$$ P(t) = {}^i\bar{x}(t)\,{}^i\bar{x}^T(t), \tag{6.62} $$

$$ {}^i\bar{x}(t) = {}^i x(t)\frac{1}{\|{}^i x(t)\|}, \tag{6.63} $$

and $k_x(t)$ and $k_z(t)$ are positive scalar gains.

6.6.5 Error System

The corresponding error system is

$$ \begin{aligned} \dot{\tilde{R}}(t) &= {}^N_i\dot{R}^T(t)\,{}^N_i\hat{R}(t) + {}^N_i R^T(t)\,{}^N_i\dot{\hat{R}}(t) \\ &= -\mathcal{J}\left({}^i w_v(t)\right)\tilde{R}(t) + \tilde{R}(t)\mathcal{J}\left(\tilde{x}(t) + \tilde{z}(t) + {}^i w_e(t) - {}^i w_b - {}^N_i\hat{R}^T(t)\,{}^N w_E\right). \end{aligned} \tag{6.64} $$

Using the property $\mathcal{J}(v)R = R\mathcal{J}(R^T v)$ for $v \in \mathbb{R}^3$ and $R \in SO(3)$, (6.64) becomes

$$\begin{aligned}\dot{\tilde{R}}(t) &= \tilde{R}(t)\mathcal{J}\left(\tilde{x}(t) + \tilde{z}(t) + {}^i w_e(t) - {}^i w_b - \tilde{R}^T(t){}^i w_E(t) - \tilde{R}^T(t){}^i w_v(t)\right) \\ &= \tilde{R}(t)\mathcal{J}\left(\tilde{x}(t) + \tilde{z}(t) + {}^i w_{Ev}(t) - \tilde{R}^T(t){}^i w_{Ev}(t)\right) \end{aligned} \tag{6.65}$$

where

$${}^i w_{Ev}(t) = {}^i w_E(t) + {}^i w_v(t). \tag{6.66}$$

6.6.6 Stability

Consider the Lyapunov function candidate

$$V = \frac{1}{2}\tilde{q}^T(t)\tilde{q}(t) \tag{6.67}$$

where V is a smooth, positive definite function by construction and $\tilde{q}(t)$ defined in (2.7). Note that in the following stability proof, the fact $\mathcal{J}(v)v = 0$ $\forall v \in \mathbb{R}^3$, and consequently $q^T A^{-1}(q) = q^T$ is used repeatedly.

Differentiating (6.67) yields

$$\dot{V} = \tilde{q}^T(t)\dot{\tilde{q}}(t). \tag{6.68}$$

Substituting (2.15) into (6.68) results in

$$\dot{V} = \tilde{q}^T(t)\left(A^{-1}\left(\tilde{q}(t)\right)\mathcal{J}^{-1}\left(\tilde{R}^T(t)\dot{\tilde{R}}(t)\right)\right), \tag{6.69}$$

and substituting (2.12) and (6.65) into (6.69) results in

$$\dot{V} = \tilde{q}^T(t)\left(\tilde{x}(t) + \tilde{z}(t) + {}^i w_{Ev}(t) - \tilde{R}^T(t)\,{}^i w_{Ev}(t)\right). \tag{6.70}$$

Substituting (2.4) into (6.70) yields

$$\begin{aligned}\dot{V} &= \tilde{q}^T(t)\left(\tilde{x}(t) + \tilde{z}(t) + {}^i w_{Ev}(t) - \left(I - \gamma(t)\mathcal{J}\left(\tilde{q}(t)\right) + \kappa(t)\mathcal{J}^2\left(\tilde{q}(t)\right)\right){}^i w_{Ev}(t)\right) \\ &= \tilde{q}^T(t)\left(\tilde{x}(t) + \tilde{z}(t) + {}^i w_{Ev}(t) - {}^i w_{Ev}(t)\right) \\ &= \tilde{q}^T(t)\left(\tilde{x}(t) + \tilde{z}(t)\right). \end{aligned} \tag{6.71}$$

Substituting (6.60), (6.61), into (6.71) yields

$$\begin{aligned}\dot{V} &= k_x(t)\tilde{q}^T(t)\mathcal{J}\left({}^i x(t)\right){}^N_i\hat{R}^T(t)\,{}^N x + k_z(t)\tilde{q}^T(t)\mathcal{J}\left(\left(I - P(t)\right){}^i z(t)\right){}^N_i\hat{R}^T(t)\,{}^N z \\ &= k_x(t)\tilde{q}^T(t)\mathcal{J}\left({}^i x(t)\right)\tilde{R}^T(t)\,{}^i x(t) + k_z(t)\tilde{q}^T(t)\mathcal{J}\left({}^i z(t)\right)\tilde{R}^T(t)\,{}^i z(t) \\ &\quad - k_z(t)\tilde{q}^T(t)\mathcal{J}\left({}^i\bar{x}(t)\,{}^i\bar{x}^T(t)\,{}^i z(t)\right)\tilde{R}^T(t)\,{}^i y(t). \end{aligned} \tag{6.72}$$

Note that since x is perpendicular to z, ${}^i x^T(t)\,{}^i z(t) = 0$. Thus, (6.72) becomes:

$$\dot{V} = k_x(t)\tilde{q}^T(t)\mathcal{J}\left({}^i x(t)\right)\tilde{R}^T(t)\,{}^i x(t) + k_z(t)\tilde{q}^T(t)\mathcal{J}\left({}^i z(t)\right)\tilde{R}^T(t)\,{}^i z(t). \tag{6.73}$$

Using the fact that $q(t)^T\mathcal{J}\left(x(t)\right)\mathcal{J}^2\left(q(t)\right)x(t) = 0$ and substituting (2.4) into

(6.73) yields

$$\begin{aligned}\dot{V} &= -k_x(t)\tilde{\gamma}(t)\tilde{q}^T(t)\mathcal{J}\left({}^i x(t)\right)\mathcal{J}\left(\tilde{q}(t)\right){}^i x(t) \\ &\quad - k_z(t)\tilde{\gamma}(t)\tilde{q}^T(t)\mathcal{J}\left({}^i z(t)\right)\mathcal{J}\left(\tilde{q}(t)\right){}^i z(t) \\ &= -k_x(t)\tilde{\gamma}(t)\|\mathcal{J}\left({}^i x(t)\right)\tilde{q}(t)\|^2 - k_z(t)\tilde{\gamma}(t)\|\mathcal{J}\left({}^i z(t)\right)\tilde{q}(t)\|^2 \\ &< 0 \end{aligned} \tag{6.74}$$

where $\tilde{\gamma}(t)$ is defined in (2.5). Thus, the time derivative of the Lyapunov function is locally negative definite and the observer is locally asymptotically stable.

6.7 Gyrocompass System

The gyrocompass system is comprised of the bias (Section 6.4) and attitude (Section 6.6) observers. The estimates of ${}^i e(t)$, ${}^i w_b$, and ${}^i a_b$ from the bias observer presented in Section 6.4 are utilized in real-time by the attitude

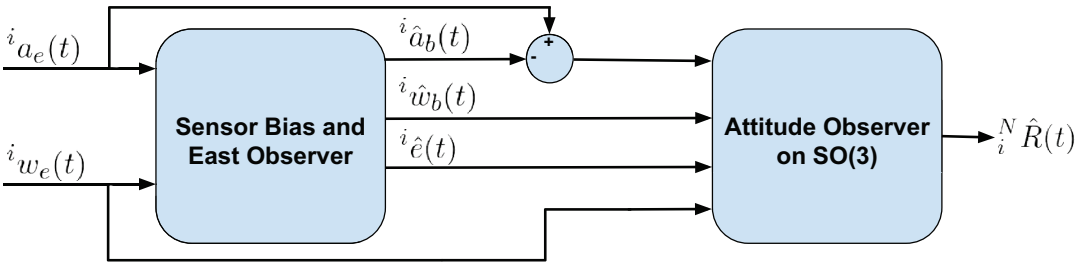

Figure 6.2: Block diagram of the gyrocompass system.

observer of Section 6.6 as follows:

$$ {}^{N}x = -\left(I_{3\times 3} + \frac{1}{g_0}\mathcal{J}({}^{N}w_E)^2 \right) \mathbf{e}_3, \tag{6.75} $$

$$ {}^{N}z = \mathcal{J}\left({}^{N}w_E\right) {}^{N}x, \tag{6.76} $$

$$ \mathbf{e}_3 = \begin{bmatrix} 0 & 0 & 1 \end{bmatrix}^T, \tag{6.77} $$

$$ {}^{i}x(t) = {}^{i}a_e(t) - {}^{i}\hat{a}_b(t), \tag{6.78} $$

$$ {}^{i}z(t) = {}^{i}\hat{e}(t), \tag{6.79} $$

$$ {}^{i}w_b = {}^{i}\hat{w}_b(t) \tag{6.80} $$

where g_0 is the magnitude of the local gravity field ($\sim 9.81\ m/s^2$).

The combined use of the reported East and bias observer (for accelerometers and angular rate sensor bias calibration on-the-fly) and the reported attitude observer will be termed the “gyrocompass system" in the following sections. Figure 6.2 shows a block diagram of the gyrocompass system.

6.8 Gyrocompass System Evaluation

The gyrocompass system is preliminarily evaluated in three numerical simulations and one UV experimental trial.

Note that in the derivation and stability proofs presented in Sections 6.4 and 6.6, the noise free case (6.8-6.10) of the measurement model is used. In the evaluation of the gyrocompass system, actual noisy sensor measurements (6.9-6.11) are used.

6.8.1 Gain Selection

As with most adaptive systems that rely on persistence of excitation [42, 52] to converge to the true parameter values, the rate of convergence is dependent on the amount of excitation the system is experiencing and observer gains. In order to choose the gyrocompass gains, a constrained optimization using MATLAB's nonlinear programing solver fmincon was used to select gains for the sensor bias and East observer.

The optimization was setup as follows:

- The $k_x(t) = 1$ and $k_y(t) = 1$ gains were held constant since these attitude observer gains are easy to tune by hand.
- The k_a, k_e, k_{b_w}, and k_{b_a} gains from the sensor bias and East observer are the parameters optimized over.
- RMSE of the roll, pitch, and heading from the gyrocompass system is the function optimized.

- A 30 minute long simulation sampled at 10Hz with $\|^i a_v(t)\| = 0$ was used. Note that the simulation was sampled at 10hz to allow the optimization to run faster and that this simulation experienced different instrument rotations than the simulations and vehicle trial presented in Sections 6.8.2-6.8.5.

- RMSE was started to be calculated 10 minutes after filter starts.

- Initial conditions were

$$k_a = 5.0 \cdot 10^{-1} \tag{6.81}$$

$$k_e = 1.0 \cdot 10^{-3} \tag{6.82}$$

$$k_{b_w} = 1.0 \cdot 10^{-5} \tag{6.83}$$

$$k_{b_a} = 5.0 \cdot 10^{-1}. \tag{6.84}$$

  These were chosen from previous experience with these gains working well.

- The constraints on the gain values were

$$0 < k_a < 10 \tag{6.85}$$

$$0 < k_e < 1 \tag{6.86}$$

$$0 < k_{b_w} < 1 \tag{6.87}$$

$$0 < k_{b_a} < 1 \tag{6.88}$$

The gains resulting from the optimization are

$$k_a = 3.3 \cdot 10^{-1} \tag{6.89}$$

$$k_e = 1.2 \cdot 10^{-3} \tag{6.90}$$

$$k_{b_w} = 1.5 \cdot 10^{-5} \tag{6.91}$$

$$k_{b_a} = 8.0 \cdot 10^{-1} \tag{6.92}$$

$$k_x(t) = 1 \tag{6.93}$$

$$k_y(t) = 1 \tag{6.94}$$

where $k_x(t)$ and $k_y(t)$ are the static gains chosen for the attitude observer. These gains were used during the simulations and vehicle experiment presented in this paper. We note that this gain optimization process did not result in gains that were significantly different from the initial gains that we manually selected, and did not result in significant improvements in observer performance.

Note: During the simulations and vehicle experiment, we gain-scheduled the sensor bias gains, k_{b_w} and k_{b_a}, by setting them to zero for the first minute of operation to allow the ${}^i\hat{e}(t)$ and ${}^i\hat{a}_e(t)$ signals to settle so that the sensor bias estimates are not driven far from their true values during the start-up transient period.

6.8.2 Simulation Setup

The gyrocompass system is evaluated in three numerical simulations.

- Sensor measurement sampling was simulated at 1kHz.
- Simulations include sensor biases consistent in magnitude to those seen in KVH 1775 IMUs.
- Simulations were for a latitude of 39.32°N (Baltimore, MD, USA).
- $\|{}^{i}a_{v}(t)\| = 0$ for the three simulations.
- Simulations included sensor measurements with sensor noise representative of the KVH 1775 FOG IMU (used ${}^{i}a_{m}(t)$ and ${}^{i}w_{m}(t)$ instead of ${}^{i}a_{e}(t)$ and ${}^{i}w_{e}(t)$). Angular velocity sensor and linear accelerometer sensor noises are computed from the IMU's specifications [32], as per [77], and confirmed by the authors experimentally to be $\sigma_{w} = 6.32 \times 10^{-3}$ rad/s and $\sigma_{a} = 0.0037$ g.
- The sensor biases used in the three simulations are:

$$w_{b} = \begin{bmatrix} -2 & 3 & -1 \end{bmatrix}^{T} \cdot 10^{-5} \ rad/s \tag{6.95}$$

$$a_{b} = \begin{bmatrix} 1 & -0.5 & 1 \end{bmatrix}^{T} \cdot 10^{-3} \ g \tag{6.96}$$

- The **sim1** simulation experienced no rotation. Figure 6.3 reports the IMU sensor measurements from **sim1**.

- The **sim2** simulation experienced changes in heading. Figure 6.4 reports the IMU sensor measurements from **sim2**.
- The **sim3** simulation experienced changes in heading, roll, and pitch. Figure 6.5 reports the IMU sensor measurements from **sim3**.
- Root mean square error (RMSE) was started to be calculated 20 minutes after filter starts.
- The initial condition, ${}^{N}_{i}\hat{R}(t)$, is chosen such that the initial heading is off by $\sim 30 - 35^{\circ}$. This is an initial heading that can be easily achieved with magnetic compasses. In the future, we plan to use the magnetometer in the KVH IMU for choosing the initial condition of the proposed gyrocompass system.
- The sensor biases estimates, ${}^{i}\hat{w}_{b}(t)$ and ${}^{i}\hat{a}(t)$, were all set to zero for their initial conditions.

6.8.3 Simulation Results

The estimated attitude and sensor bias errors for the three simulations are shown in Figures 6.6-6.17. Figure 6.6 reports the comparison between the reported gyrocompasses attitude estimate and the PHINS INS "ground truth" attitude for **sim1**. Figure 6.7 reports the corresponding attitude error for **sim1**. Figure 6.8 reports the **sim1** estimated angular rate bias errors, and Figure 6.9 reports the **sim1** estimated accelerometer bias errors. Similarly, Figures 6.10 and 6.11 report the **sim2** KVH vs PHINS attitude comparison and respective attitude errors, and Figures 6.12 and 6.13 report the **sim2** angular rate and

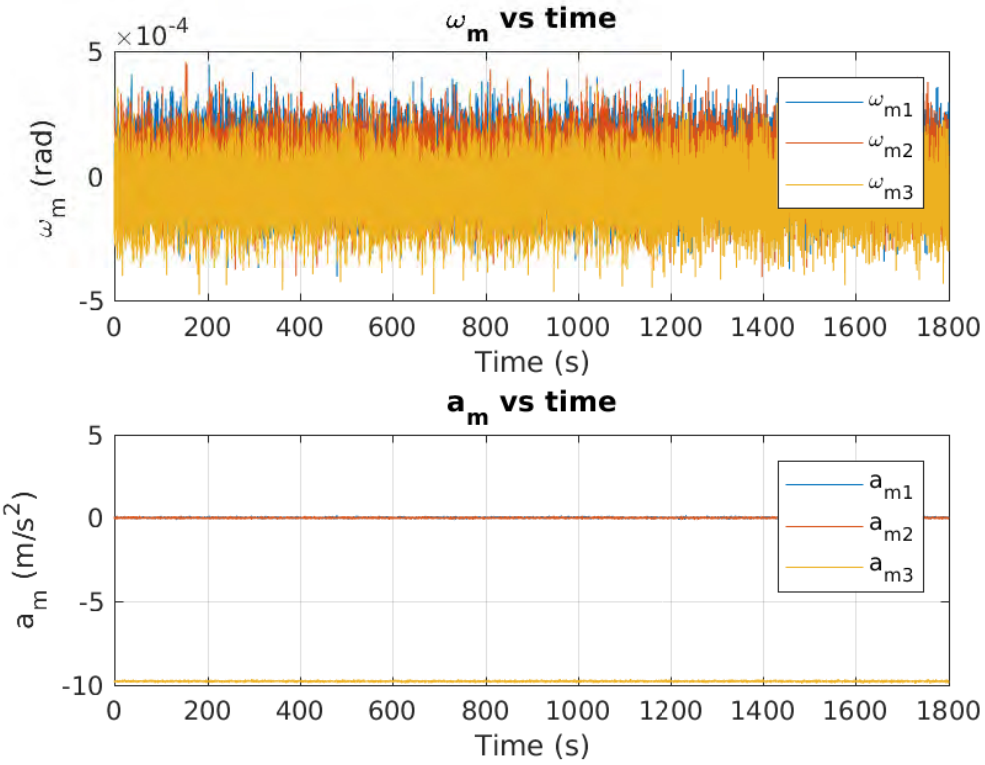

Figure 6.3: Sim1 KVH simulation measurements.

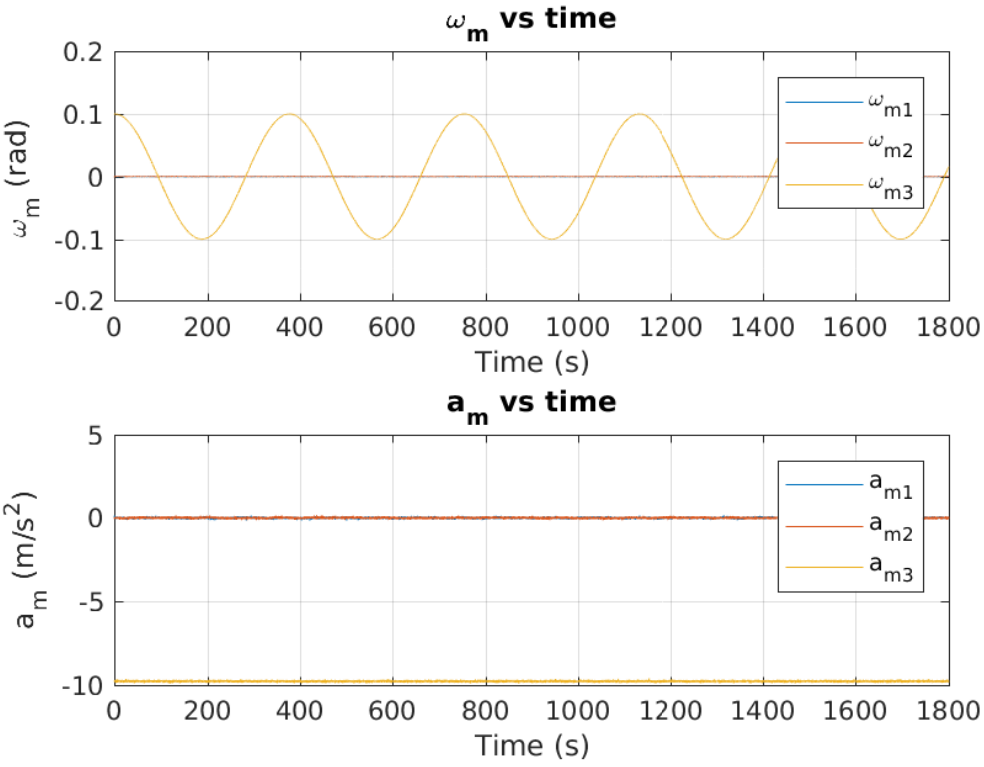

Figure 6.4: Sim2 KVH simulation measurements.

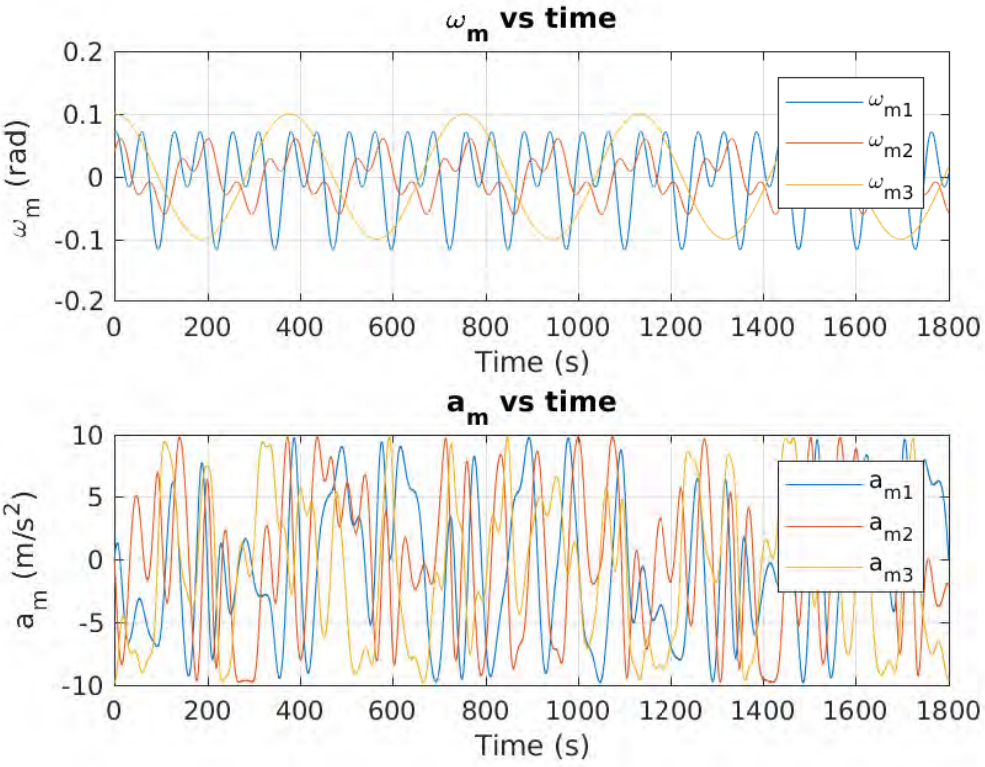

Figure 6.5: Sim3 KVH simulation measurements.

accelerometer estimated sensor biases, respectively. Lastly, Figures 6.14 and 6.15 report the **sim3** KVH vs PHINS attitude comparison and respective attitude errors, and Figures 6.16 and 6.17 report the **sim3** angular rate and accelerometer estimated sensor biases, respectively.

The **sim1** simulation results show that when the instrument is not excited via rotations, the gyrocompass system bias estimates and attitude estimates do not converge to their true values. This is consistent with adaptive identifiers which rely on persistence of excitation [42, 52]. In the **sim2** and **sim3** simulations, the attitude converges. Specifically, the simulations show (after the system has converged) the gyrocompass system to estimate roll and pitch within 0.1° and heading within 1° in RMSE. The **sim3** simulation converges faster than the **exp2** simulation due to the increased excitation experienced by the instrument in the **sim3** simulation.

In simulations with no sensor noise (not shown), we observed the attitude and bias errors estimations errors to converge to zero. In the three simulations reported herein, which include simulated sensor noise for the gyros and accelerometers, we see the attitude estimation errors converge to a neighborhood zero. As shown in the stability proof, the convergence of the bias estimation error is seen to depend upon the richness of the attitude excursions (persistence of excitation) the IMU experiences: In simulation **sim1**, where the IMU is motionless, the bias estimates do not converge to the true bias values. In simulation **sim2**, where the IMU experiences excursions in heading, with roll and pitch remaining zero, only four of the six components of the bias estimate converge to the neighborhood of the true values. In simulation **sim3**,

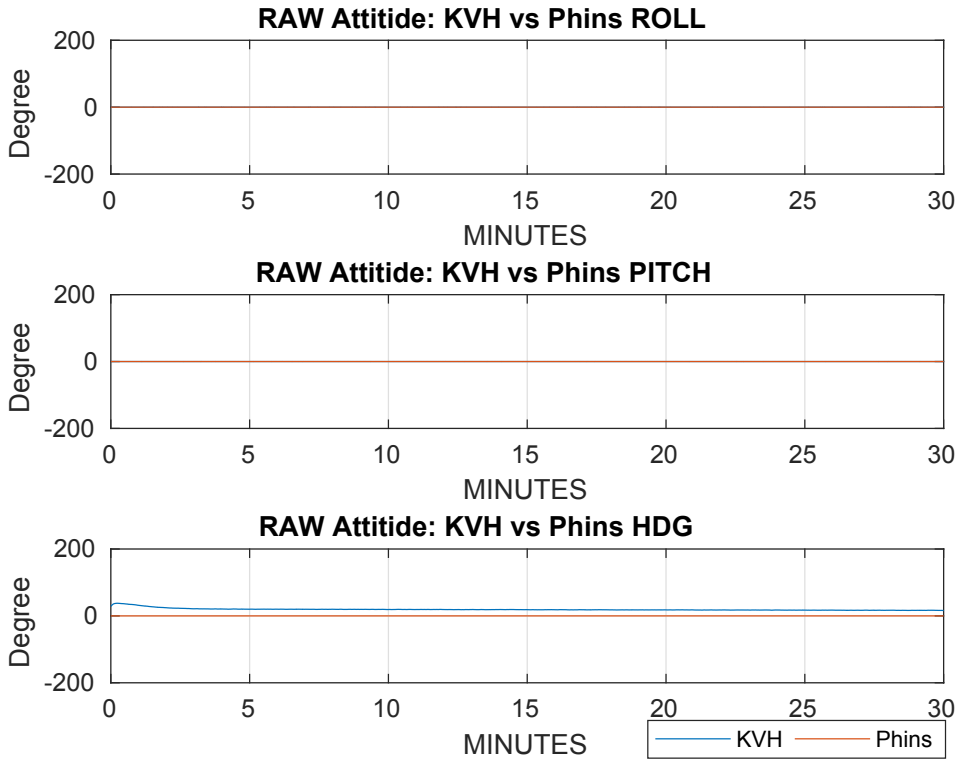

Figure 6.6: Comparison between **sim1** KVH simulation and PHINS ground truth attitude.

where the IMU experiences attitude excursions in 3-DOF, all six bias estimate terms converge to the "true" bias values.

It is important to note that the ${}^{i}\hat{w}_b(t)$ and ${}^{i}\hat{a}_b(t)$ update laws do not update bias components in the kernels of $\mathcal{J}\left({}^{i}a_e(t)\right)$ and $\mathcal{J}\left({}^{i}w_e(t)\right)$ respectively. Thus, in the case of **sim2** where the instrument only experiences changes in heading (the PE condition for asymptotic stability is not met when the instrument only experiences heading changes), the components of the biases along the gravity vector do not evolve. This configuration is common in oceanographic UVs which are commonly passively stable in roll and pitch. Since the convergence

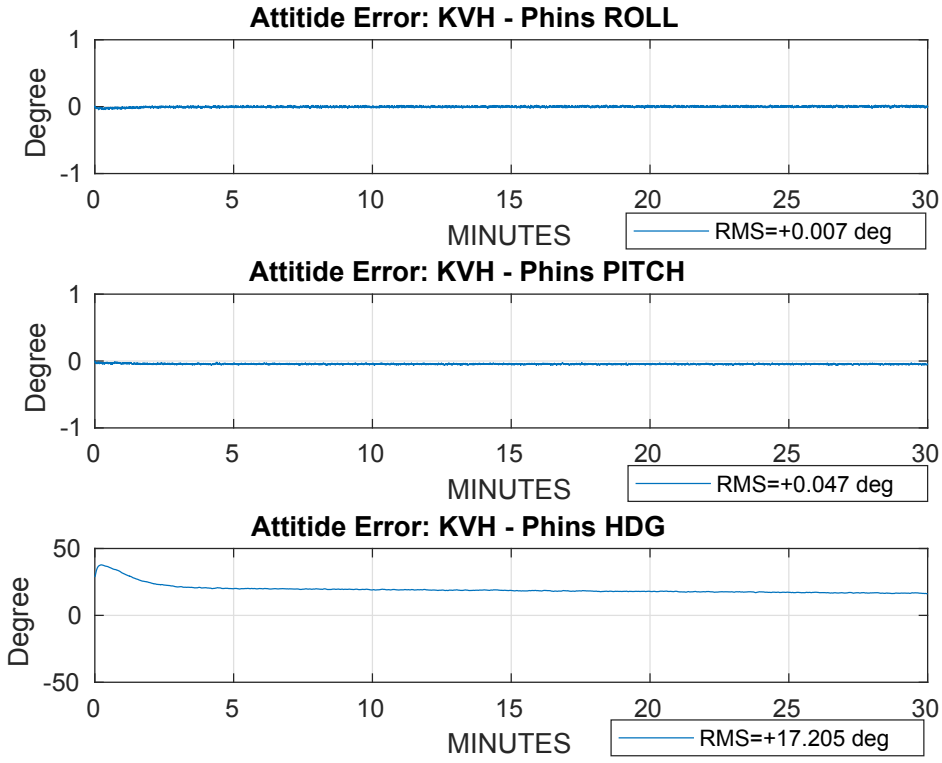

Figure 6.7: Sim1 KVH simulation attitude error.

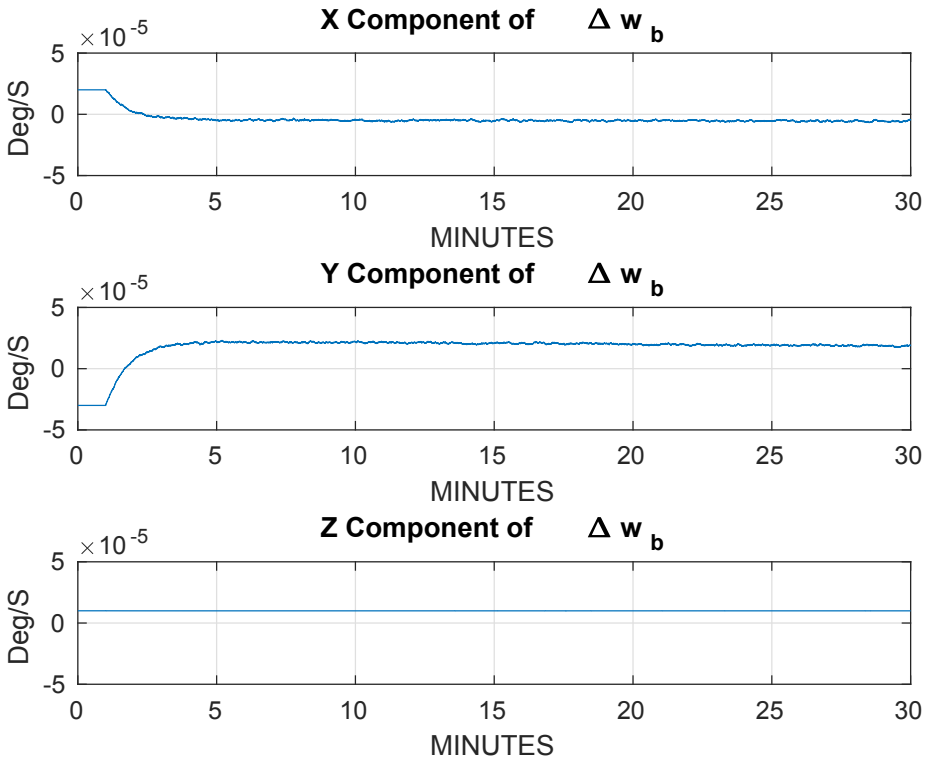

Figure 6.8: Sim1 estimated angular rate bias errors.

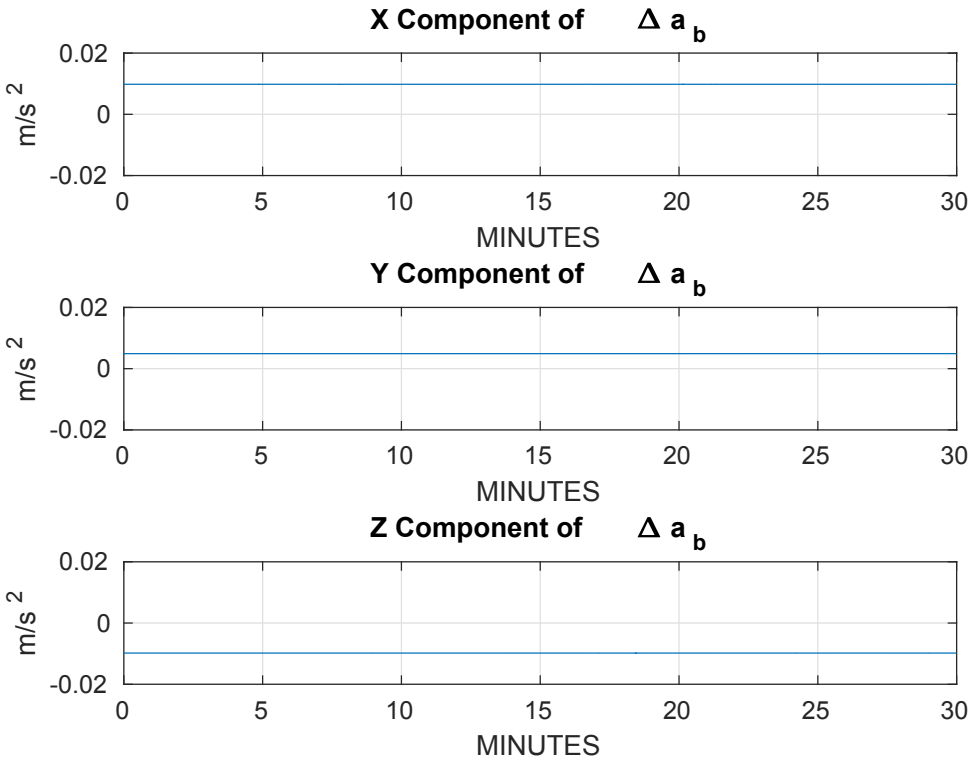

Figure 6.9: Sim1 estimated linear acceleration bias errors.

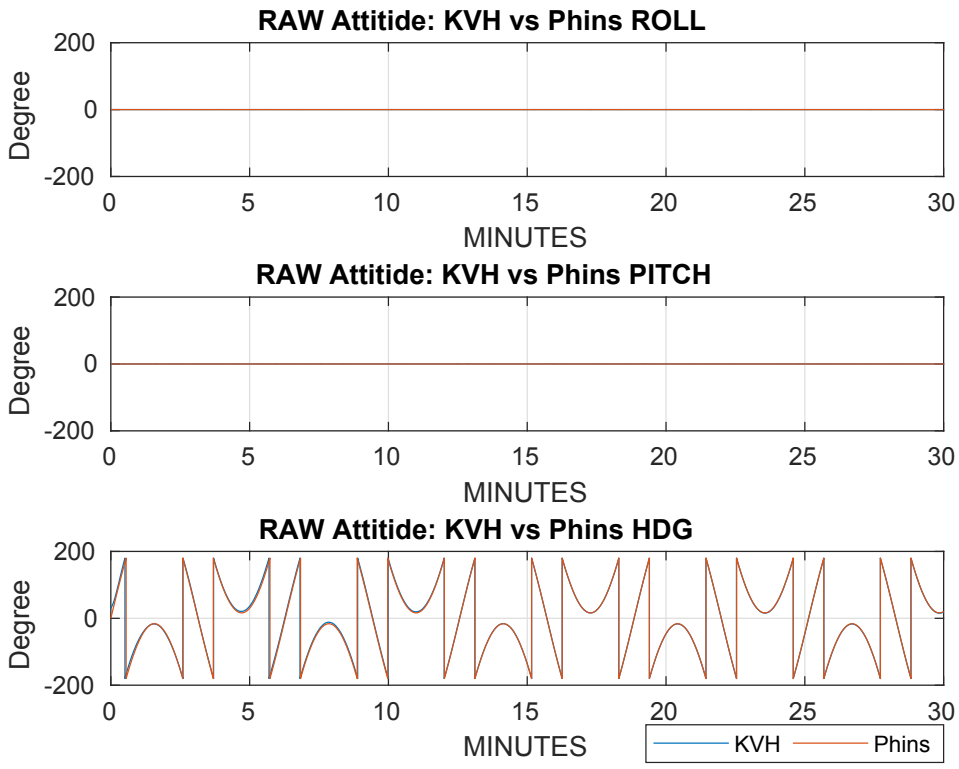

Figure 6.10: Comparison between **sim2** KVH simulation and PHINS ground truth attitude.

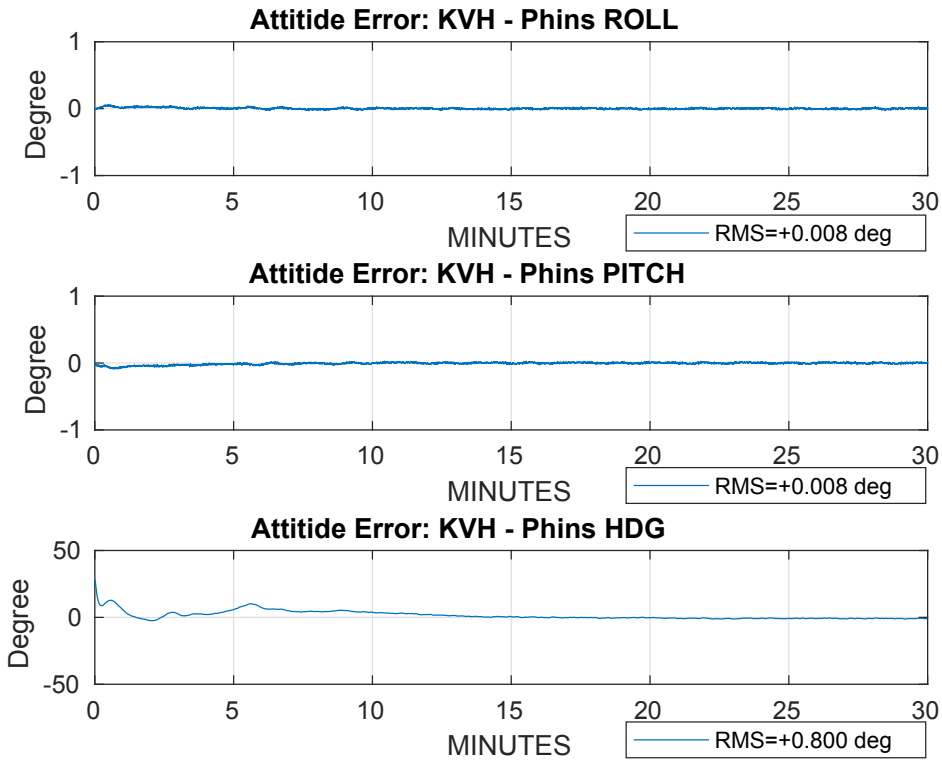

Figure 6.11: Sim2 KVH simulation attitude error.

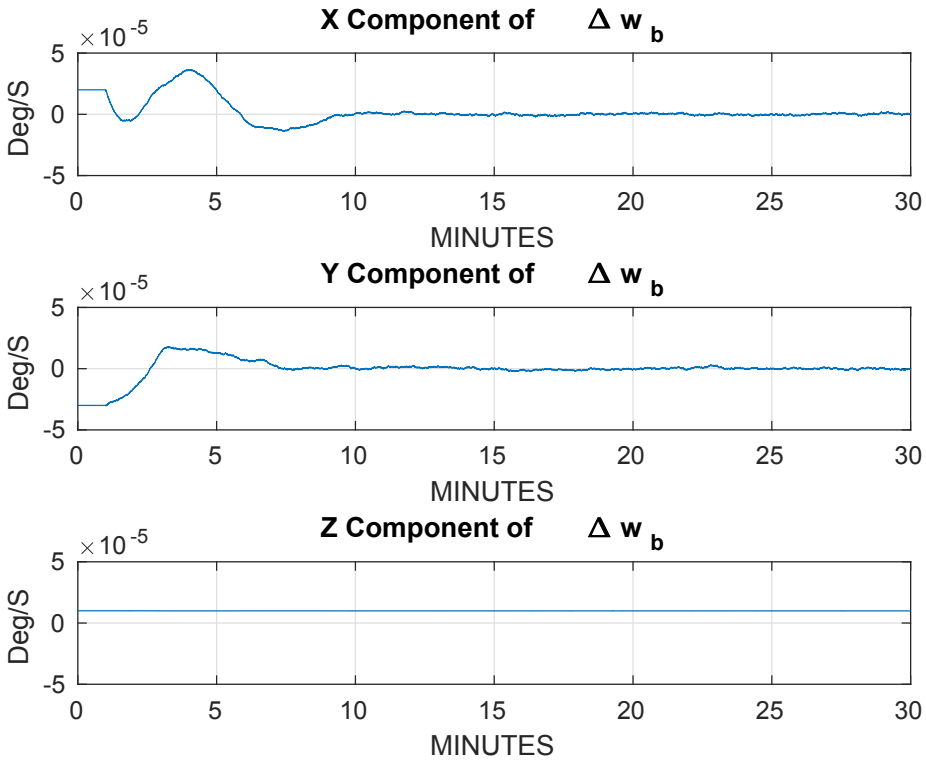

Figure 6.12: Sim2 estimated angular rate bias errors.

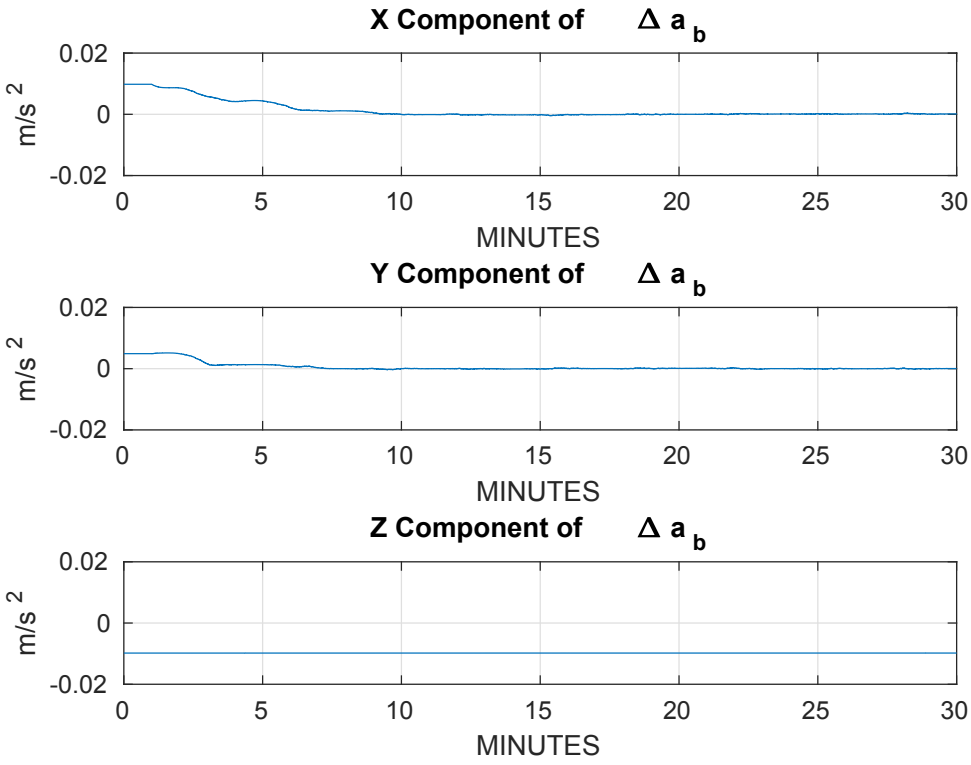

Figure 6.13: Sim2 estimated linear acceleration bias errors.

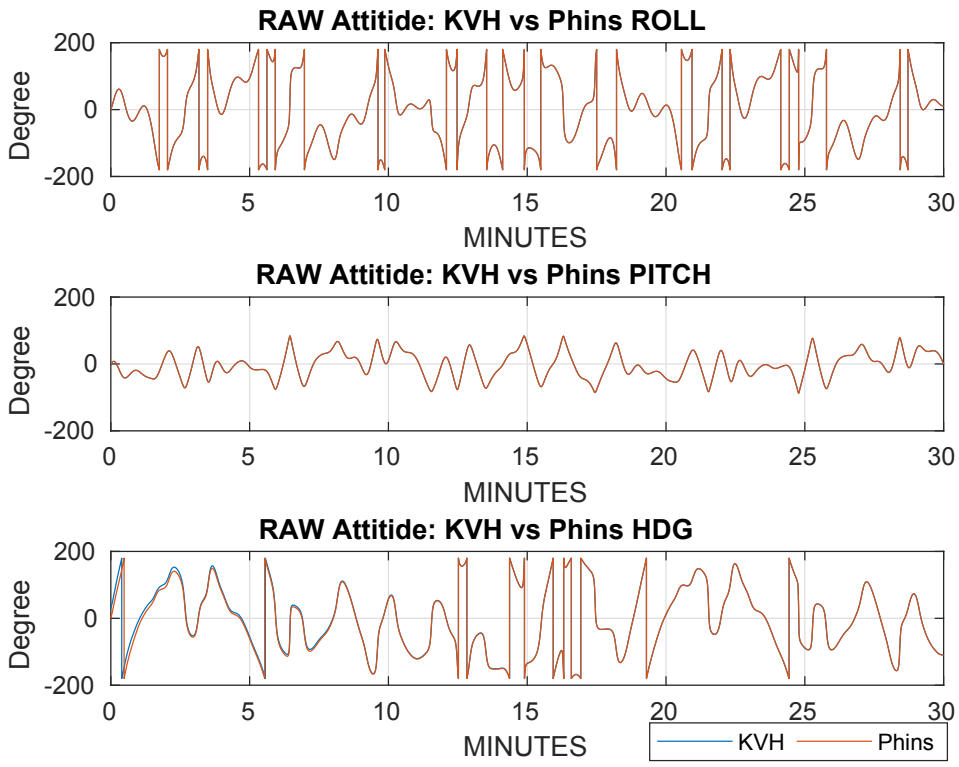

Figure 6.14: Comparison between **sim3** KVH simulation and PHINS ground truth attitude.

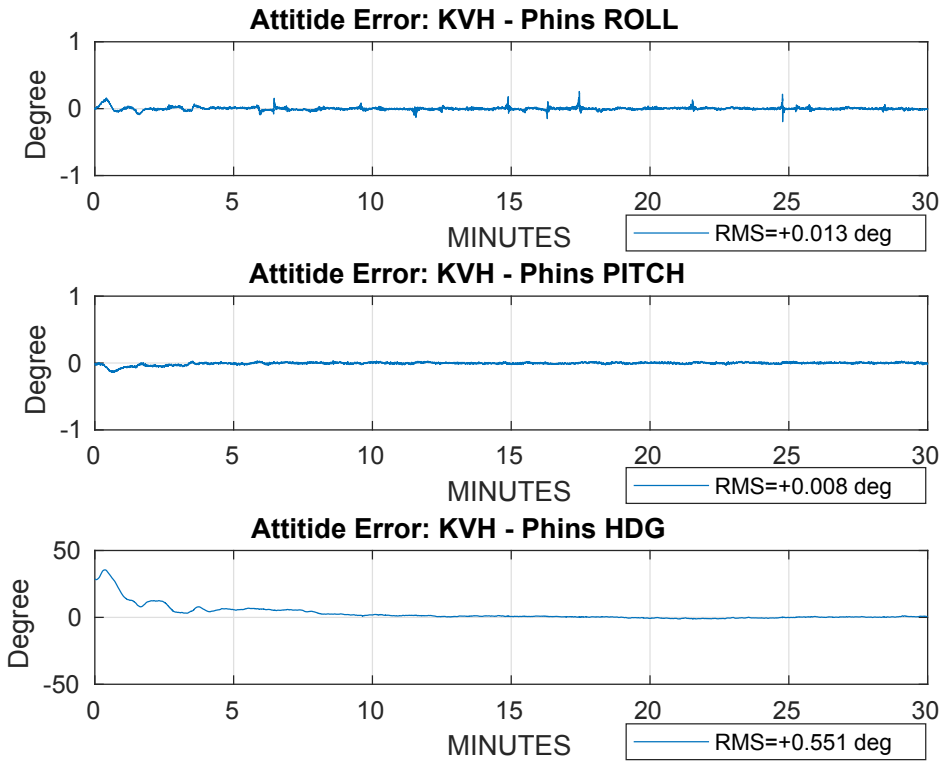

Figure 6.15: Sim3 KVH simulation attitude error.

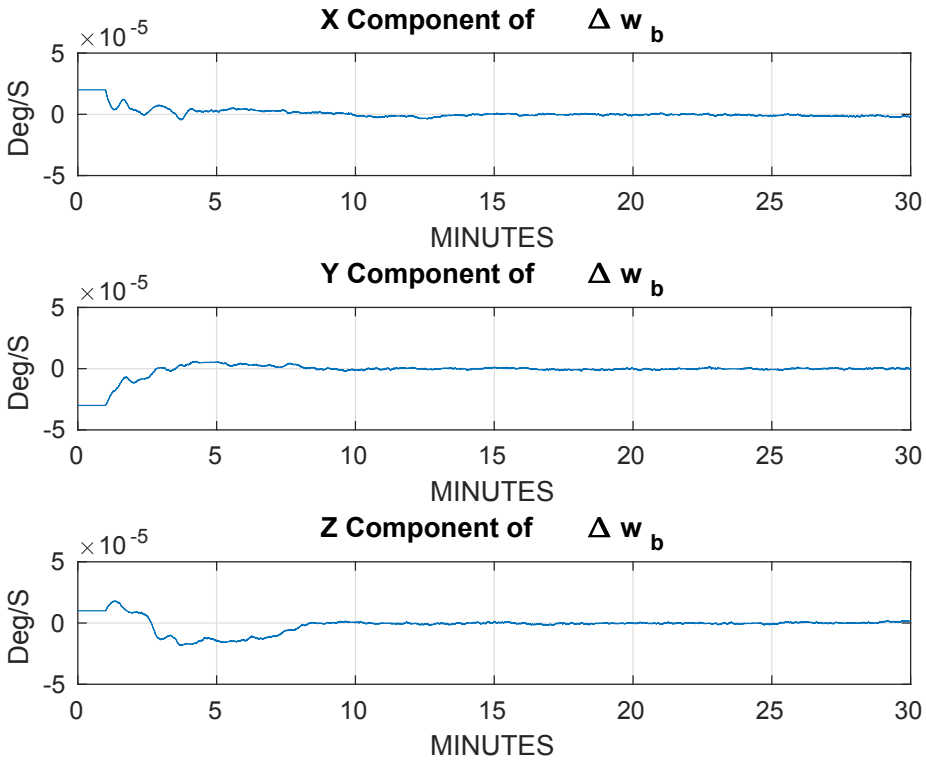

Figure 6.16: Sim3 estimated angular rate bias errors.

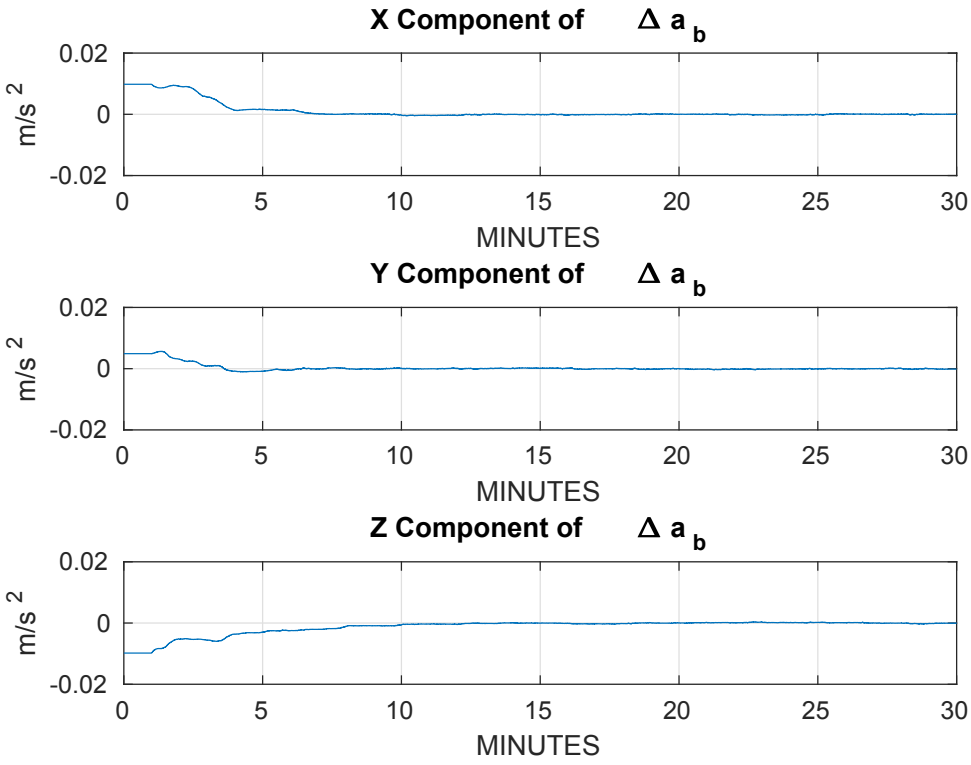

Figure 6.17: Sim3 estimated linear acceleration bias errors.

of ${}^{i}\hat{e}(t)$ is dependent on accurate estimation of the components of the biases in the North-East plane, the gyrocompass system is still able to converge to the correct attitude in **sim2** (only heading changes) since the components of the biases which affect the accuracy of the "East" estimate are properly estimated. Thus, in vehicles like oceanographic UVs which are passively stable in roll and pitch, it is not necessary to estimate accurately the components of the biases along the gravity vector in order to achieve accurate true-North attitude estimation.

6.8.4 Experimental Setup

The gyrocompass system is evaluated with a preliminary vehicle trial employing a comparatively low-cost ($\sim$ \$20k USD) FOG KVH 1775 IMU (KVH Industries, Inc., Middletown, RI, USA).

- The KVH 1775 FOG IMU was sampled at 5kHz.
- The KVH 1775 FOG IMU was aligned via a fixture to the ROV's iXBLUE PHINS INS (iXblue SAS, Cedex, France). The PHINS attitude is used as ground truth during our experimental evaluation of the attitude estimator.
- The **KVH** experiment was conducted at a latitude of 39.32°N (Baltimore, MD, USA).
- The ROV was commanded to execute smooth sinusoidal rotations ($\sim$ 720°) in heading while in closed-loop control. Figure 6.18 reports the IMU sensor measurements from the **KVH** experiment.

- The ROV experienced $\|{}^{i}a_v(t)\| \approx 0$ during the experiment.
- RMSE error was started to be calculated 20 minutes after filter starts.
- The initial condition, ${}^{N}_{i}\hat{R}(t)$, is chosen such that the initial heading is off by $\sim 40^{\circ}$. This is an initial heading that can be easily achieved with magnetic compasses. In the future, we plan to use the magnetometer in the KVH IMU for choosing the initial condition of the proposed gyrocompass system.
- The sensor biases estimates, ${}^{i}\hat{w}_b(t)$ and ${}^{i}\hat{a}(t)$, were all set to zero for their initial conditions.
- The instrument is mounted on the vehicle such that the instrument's x-axis is toward starboard, the y-axis is toward up, and the z-axis is toward stern of the vehicle.

6.8.5 Experimental Results

The attitude and sensor bias estimations and attitude errors for the vehicle trial are shown in Figures 6.19 - 6.22. Figure 6.21 reports the estimated angular rate sensor bias and Figure 6.22 reports the estimated accelerometer sensor bias. Figure 6.19 reports the comparison of the reported gyrocompass system's estimated attitude to that of the PHINS INS used as a "ground truth" during the laboratory experimental evaluation. Figure 6.20 reports the corresponding roll, pitch, and heading error. The results show that during this experimental evaluation of the gyrocompass system, the attitude estimate converged to the

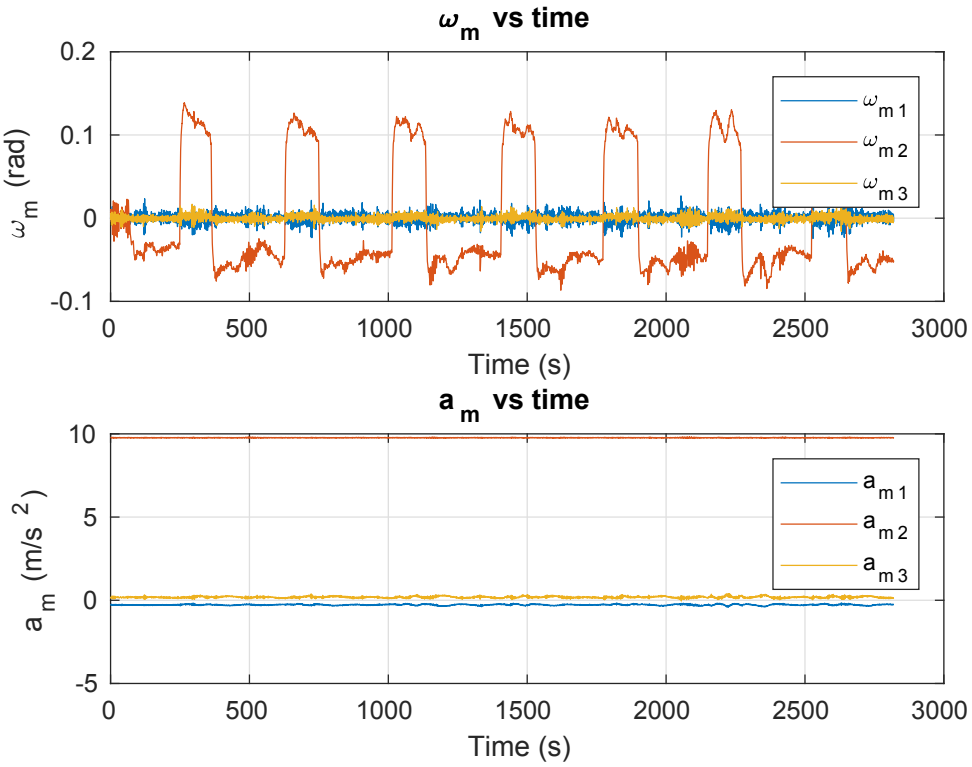

Figure 6.18: Vehicle trial KVH measurements.

true attitude. Roll and pitch converged to within 0.15° RMSE and true-North heading to within 1° RMSE of their true values.

In this experiment, where the vehicle and IMU principally experienced excursions in heading, with vehicle's roll and pitch remaining passively stable near zero, we see that the attitude estimation errors converge to a neighborhood zero and four of the six bias estimate terms converge to steady values. Thus the experimental conditions and experimental results of the bias and attitude estimator are seen to be similar to that observed in the simulation study **sim2**.

Note that as in **sim2**, the JHU ROV is a passively in roll and pitch and

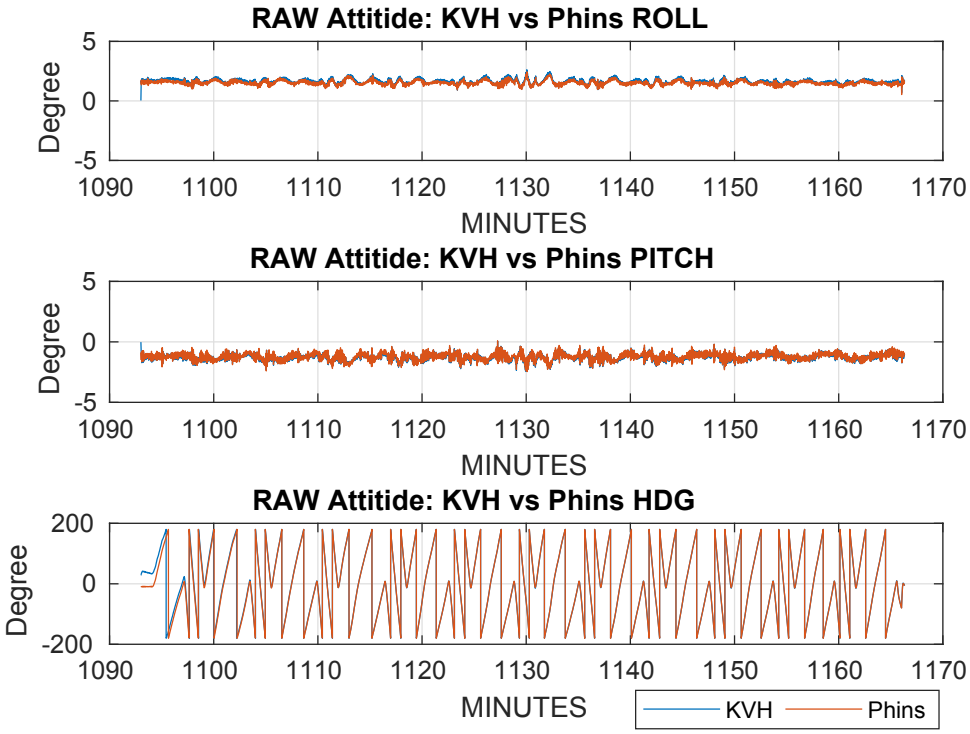

Figure 6.19: Comparison between the KVH experiment and PHINS ground truth attitude.

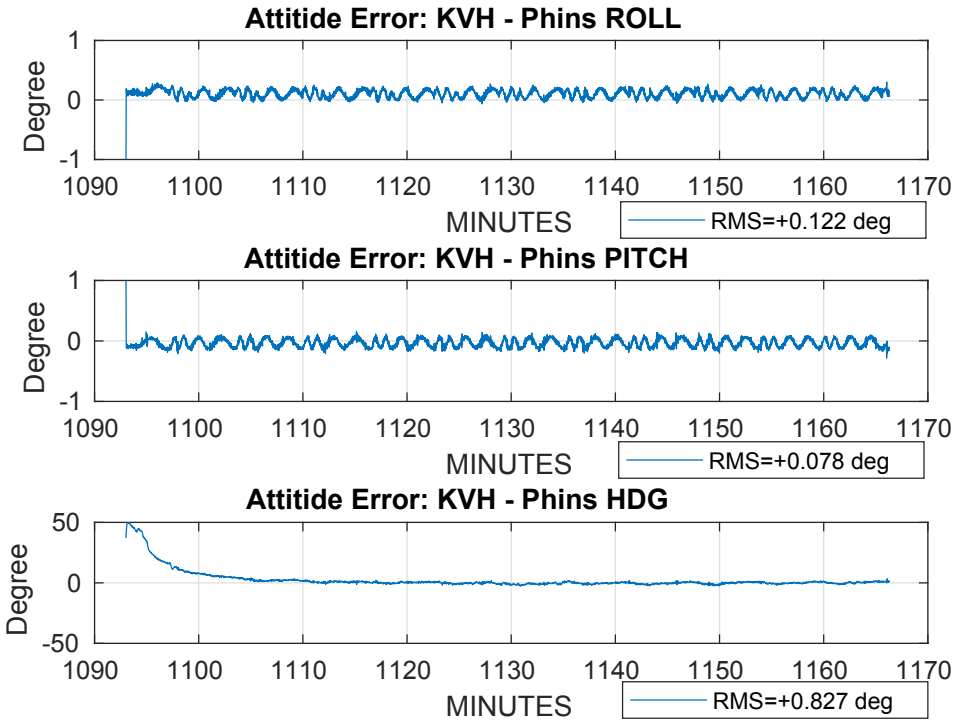

Figure 6.20: KVH experiment attitude error.

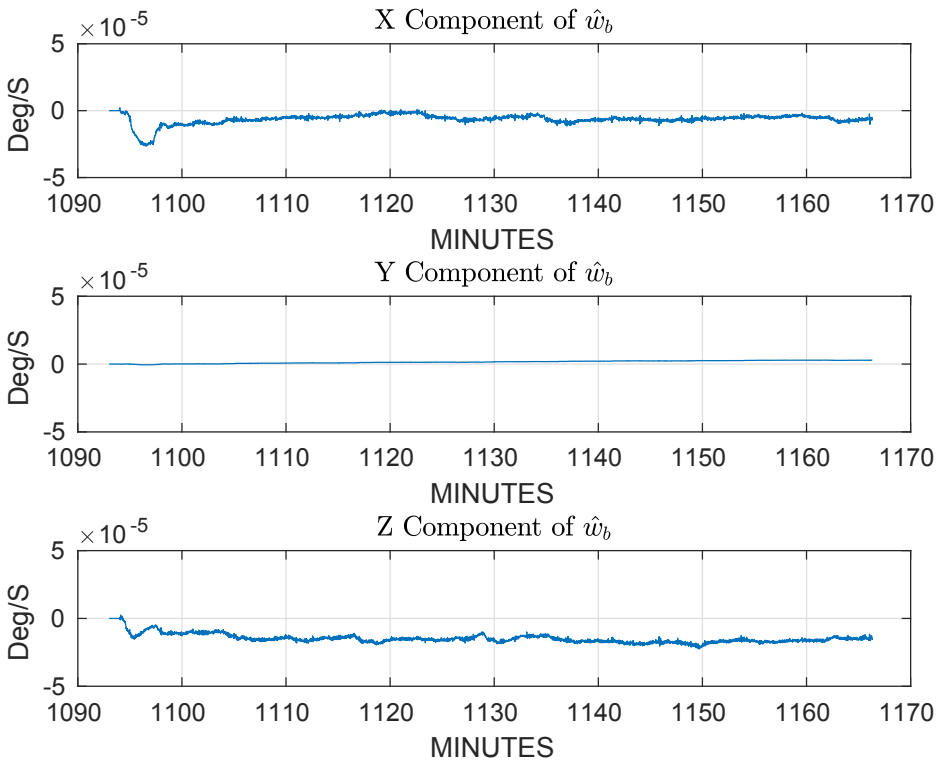

Figure 6.21: Estimated angular rate biases.

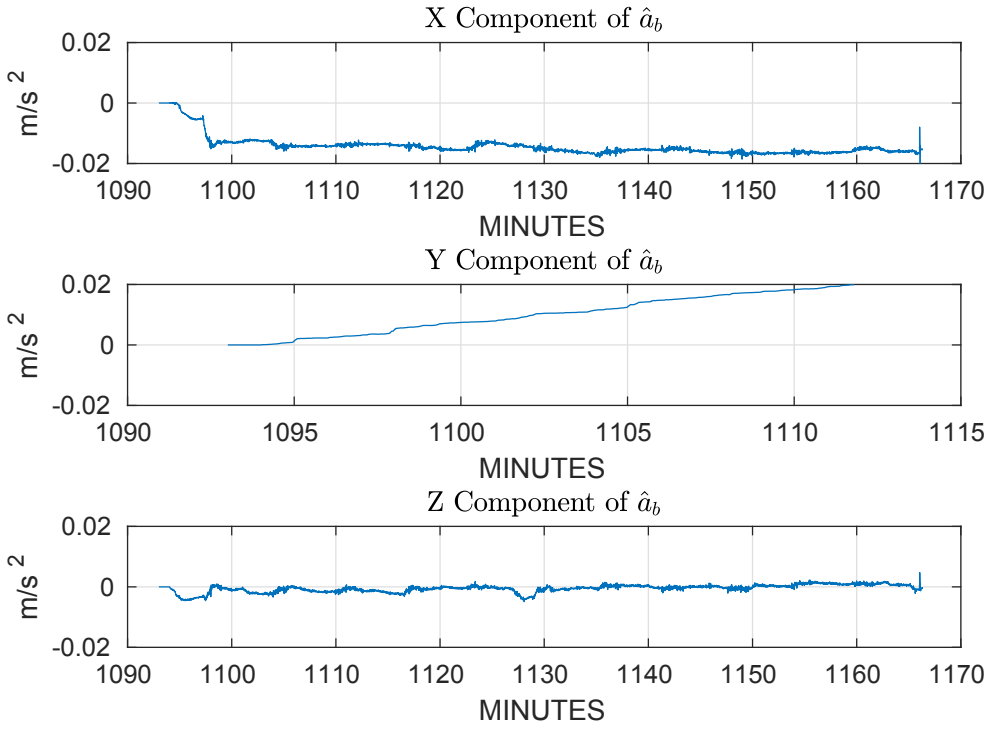

Figure 6.22: Estimated linear acceleration biases.

predominantly experiences attitude changes in heading only. Hence, while the components of the biases along the gravity vector (along the IMU's y-axis) do not converge to their correct values (See Figure 6.22), the true-North attitude does converge to the correct attitude.

In this preliminary result, the estimator took ∼15 minutes to converge to the correct true-North heading. Long convergence time is typical of true-North gyrocompass systems. For example, the iXBlue PHINS takes ∼10 minutes to achieve fine alignment [25]. We are currently investigating improvements to this sensor bias and East observer (e.g. adaptive gains) to improve its rate of convergence.

6.9 Conclusion

This chapter reports the derivation and stability analysis of an adaptive bias and East vector observer and an attitude observer for use in true-North gyrocompass systems. Preliminary simulations and a full-scale vehicle experiment using a commercially available low-cost FOG IMU are reported.

The preliminary simulation and vehicle trial suggest, for the case of a gyrocompass system that experiences rotations, the convergence of the reported gyrocompass system to the true attitude *without* using magnetometers. The vehicle trial shows roll and pitch converge to within 0.15° RMSE and true-North heading to within 1° RMSE of their true values.

In future studies, the author hopes to improve the time of convergence, increase the accuracy of the gyrocompass system, extend the system to non-trivial vehicle accelerations, and conduct extensive full-scale experimental

vehicle trials both in the lab and in the field.

Intended to be blank.

Chapter 7

Conclusion

7.1 Thesis Summary

This thesis reports algorithms for the estimation of inertial measurement unit (IMU) sensor biases for use in the calibration of attitude and heading reference systems (AHRSs). AHRSs are divided into two classes of AHRSs – one for those systems which estimate true-North heading and one for those systems which estimate magnetic-North heading. Chapters 3 - 5 present novel algorithms for calibrating and compensating for sensor biases arising in magnetic-North heading AHRSs. Chapter 6 reports nonlinear adaptive observers for IMU sensor bias estimation and attitude estimation directly on $SO(3)$ for use in a true-North gyrocompass AHRS. Stability or observability analysis is included for every reported algorithm.

Chapter 3 reports the derivation and stability proof of an adaptive observer for sensor biases (magnetometer hard-iron bias only, no soft-iron sensor bias) in 9-degrees of freedom (DOF) IMUs. Numerical simulations and an experimental evaluation are presented. Although only stability of the adaptive

observer is analytically shown, the simulations and vehicle trial suggest, for the case of a rotating IMU, the asymptotic convergence of the sensor biases to their true values.

Chapter 4 reports a novel magnetometer sensor bias adaptive observer for the class of vehicles which are passively stable in roll and pitch. The chapter reports an method for on-line, real-time estimation of hard-iron and soft-iron magnetometer biases in 2-axis magnetometers for use in AHRSs. The observer uses only magnetometer sensor signals, does not require knowledge of the instrument attitude, and is shown to be globally stable. When the measured magnetometer is persistently exciting (PE), the observer is shown to be globally asymptotically stable where the estimated parameters converge to their true values. A simulation study and full-scale vehicle experiment with comparison to a least squares method are reported and suggest that the observer can be utilized to provide accurate magnetometer bias compensation for AHRS. In addition to the 2-axis adaptive observer, a 3-axis extension of the observer is reported. The 3-axis observer however, is shown to suffer from the same drawbacks of many previously reported least-squares methods. Large angular rotations and full coverage of the sphere are required in order for the 3-axis observer to be used for accurate magnetometer sensor bias estimation. The 3-axis adaptive observer is not suitable for use on vehicles which are passively stable in roll and pitch, which are the focus of this chapter.

Chapter 5 reports a novel method for online, real-time estimation of hard-iron and soft-iron magnetometer biases and angular rate sensor biases in IMUs for use in AHRSs. By utilizing angular rate sensor measurements, smaller

angular rotations of the instrument (in comparison to previously reported methods for magnetometer calibration like the 3-axis method presented in Chapter 4 and the TWOSTEP method) are required for accurate compensation of magnetometer and angular velocity sensor biases. Since the proposed estimator works with smaller changes in roll and pitch than previously reported methods, it can be implemented on real full-scale remotely operated vehicles (ROVs), which are commonly passively stable in roll and pitch, to provide online estimates of the full 3-axis magnetometer sensor biases. Numerical simulations, laboratory experiments, and field trials show that the proposed MAVBE magnetometer calibration method provides improved performance over common methods like the TWOSTEP method and the OceanServer Iver3 AUV commercial solution. The ability of the proposed MAVBE method to accurately estimate magnetometer biases when there is limited excitation of the magnetometer signal illustrates the advantage of the MAVBE method over common calibration methods like the TWOSTEP and ellipsoid fitting methods which fail when there is low coverage of the magnetometer on the sphere.

Chapter 6 reports the derivation and stability analysis of an adaptive bias and East vector observer and an attitude observer for use in a true-North gyrocompass system. Preliminary simulations and a full-scale vehicle experiment using a commercially available low-cost FOG IMU are reported. The preliminary simulation and vehicle trial suggest, for the case of a gyrocompass system that experiences rotations, the convergence of the reported gyrocompass system to the true attitude *without* using magnetometers.

7.2 Future Work

In future work, the author hopes to improve the convergence times of the reported observers and conduct more extensive field testing.

- For the adaptive observer reported in Chapter 3, future work includes improving the time of convergence, extending the proof to analytically show asymptotic stability of the sensor biases, and to do thorough vehicle trials both in the lab and in the field.

- For the magnetometer soft-iron and hard-iron adaptive observer presented in Chapter 4, the author hopes to develop a coarse and fine alignment protocol to allow for fast convergence and accurate bias estimation, employ the observer in field trials, and provide a sensitivity analysis on how roll and pitch affect the sensor bias estimates.

- Future work on the Chapter 5 reported MAVBE calibration method includes improving convergence time of the estimator by developing coarse and fine alignment protocols, comparison of the MAVBE calibrated AHRS with a "ground truth" system like a high-end inertial navigation system (INS), and conducting extensive field testing. Different values for the process covariance matrix, Q, could be chosen during the coarse and fine alignment to enable both a fast convergence of the sensor biases and a smooth final steady state.

- In future studies, the author hopes to improve the time of convergence and increase the accuracy of the Chapter 6 gyrocompass system, extend

the system to accommodate for nontrivial vehicle accelerations, and conduct extensive full-scale experimental vehicle trials both in the lab and in the field. The author would also like to employ the algorithm on KVH IMU data logged during dives with the Sentry autonomous underwater vehicle (AUV) on the Bowditch Seamont in August 2018.

Intended to be blank.

Appendix A

Johns Hopkins University (JHU) Hydrodynamic Test Facility (HTF)

The Johns Hopkins University (JHU) hydrodynamic test facility (HTF) [29] contains a test tank, a remotely operated vehicle (ROV), and autonomous underwater vehicle (AUV) for the design, development, and testing of oceanographic systems.

A.1 JHU HTF Test Tank

The JHU HTF contains an indoor fresh water tank measuring 7.5 meters in diameter by 4 meters deep with a capacity of 174,000 liters. The facility has two 1-ton overhead gantry cranes for working over the tank and in the lab.

A.2 JHU ROV

The JHU ROV is a fully actuated (six-DOF) vehicle with six 1.5 kW DC brushless electric thrusters and employs a suite of sensors commonly employed on deep submergence underwater vehicles. Figure A.2 shows the test facility and

Figure A.1: The Johns Hopkins University (JHU) hydrodynamic test facility (HTF) test tank (Image credit: Louis Whitcomb, JHU).

the ROV operating in the test tank. The ROV is instrumented with a high-end INS, the iXBlue PHINS III (iXBlue SAS, Cedex, France) [24, 25], a MicroStrain 3DM-GX5-25 IMU [39], a KVH 1775 (KVH Industries, Inc., Middletown, RI, USA) FOG IMU [32], a 1200 kHz bottom-lock Doppler sonar (RD Instruments, San Diego, CA), and a 8CDP010-1 Digiquartz depth sensor (Paroscientific Inc., Redmond, WA) [49].

A.3 JHU Iver3 AUV

The facility contains the JHU Iver3 AUV (L3 OceanServer, Fall River, MA, USA) [45]. The AUV is an under-actuated AUV equipped with a 600 kHz Phased Array RDI Explorer DVL [67], a MicroStrain 3DM-GX5-25 [39] IMU, and the a OceanServer OS5000 [44] magnetic compass. Figure A.3 shows the

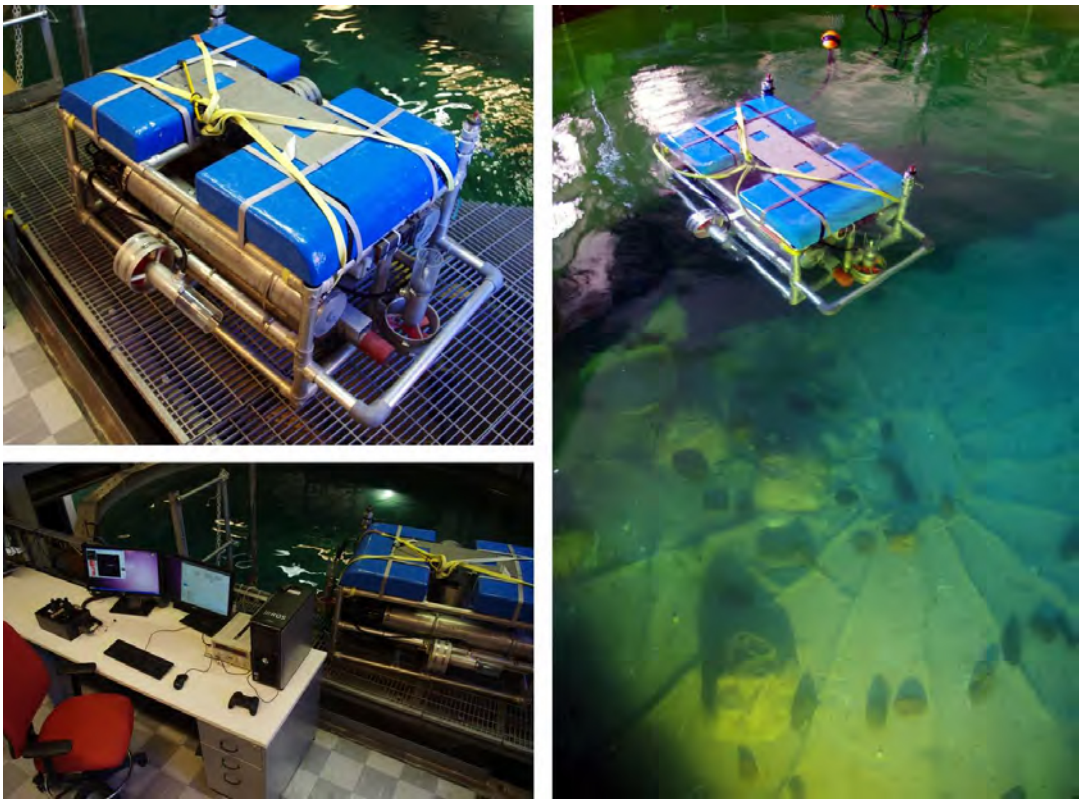

Figure A.2: The Johns Hopkins University (JHU) hydrodynamic test facility (HTF) and the fully actuated JHU ROV (Image credit: Louis Whitcomb, JHU).

Table A.1: JHU ROV Measurement sources, resolutions, and accuracies [39, 24, 25, 32, 49].

State	Source	Update Rate	Measurement Resolution
Roll, Pitch, Hdg.	IXBlue PHINS III	$1 - 100$ Hz	0.01° roll and pitch, 0.05° / cos(latitude)
Linear Acceleration	Microstrain 3DM-GX5-25	$1 - 1000$ Hz	0.0075 m/s^2 Std Dev
Angular Velocity	Microstrain 3DM-GX5-25	$1 - 1000$ Hz	0.00025 rad/s Std Dev
Magnetic Field	Microstrain 3DM-GX5-25	$1 - 100$ Hz	0.002 gauss Std Dev
Linear Acceleration	KVH 1775	$1 - 5000$ Hz	0.0037 m/s^2 Std Dev
Angular Velocity	KVH 1775	$1 - 5000$ Hz	6.32×10^{-3} rad/s Std Dev
Magnetic Field	KVH 1775	$1 - 500$ Hz	0.002 gauss Std Dev
Translational Velocity	1200 kHz RDI DVL	6 Hz	$>$ 0.003 m/s Std Dev
Pressure	Digiquartz Depth Sensor	7 Hz	Resolution 2 parts-per-million $>$ 0.75% as calculated

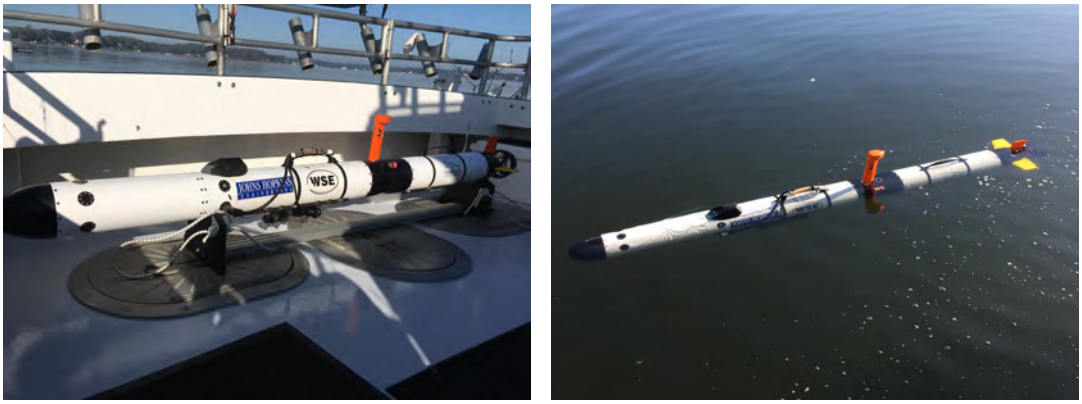

(a) (b)

Figure A.3: Field trials were conducted with the Johns Hopkins University (JHU) Iver3 autonomous underwater vehicle (AUV) in the Chesapeake Bay, MD, USA. The JHU Iver3 has a full suite of navigation sensors, including a Doppler velocity log (DVL) and several inertial measurement units (IMUs) (Image credit: Paul Stankiewicz, JHU).

JHU Iver3 AUV during the vehicle tests. Table A.2 lists the sensors on board the JHU Iver3.

Table A.2: JHU Iver3 AUV Measurement sources, resolutions, and accuracies [39, 45, 44, 67].

State	Source	Update Rate	Measurement Resolution
Roll, Pitch, Hdg.	OceanServer OS5000 Compass Unit	1 Hz	$< 0.5^\circ$ Heading RMSE When Level 1° Heading RMSE When $< \pm 30^\circ$ Tilt
Linear Acceleration	Microstrain 3DM-GX5-25	20 Hz	0.0075 m/s^2 Std Dev
Angular Velocity	Microstrain 3DM-GX5-25	20 Hz	0.00025 rad/s Std Dev
Magnetic Field	Microstrain 3DM-GX5-25	20 Hz	0.002 gauss Std Dev
Translational Velocity	600 kHz RDI Explorer DVL	4 Hz	0.01 m/s Std Dev

Bibliography

[1] R. Alonso and M. D. Shuster, "TWOSTEP: A fast robust algorithm for attitude-independent magnetometer-bias determination," *Journal of the Astronautical Sciences*, vol. 50, no. 4, pp. 433–452, 2002.

[2] R. Alonso and M. D. Shuster, "Complete linear attitude-independent magnetometer calibration," *Journal of the Astronautical Sciences*, vol. 50, no. 4, pp. 477–490, 2002.

[3] N. Ammann, A. Derksen, and C. Heck, "A novel magnetometer-accelerometer calibration based on a least squares approach," in *2015 International Conference on Unmanned Aircraft Systems (ICUAS)*, June 2015, pp. 577–585.

[4] P. Batista, C. Silvestre, and P. Oliveira, "Attitude observer on the special orthogonal group with Earth velocity estimation," *Systems & Control Letters*, vol. 126, pp. 33–39, 2019.

[5] G. Besançon, "Remarks on nonlinear adaptive observer design ," *Systems & Control Letters*, vol. 41, no. 4, pp. 271 – 280, 2000.

[6] A. Bronner, M. Munschy, D. Sauter, J. Carlut, R. Searle, and A. Maineult, "Deep-tow 3C magnetic measurement: Solutions for calibration and interpretation," *GEOPHYSICS*, vol. 78, no. 3, pp. J15–J23, 2013.

[7] G. S. Chirikjian, *Stochastic Models, Information Theory, and Lie Groups, Volume 2: Analytic Methods and Modern Applications*. Birkhäuser Basel, 2012, vol. 2.

[8] D. Clegg and M. Peterson, "User Operational Evaluation System of Unmanned Underwater Vehicles for very Shallow Water Mine Countermeasures," in *OCEANS 2003*, vol. 3, September 2003, pp. 1417–1423.

[9] T. R. Clem, D. D. Sternlicht, J. E. Fernandez, J. L. Prater, R. Holtzapple, R. P. Gibson, J. P. Klose, and T. M. Marston, "Demonstration of advanced sensors for underwater unexploded ordnance (UXO) detection," in *OCEANS 2012*, October 2012, pp. 1–4.

[10] R. Costanzi, F. Fanelli, N. Monni, A. Ridolfi, and B. Allotta, "An Attitude Estimation Algorithm for Mobile Robots Under Unknown Magnetic Disturbances," *IEEE/ASME Transactions on Mechatronics*, vol. 21, no. 4, pp. 1900–1911, August 2016.

[11] J. L. Crassidis, K.-L. Lai, and R. R. Harman, "Real-time attitude-independent three-axis magnetometer calibration," *Journal of Guidance, Control, and Dynamics*, vol. 28, no. 1, pp. 115–120, 2005.

[12] J. L. Crassidis, F. L. Markley, and Y. Cheng, "Survey of nonlinear attitude estimation methods," *Journal of guidance, control, and dynamics*, vol. 30, no. 1, pp. 12–28, 2007.

[13] Dinale, Justin P., "Magnetic Test Facility - Sensor and Coil Calibrations," Master's thesis, University of Adelaide, School of Electrical and Electronic Engineering, 2013.

[14] M. Fackler, Ed., *Six Years After Fukushima, Robots Finally Find Reactors' Melted Uranium Fuel*, The New York Times, November 2017.

[15] J. Fang, H. Sun, J. Cao, X. Zhang, and Y. Tao, "A Novel Calibration Method of Magnetic Compass Based on Ellipsoid Fitting," *IEEE Transactions on Instrumentation and Measurement*, vol. 60, no. 6, pp. 2053–2061, June 2011.

[16] C. C. Foster and G. H. Elkaim, "Extension of a two-step calibration methodology to include nonorthogonal sensor axes," *IEEE Transactions on Aerospace and Electronic Systems*, vol. 44, no. 3, pp. 1070–1078, July 2008.

[17] B. Gambhir, "Determination of magnetometer biases using module RESIDG," *Computer Sciences Corporation, Report*, no. 3000-32700, p. 01, 1975.

[18] M. George and S. Sukkarieh, "Tightly coupled INS/GPS with bias estimation for UAV applications," in *Proceedings of Australiasian Conference on Robotics and Automation (ACRA)*, 2005.

[19] P. Guo, H. Qiu, Y. Yang, and Z. Ren, "The soft iron and hard iron calibration method using extended Kalman filter for attitude and heading reference system," in *Position, Location and Navigation Symposium, 2008 IEEE/ION*. IEEE, 2008, pp. 1167–1174.

[20] T. Hamel and R. Mahony, "Attitude estimation on SO(3) based on direct inertial measurements," in *2006 IEEE International Conference on Robotics and Automation (ICRA)*. IEEE, 2006, pp. 2170–2175.

[21] K. Han, H. Han, Z. Wang, and F. Xu, "Extended Kalman Filter-Based Gyroscope-Aided Magnetometer Calibration for Consumer Electronic Devices," *IEEE Sensors Journal*, vol. 17, no. 1, pp. 63–71, January 2017.

[22] C. Honsho, T. Ura, and K. Kim, "Deep-sea magnetic vector anomalies over the Hakurei hydrothermal field and the Bayonnaise knoll caldera, Izu-Ogasawara arc, Japan," *Journal of Geophysical Research: Solid Earth*, vol. 118, no. 10, pp. 5147–5164, 2013.

[23] T. P. Hughes, *Elmer Sperry: Inventor and Engineer*, Softshell Books ed. The Johns Hopkins Press, 1993.

[24] iXblue SAS, Cedex, France, "iXSEA PHINS INS datasheet," 2008.

[25] IXSEA, *PHINS III User Guide*, MU-PHINSIII-006 B ed., IXSEA, December 2008.

[26] S. Kawatsuma, M. Fukushima, and T. Okada, "Emergency response by robots to Fukushima-Daiichi accident: summary and lessons learned," *Industrial Robot*, vol. 39, no. 5, pp. 428–435, 2012.

[27] H. K. Khalil, *Noninear Systems; 3rd ed.* Upper Saddle River, NJ: Prentice-Hall, 2002.

[28] J. C. Kinsey and L. L. Whitcomb, "Adaptive Identification on the Group of Rigid-Body Rotations and its Application to Underwater Vehicle Navigation," *IEEE Transactions on Robotics*, vol. 23, no. 1, pp. 124–136, Febuary 2007.

[29] J. Kinsey, D. Smallwood, and L. Whitcomb, "A new hydrodynamics test facility for UUV dynamics and control research," in *2003 IEEE OCEANS*, vol. 1, September 2003, pp. 356 – 361.

[30] J. C. Kinsey and L. L. Whitcomb, "Preliminary field experience with the DVLNAV integrated navigation system for oceanographic submersibles," *Control Engineering Practice*, vol. 12, no. 12, pp. 1541 – 1549, 2004.

[31] M. Kok, J. D. Hol, T. B. Schön, F. Gustafsson, and H. Luinge, "Calibration of a magnetometer in combination with inertial sensors," in *Information Fusion (FUSION), 2012 15th International Conference on*. IEEE, 2012, pp. 787–793.

[32] KVH Industries, Inc., Middletown, RI, USA, "KVH 1775 IMU datasheet," 2015.

[33] X. Li and Z. Li, "A new calibration method for tri-axial field sensors in strap-down navigation systems," *Measurement Science and technology*, vol. 23, no. 10, p. 105105, 2012.

[34] W. M. Macek and D. Davis Jr, "Rotation Rate Sensing with Traveling-Wave Ring Lasers," *Applied Physics Letters*, vol. 2, no. 3, pp. 67–68, 1963.

[35] R. Mahony, T. Hamel, and J. M. Pflimlin, "Nonlinear Complementary Filters on the Special Orthogonal Group," *IEEE Transactions on Automatic Control*, vol. 53, no. 5, pp. 1203–1218, June 2008.

[36] A. Martinelli, "Vision and IMU Data Fusion: Closed-Form Solutions for Attitude, Speed, Absolute Scale, and Bias Determination," *IEEE Transactions on Robotics*, vol. 28, no. 1, pp. 44–60, Febuary 2012.

[37] N. Metni, J. M. Pflimlin, T. Hamel, and P. Souéres, "Attitude and gyro bias estimation for a flying UAV," in *2005 IEEE/RSJ International Conference on Intelligent Robots and Systems (IROS)*, August 2005, pp. 1114–1120.

[38] N. Metni, J.-M. Pflimlin, T. Hamel, and P. Souéres, "Attitude and gyro bias estimation for a VTOL UAV," *Control Engineering Practice*, vol. 14, no. 12, pp. 1511 – 1520, 2006.

[39] Microstrain Inc., "3DM-GX3-25 Miniature Attitude Heading Reference System datasheet," Microstrain Inc., Williston, VT, Tech. Rep. P/N 8400-0033 rev. 002, 2012.

[40] R. R. Murphy, "A decade of rescue robots," in *2012 IEEE/RSJ International Conference on Intelligent Robots and Systems*, October 2012, pp. 5448–5449.

[41] R. M. Murray, Z. Li, and S. S. Sastry, *A Mathematical Introduction to Robotic Manipulation*. Boca Raton: CRC Press, 1994.

[42] K. S. Narendra and A. M. Annaswamy, *Stable adaptive systems*. Prentice-Hall Inc., 1989.

[43] NCEI Geomagnetic Modeling Team and British Geological Survey, *World Magnetic Model 2020*. National Centers for Environmental Information, 2019.

[44] OceanServer Technology, Inc., *Digital Compass Users Guide, OS5000 Series*, Rev. 5.0 ed., OceanServer, April 2015.

[45] OceanServer Technology, Inc., *AUV Operating Guide*, Rev. 5.0 ed., OceanServer, July 2016.

[46] H. S. Ousaloo, G. Sharifi, J. Mahdian, and M. T. Nodeh, "Complete Calibration of Three-Axis Strapdown Magnetometer in Mounting Frame," *IEEE Sensors Journal*, vol. 17, no. 23, pp. 7886–7893, December 2017.

[47] G. E. Packard, A. Kukulya, T. Austin, M. Dennett, R. Littlefield, G. Packard, M. Purcell, R. Stokey, and G. Skomal, "Continuous autonomous tracking and imaging of white sharks and basking sharks using a REMUS-100 AUV," in *2013 OCEANS - San Diego*, September 2013, pp. 1–5.

[48] K. Papafotis and P. P. Sotiriadis, "Computationally Efficient Calibration Algorithm for Three-Axis Accelerometer and Magnetometer," in *2019 8th International Conference on Modern Circuits and Systems Technologies (MOCAST)*, May 2019, pp. 1–4.

[49] Paroscientific Inc., Redmond, WA, "Submersible Depth Sensors - Series 8000," 2005.

[50] J. M. Pflimlin, T. Hamel, and P. SouÃĺres, "Nonlinear attitude and gyroscope's bias estimation for a VTOL UAV," *International Journal of Systems Science*, vol. 38, no. 3, pp. 197–210, 2007.

[51] W. J. Rugh, *Linear System Theory (2nd Ed.)*. Upper Saddle River, NJ, USA: Prentice-Hall, Inc., 1996.

[52] S. Sastry and M. Bodson, *Adaptive control: stability, convergence and robustness*. Prentice-Hall Inc., 1989.

[53] G. G. Scandaroli and P. Morin, "Nonlinear filter design for pose and IMU bias estimation," in *2011 IEEE International Conference on Robotics and Automation (ICRA)*, May 2011, pp. 4524–4530.

[54] G. G. Scandaroli, P. Morin, and G. Silveira, "A nonlinear observer approach for concurrent estimation of pose, IMU bias and camera-to-IMU rotation," in *2011 IEEE/RSJ International Conference on Intelligent Robots and Systems (IROS)*, September 2011, pp. 3335–3341.

[55] Schäcke, Kathrin, "On the Kronecker Product," Master's thesis, University of Waterloo, Mathematics Department, 2013.

[56] H. E. Soken and S. Sakai, "TRIAD+Filtering Approach for Complete Magnetometer Calibration," in *2019 9th International Conference on Recent Advances in Space Technologies (RAST)*, June 2019, pp. 703–708.

[57] E. A. Sperry, "Gyroscopic Compass," U.S. Patent US1 279 471A, 1918.

[58] A. R. Spielvogel and L. L. Whitcomb, "Preliminary results with a low-cost fiber-optic gyrocompass system," in *2015 MTS/IEEE OCEANS*, October 2015, pp. 1–5.

[59] A. R. Spielvogel and L. L. Whitcomb, "A stable adaptive attitude estimator on SO(3) for true-North seeking gyrocompass systems: Theory and preliminary simulation evaluation," in *2017 IEEE International Conference on Robotics and Automation (ICRA)*, May 2017, pp. 3231–3236.

[60] A. R. Spielvogel and L. L. Whitcomb, "Adaptive estimation of measurement bias in six degree of freedom inertial measurement units: Theory and preliminary simulation evaluation," in *2017 IEEE/RSJ International Conference on Intelligent Robots and Systems (IROS)*, September 2017, pp. 5880–5885.

[61] A. R. Spielvogel and L. L. Whitcomb, "Adaptive Sensor Bias Estimation in Nine Degree of Freedom Inertial Measurement Units: Theory and Preliminary Evaluation," in *2018 IEEE/RSJ International Conference on Intelligent Robots and Systems (IROS)*, October 2018, pp. 5555–5561.

[62] A. R. Spielvogel and L. L. Whitcomb, "A Stable Adaptive Observer for Hard-Iron and Soft-Iron Bias Calibration and Compensation for Two-Axis Magnetometers: Theory and Experimental Evaluation," *IEEE Robotics and Automation Letters*, vol. 5, no. 2, pp. 1295–1302, April 2020.

[63] A. R. Spielvogel, A. S. Shah, and L. L. Whitcomb, "Online 3-axis magnetometer hard-iron and soft-iron bias and angular velocity sensor bias

estimation using angular velocity sensors for improved dynamic heading accuracy," *Journal of Field Robotics*, Under Review, 2020.

[64] A. R. Spielvogel and L. L. Whitcomb, "Adaptive Bias and Attitude Observer on the Special Orthogonal Group for True-North Gyrocompass Systems: Theory and Preliminary Results," in *Proceedings of Robotics: Science and Systems*, Pittsburgh, Pennsylvania, June 2018.

[65] A. R. Spielvogel and L. L. Whitcomb, "Adaptive Bias and Attitude Observer on the Special Orthogonal Group for True-North Gyrocompass Systems: Theory and Preliminary Results," *The International Journal of Robotics Research*, vol. 39, no. 2-3, pp. 321–338, 2019.

[66] E. Steele, T. Boyd, M. Inall, E. Dumont, and C. Griffiths, "Cooling of the West Spitsbergen Current: AUV-Based Turbulence Measurements West of Svalbard," in *2012 IEEE/OES Autonomous Underwater Vehicles (AUV)*, September 2012, pp. 1–7.

[67] Teledyne RD Instruments, Poway, CA, USA, "Teledyne RD Instruments Explorer Doppler Velocity Log (DVL) Datasheet," 2017.

[68] E. Thébault, C. C. Finlay, C. D. Beggan, P. Alken, J. Aubert, O. Barrois, F. Bertrand, T. Bondar, A. Boness, L. Brocco, E. Canet, A. Chambodut, A. Chulliat, P. Coïsson, F. Civet, A. Du, A. Fournier, I. Fratter, N. Gillet, B. Hamilton, M. Hamoudi, G. Hulot, T. Jager, M. Korte, W. Kuang, X. Lalanne, B. Langlais, J.-M. Léger, V. Lesur, F. J. Lowes, S. Macmillan, M. Mand ea, C. Manoj, S. Maus, N. Olsen, V. Petrov, V. Ridley, M. Rother, T. J. Sabaka, D. Saturnino, R. Schachtschneider, O. Sirol,

A. Tangborn, A. Thomson, L. Tøffner-Clausen, P. Vigneron, I. Wardinski, and T. Zvereva, "International Geomagnetic Reference Field: the 12th generation," *Earth, Planets, and Space*, vol. 67, p. 79, May 2015.

[69] H. H. Thompson, "Gyroscopic Compass," U.S. Patent US1 773 412A, 1930.

[70] G. Troni and L. L. Whitcomb, "Field Sensor Bias Calibration with Angular-Rate Sensors: Theory and Experimental Evaluation with Application to Magnetometer Calibration," *IEEE/ASME Transactions on Mechatronics*, pp. 1–1, 2019.

[71] G. Troni, "Advances in precision navigation of underwater vehicles," Ph.D. dissertation, Johns Hopkins University, Department of Mechanical Engineering, 2013.

[72] G. Troni and L. L. Whitcomb, "Adaptive Estimation of Measurement Bias in Three-Dimensional Field Sensors with Angular Rate Sensors: Theory and Comparative Experimental Evaluation," in *Robotics: Science and Systems*, 2013.

[73] V. Vali and R. Shorthill, "Fiber ring interferometer," *Applied optics*, vol. 15, no. 5, pp. 1099–1100, 1976.

[74] J. F. Vasconcelos, G. Elkaim, C. Silvestre, P. Oliveira, and B. Cardeira, "Geometric Approach to Strapdown Magnetometer Calibration in Sensor Frame," *IEEE Transactions on Aerospace and Electronic Systems*, vol. 47, no. 2, pp. 1293–1306, April 2011.

[75] S. Webster, "Decentralized Single-beacon Acoustic Navigation: Combined Communication and Navigation for Underwater Vehicles," Ph.D. dissertation, Johns Hopkins University, Department of Mechanical Engineering, 2010.

[76] L. Whitcomb, D. Yoerger, and H. Singh, "Advances in Doppler-based navigation of underwater robotic vehicles," in *1999 IEEE International Conference on Robotics and Automation (ICRA)*, vol. 1, May 1999, pp. 399–406 vol.1.

[77] Woodman, Oliver J., "An introduction to inertial navigation," University of Cambridge, Cambridge, UK, Tech. Rep., 2007.

[78] T. H. Wu, E. Kaufman, and T. Lee, "Globally Asymptotically Stable Attitude Observer on SO(3)," in *2015 54th IEEE Conference on Decision and Control (CDC)*, December 2015, pp. 2164–2168.

[79] Z. Wu, Y. Wu, X. Hu, and M. Wu, "Calibration of Three-Axis Magnetometer Using Stretching Particle Swarm Optimization Algorithm," *IEEE Transactions on Instrumentation and Measurement*, vol. 62, no. 2, pp. 281–292, Febuary 2013.

[80] M. Zhou, R. Bachmayer, and B. de Young, "Working towards seafloor and underwater iceberg mapping with a Slocum glider," in *2014 IEEE/OES Autonomous Underwater Vehicles (AUV)*, October 2014, pp. 1–5.

Vita

Andrew R. Spielvogel was born in Boston, Massachusetts in 1990. From 2004-2009, he attended the Green Mountain Valley School where he was Valedictorian of the Class of 2009. Afterwards, he attended Harvard University, where he graduated cum laude in May 2013 with a S.B. in Electrical Engineering with high honors in field. While at Harvard, Andrew competed for four years on the NCAA Division 1 Harvard Alpine Ski team where he was named three times to the All-Academic Team (2011-2013) and twice captain of the ski team (2011-2012, 2012-2013). After graduating college, Andrew was an Electrical Engineering Intern at Harvest Automation where he worked on a vision system for mobile robots in the nursery and greenhouse industries. In August 2014, he enrolled in the Mechanical Engineering Ph.D. program at Johns Hopkins University, where he received a Robotics MSE in 2017.